

## ABSTRACT

Title of Thesis: DEVELOPMENT OF A PROTOTYPE  
MAGNETOSTRICTIVE ENERGY HARVESTING DEVICE

Mark Elliott Staley, Master of Science, 2005

Thesis directed by: Professor Alison B. Flatau  
Department of Aerospace Engineering

To enhance performance and safety, structures of all types are made “smart” with the addition of sensors. These sensors require power, but in some cases conventional power supply methods are inadequate. Ideally, these sensors would convert the available ambient energy into electrical energy. This thesis develops and examines a prototype energy harvesting transducer which converts mechanical vibration into electrical energy. The transducer utilizes the coupling between the magnetic and elastic state of magnetostrictive materials along with a flux-linked coil for conversion of mechanical energy to electrical energy. The examined transducer doesn’t affect the stiffness characteristics of the host structure, but as a result its performance is dependant on a resonance condition. Experimental results led to coupled optimization of prestress and magnetic bias. An electric circuit model is proposed and compared to test results. Efficiency calculations prove the current transducer to be inefficient, but possible areas of significant improvement were identified.

DEVELOPMENT OF A PROTOTYPE MAGNETOSTRICTIVE ENERGY  
HARVESTING DEVICE

By

Mark Elliott Staley

Thesis submitted to the Faculty of the Graduate School of the  
University of Maryland, College Park in partial fulfillment  
of the requirements for the degree of  
Master of Science  
2005

Advisory Committee:

Dr. Alison Flatau, Chair  
Dr. Amr Baz  
Dr. Norman Wereley

© Copyright by  
Mark Elliott Staley  
2005

## TABLE OF CONTENTS

1. INTRODUCTION.....	1
1.1 Objective.....	1
1.2 Review of Energy Harvesting Principles.....	4
1.2.1 Introduction.....	4
1.2.2 Electric Generators (Wind/Hydro/Geothermal Power).....	4
1.2.3 Solar Power.....	9
1.2.4 Piezoelectric Power.....	12
1.2.5 Magnetostrictive Power.....	14
1.3 Review of Magnetostrictives Materials and Magnetostrictive Transduction.....	15
1.3.1 Material Background.....	15
1.3.2 Basics of Magnetostrictives.....	17
1.3.2.1 Relationship between magnetic flux density and magnetic field.....	18
1.3.3 Performance considerations.....	28
2. TRANSDUCER DESIGN AND TESTING METHODOLOGY.....	33
2.1 Transducer Design.....	33
2.1.1 Overview.....	33
2.1.2 Magnetic Circuit Design.....	37
2.1.3 Prestress Adjustment Design.....	38
2.1.4 Resonance Prediction and Tuning.....	39
2.1.5 Bias Coil and Sense Coil Design.....	42
2.2 Test Procedure.....	43
3. EXPERIMENTAL RESULTS.....	50
3.1 Static Strain-H Curves.....	50
3.2 Sine sweep tests to characterize transducer performance.....	51
3.3 Sinusoidal dwell tests.....	54
3.4 Sine sweep tests at 2 ksi and different biases.....	58
3.5 Sine Sweep Tests at different prestresses and optimum bias.....	60
3.6 Scalability of electrical output to mechanical input.....	62
3.7 Circuit Tests.....	66
3.8 Coil Inductance.....	69
4. FULL CIRCUIT MODELING.....	72
4.1 Circuit Model.....	72
4.2 Transducer Efficiency.....	75
5. CONCLUSION.....	79
5.1 Summary of Results.....	79
5.2 Recommended Future Work.....	80
APPENDIX A.....	84
APPENDIX B.....	88
APPENDIX C.....	91
APPENDIX D.....	93
APPENDIX E.....	94
References.....	106

## LIST OF FIGURES

Figure 1.1: Magnetic flux density, $B$ , versus applied magnetic field, $H$ , for a theoretical ferromagnetic material. Taken from Calkins. <sup>4</sup> .....	19
Figure 1.2: $\lambda$ - $H$ butterfly curves for Terfenol-D from Kellogg <sup>10</sup> under zero and one ksi prestress. ....	23
Figure 1.3: Eddy current cutoff frequency relationship to rod diameter for Terfenol-D and Galfenol using the relative properties of each material. Relative permeability of 10 and 100 used for Terfenol-D and Galfenol respectively. Resistivity shown in table 1-1.....	31
Figure 2.1: Two types of energy harvesting transducers .....	34
Figure 2.2: Picture of the energy harvesting transducer used in this study. ....	36
Figure 2.3: Diagram of the energy harvesting transducer designed for this study .....	36
Figure 2.4: Diagram of resonant beam in the energy harvesting transducer. ....	39
Figure 2.5: Output field at radial center of the bias coil along the axis vs. applied DC voltage.....	44
Figure 2.6: Diagram of Power supply setup to control the DC magnetic bias coil. ....	46
Figure 2.7: Full circuit test setup, including representation of the sense coil and the load resistance...	47
Figure 3.1: Static Strain- $H$ curve for research Galfenol and Terfenol-D under a 3.9 ksi prestress. ....	51
Figure 3.2: Normalized frequency vs. acceleration curves for Terfenol-D, research and production Galfenol. Plots are all normalized to the maximum tip acceleration of the Terfenol-D plot.....	52
Figure 3.3: Normalized open circuit sense coil voltage response for Terfenol-D, research Galfenol and production Galfenol as the magnetostrictive. Curves are normalized with respect to the Terfenol-D curve peak open circuit voltage output. This is why the graph exceeds a value of one on the y-axis. ....	53
Figure 3.4: Terfenol-D sweep tests at for 1, 2 and 3 ksi prestress. Data taken on 4/13/05.....	56
Figure 3.5: Terfenol-D sweep tests at 1, 2 and 3 ksi prestress. Data taken on 4/14/05. ....	56
Figure 3.6: research Galfenol sweep tests at 1, 2 and 3 ksi prestress. Data from 4/13/05.....	57
Figure 3.7: research Galfenol sweep tests at 1, 2 and 3 ksi prestress. Data on 4/14/05.....	57
Figure 3.8: Sense coil output for Terfenol-D at 2 ksi prestress and varying biases.....	59
Figure 3.9: Sense coil output for research Galfenol at 2 ksi prestress and varying biases. ....	59

Figure 3.10: Sense coil open circuit output for Terfenol-D under different prestress and the corresponding optimum bias as determined from Figs. 3.4 and 3.5. ....	60
Figure 3.11: Sense coil open circuit output for research Galfenol under different prestresses and the corresponding optimum bias as determined from Figs. 3.6 and 3.7. ....	61
Figure 3.12: Sense coil output for Terfenol at 2 ksi and optimum bias (220 Oe) vs. frequency at input peak sine forces of 1,2,3 and 4 lb <sub>f</sub> . ....	63
Figure 3.13: Sense coil output for research Galfenol at 2 ksi and optimum bias ( 71 Oe) vs. frequency at input peak sine forces of 1,2,3 and 4 lb <sub>f</sub> . ....	63
Figure 3.14: Beam tip acceleration response vs. frequency at input peak sine forces of 1,2,3 and 4 lb <sub>f</sub> for Terfenol-D. ....	64
Figure 3.15: Beam tip acceleration response vs. frequency at input peak sine forces of 1,2,3 and 4 lb <sub>f</sub> for research Galfenol. ....	64
Figure 3.16: Sense coil output (Fig. 3.12) divided by beam tip acceleration (Fig. 3.14) for Terfenol-D. ....	65
Figure 3.17: Sense coil output (Fig. 3.13) divided by beam tip acceleration (Fig. 3.15) for research Galfenol. ....	65
Figure 3.18: Power delivered to load vs. load resistance for production and research Galfenol and Terfenol-D under 2 ksi prestress and optimum bias for each material. This data was obtained with the 20 ohm coil and a 2-lb input sinusoidal force at the transducer resonant frequency of ~61 Hz. ....	67
Figure 3.19: Comparison of power delivered to the load resistance for the two different coils tested. Material is Terfenol-D under 2 ksi prestress and a 2-lb input sinusoidal force at the transducer resonant frequency of ~61 Hz. ....	68
Figure 3.20: Comparison of power delivered to the load resistance for the two different coils tested. Material is research Galfenol under 2 ksi prestress and a 2-lb input sinusoidal force at the transducer resonant frequency of ~61 Hz. ....	69
Figure 4.1: Impedance Triangle. ....	73

Figure 4.2: Power delivered to load resistance vs. the load resistance for Terfenol-D and research  
Galfenol. Generated using equation 4.6. .... 74

Figure 5.1: Power delivered to load resistance versus load resistance. Includes matched capacitance  
case. Assumes sense coil generates 1 volt in each case. .... 82

## LIST OF TABLES

Table 1-1: Average loss distribution for NEMA design B motors, taken from Emadi. <sup>8</sup> It indicates the percentage magnitude of the total energy loss for the significant loss mechanisms.....	6
Table 1-2: Approximate material property values for Terfenol-D, research Galfenol, production Galfenol and Iron from Calkins <sup>4</sup> , Etrema, Inc and ductile.org. ....	17
Table 2-1: Examination of the different tests performed; the overall test purpose, the variables involved, materials tested, output measurement type and additional knowledge gained. ....	49
Table 3-1: Terfenol-D maximum sense coil output comparison .....	61
Table 3-2: research Galfenol maximum sense coil output comparison.....	61
Table 3-3: Optimum load resistance for maximum power transfer to load for the two different coils and two different materials.....	69
Table 3-4: Coil Inductance readings at two test frequencies for 4 different coil core materials: Air, Terfenol-D, research Galfenol, production Galfenol. All readings taken under no prestress or bias. ....	70
Table 3-5: Coil inductance readings at 120 Hz for Terfenol-D, research Galfenol, and production Galfenol under 1, 2 and 3 ksi prestress, but no magnetic bias.....	71
Table 3-6: Coil inductance readings at 120 Hz for Terfenol-D, research Galfenol, and production Galfenol under 2 ksi prestress for when no bias and optimum bias were applied. ....	71
Table 4-1: Experimental vs. analytical optimum load resistance values for Terfenol-D and research Galfenol in the 20 ohm coil. ....	74

# 1. INTRODUCTION

## 1.1 Objective

To enhance performance and safety, structures of all types, from buildings to airplanes to ships are made “smart” with to the addition of sensor arrays which can detect how well that structure is operating and predict failures before they occur. Advances in technology have made these sensors small, allowing them to run on little electrical power, but supplying them with power over the lifespan of a structure is a significant challenge.

The remote placement of some sensors prevents the traditional supply of electricity though wires attached to a distant power source. Perhaps a sensor needs to be mounted on the end of a drill which is rotating deep underground. Running wires along the length of the drill shaft could prove either unreliable due to the transient loading which could break the wires or unfeasible if the sensor needs to rotate along with the drill bit. The typical solution for cases where constant electrical power is not available through wires from a distant power source is to use batteries.

In addition to being wireless, batteries allow the sensor to be portable. Unfortunately all batteries have a finite amount of energy, after which they need to be either replaced or recharged or else the sensors they power will not be able to function. Depending on the placement of the sensor on the structure and the location of the

structure itself, (underwater, in space, remote geographical locations) battery replacement may be either a nuisance, challenging or impossible.

The optimum solution is to have a power source co-located with each sensor that uses the ambient energy available at its location, whether this be solar, thermal or mechanical. This provides the wireless advantage of the battery without its finite power supply. The intrinsic coupling between mechanical and magnetic states of magnetostrictive materials, combined with an inductive coil to convert the magnetic energy into electrical energy, theoretically should provide transduction of mechanical energy into electrical energy. The research presented in this thesis focuses on designing, testing, and optimizing a magnetostrictive transducer which converts mechanical vibratory energy into electrical energy.

Mechanical energy can be harvested from a transducer that is a structural component and carries critical loads in addition to harvesting power, such as one designed to function as an engine mount, or one that extracts energy without affecting the behavior of the structure, such as one designed to utilize the ambient mechanical vibration of a ship's hull to generate electrical power for sensors. The latter transducer type was selected as the focus of this research.

To examine the feasibility of magnetostrictive-based energy harvesting, a transducer was designed and built which allows for characterization and optimization of the variables that affect energy conversion. Both the magnetostrictive core and the

inductive coil of this transducer could easily be switched out to study their affect on the transducer performance. This transducer was also designed with tunable stiffness that allowed matching of the energy harvester's resonant response to the vibration frequency of its host structure.

Two magnetostrictive materials are investigated, Terfenol-D and Galfenol. Terfenol-D has been used successfully in many commercial actuator applications where electrical energy is converted into a mechanical output. Galfenol is a newer and a less well characterized material. Both production and research grade Galfenol, same material, but different production method, are investigated in this thesis.

Results from both open circuit and full or closed circuit experiments are presented in chapter 3 and 4 respectively. Open circuit experiments provided results used for optimization of the magnetostrictive transduction with respect to prestress and magnetic bias, two variables which have been quantified in their affect on magnetostrictive actuator performance.<sup>3,21</sup> A second experimental method, full circuit testing, was used to quantify the real electrical power output to a load device and to optimize that load resistance. Finally a model of circuit performance is proposed and compared to experimental results.

## **1.2 Review of Energy Harvesting Principles**

### **1.2.1 Introduction**

This chapter examines current means and methods of harvesting electrical energy from ‘free energy’ sources. Typical electrical power generation requires the constant input of fuel such as coal and oil to sustain the process. For wind, hydro, geothermal and solar power the wind, water, steam and light that provide the energy input for each respective process are free in the sense that no fuel is consumed and no waste expelled. Coal power plants have a setup cost for the plant and daily costs for the coal. Wind, hydro, geothermal and solar power installations also have setup costs, but have no daily costs for consumables since there are none. In addition to the previously mentioned processes, more recent methods include piezoelectric and magnetostrictive energy harvesting. These two methods are also free in the sense that they require no consumable fuel input, but they currently occupy a distinct area of utility from wind, hydro, geothermal and solar power. This chapter will examine the usefulness and challenges associated with efficient implementation of each ‘free energy’ harvesting method.

### **1.2.2 Electric Generators (Wind/Hydro/Geothermal Power)**

Electric Generators convert the kinetic energy of a spinning turbine into a time varying magnetic field that is then transformed into electrical energy. The same principles apply whether the kinetic energy source is wind, hydro or geothermal power. Faraday’s law of electromagnetic induction (eqn. 1.1) provides the basis for

the transduction of magnetic to electrical energy.<sup>23</sup> His law states that a time varying magnetic flux,  $\Phi$ , through the enclosed area of a single loop of wire, of length  $l$ , induces a voltage,  $E$ , in that loop.

$$\oint \vec{E} \cdot d\vec{l} = -\frac{d\phi}{dt} \quad (1.1)$$

Transduction of kinetic to magnetic energy is accomplished by connecting a rotor with magnetic poles at every blade end to a shaft driven by a turbine. Each magnetic pole is typically comprised of copper wire wound around a laminated iron core or a permanent magnet. The permanent magnet setup is simpler and requires no power input to generate a magnetic field. The electromagnet method gives controllability over the output of the system because it allows for an adjustable magnitude of rotor magnetic field. Spinning of the turbine shaft caused by wind, hydro, or geothermal energy spins the rotor. In turn, the spinning rotor generates a time varying magnetic field due to motion of the magnetic poles. The electrical output is created in the stator, a stationary device which contains coils of wire wound around the diameter of the rotor. These coils generate current from the time varying magnetic flux of each rotor pole as it passes by. The magnetic field of the rotor directly affects the magnitude of magnetic flux through the stator, which is why the electromagnet setup allows for controllability of stator electrical output.

Energy is lost in AC generators due to the resistance of the stator coil, eddy currents in metal components, hysteric losses in ferromagnetic components and friction in moving components. Other losses can be quantified experimentally; these are separate from the loss types previously mentioned, and are generally classified as

‘stray load losses’.<sup>8</sup> These losses are affected by many variables of the generator design and are difficult to model. Also, the electrical energy input to create the magnetic field of electromagnetic rotors must be deducted from the stator coil output to determine the net amount of electrical energy created. Table 1.1 attributes a percentage of the total loss amount to the different loss mechanisms for a motor. Motors and generators operate on the same principle, but motors turn electrical energy into mechanical energy.

Table 1-1: Average loss distribution for NEMA design B motors, taken from Emadi.<sup>8</sup> It indicates the percentage magnitude of the total energy loss for the significant loss mechanisms.

Motor component loss	Total loss, %
Stator power loss $I_s^2R$	37
Rotor power loss $I_r^2R$	18
Magnetic core loss	20
Friction and windage	9
Stray load loss	16

Wind power and hydro power operate on the same basic principle of extracting power from the kinetic energy of a fluid in motion. The only difference is the type of fluid, gas or liquid, for wind and hydro power respectively. Since liquids are denser than gases, a liquid of the same velocity and volume as a gas will contain more kinetic energy. In both cases, the ideal energy extracted is the difference in fluid velocity before and after the turbine. Hydro power is more consistent in its output since dams can be used to exert control the height of a reservoir and the volume of water that

passes through the turbines. Wind turbines extract energy from the wind, but cannot control its velocity or volume.

Wind power for uses other than electric power generation date back in recorded history as far back as the 17<sup>th</sup> century B.C. in Babylonia, but it was Denmark that first used wind power to generate electricity in the 1890.<sup>13</sup> These early machines generated 5-25kW, but more modern wind turbine installations are capable of generating hundreds of kW.<sup>13</sup> Recent turbines with rotor diameters of 48-54 meters are rated at 750-1000 kW.<sup>17</sup>

For wind turbines, power output is affected not only by the velocity of the air, but the consistency of the wind direction and its velocity over time. The power output from a wind turbine is proportional to the rotor diameter squared and the wind speed cubed.<sup>17</sup> A calculation of the ideal power difference in the wind energy before and after the turbine yields the Betz coefficient.<sup>13</sup> The Betz coefficient of .593 indicates that an ideal turbine would extract 59.3 percent of incoming wind energy. In practice, good systems can achieve 35 to 40 percent efficiency after mechanical losses.

Here it important to mention that the above mentioned efficiency corresponds to the turbine only (i.e. conversion of ambient energy to kinetic energy), and is noted as  $\eta_{Turbine}$ . The AC generator has its own efficiency, which can be denoted as  $\eta_{Generator}$ . The total efficiency of the device from input ambient energy to output electrical energy is determined from the equation below.

$$\eta_{Total} = \eta_{Turbine}\eta_{Generator} \quad (1.2)$$

If, for example a wind turbine had an efficiency of 40 percent ( $\eta_{Turbine} = .4$ ), and the associated generator had an efficiency of 50 percent ( $\eta_{Generator} = .5$ ), then the total device efficiency would be ( $\eta_{Total} = .4 * .5 = .2$ ) 20 percent.

The quantity of power that a hydro power plant can produce is dependant on two variables; water discharge and hydraulic head. Water discharge is the volume flow of water through the plant and hydraulic head is the elevation difference between the water entering and the water exiting the plant. Various types of turbine designs, from impulse turbines to axial-flow reaction turbines provide efficient transfer of energy to the generator for different amounts of water discharge and hydraulic head. As is the case for wind turbines, the goal is to maximize the kinetic energy of the shaft and rotor which drives the generator.

‘Micro’ and ‘mini’ hydro power are smaller, more specialized applications of hydro power generation. The definitions vary somewhat depending on organization and country, but micro and mini hydro power are defined by the amount of power

produced and refer to installations that generate less than 100 kW and 101-1000 kW respectively.<sup>11</sup>

Another similar process worth mentioning is geothermal power, which uses the earth's heat. In some places around the world hot water and steam is located near the surface, making the investment cost to obtain these resources reasonable. Locations with available water or steam below 150°C is termed low temperature, anything above 150°C is termed high temperature.<sup>10</sup> Higher temperature locations are the most appealing for commercial electrical power generation because the fluid itself contains more energy. For all geothermal power plants, steam energy is used to drive a turbine which in turn drives a generator to create electrical power employing the same operational principles as wind and hydro power, just with a different fluid.

### **1.2.3 Solar Power**

On average the earth receives more solar power in a single hour than is consumed by humans in a year.<sup>18</sup> The ability to turn sunlight into electricity was first discovered in 1839 by a scientist named Edmund Becquerel, but it was not until 1954 that the first solar cell was made.<sup>18</sup> Space exploration provided the main impetus for solar cell development and in 1958 the United States launched the first satellite augmented with solar panels, the Vanguard I. Solar power has large potential for power generation due to the large input power from the sun, but many challenges limit its practical use.

At the earth's distance from the sun, an average value for incident solar power per area is  $1367 \text{ W/m}^2$ , but the actual solar power hitting a given surface of the earth is dependant on latitude, weather, and the position and angle of the earth with respect to the sun.<sup>18</sup> As light passes through the atmosphere it is both absorbed and scattered. The length of air through which the light passes depends on the angle between the sun and the position of interest. When the sun is directly overhead the path is the shortest. The total or global radiation that reaches a point is the sum of three components: direct, diffuse and albedo radiation. Direct radiation is unscattered light from the sun, diffuse is scattered light that still reaches the ground and albedo radiation is reflected from the ground to an object. Seasonal variations have a larger effect as the distance from the equator increases. Finally, daily weather variations cause the greatest irregularity in the amount of irradiation that reaches the ground. The variation in the quantity of light energy that reaches the ground due to seasonal impact and daily weather makes reliable solar power virtually impossible in many geographic locations.

Semi-conductor technology enabled the creation of solar cells which turn light energy into electrical energy. The conversion capability is dependant on the crystal structure and the electron bonds between neighboring atoms. The band of electrons which is shared between atoms and holds them together is termed the valence band. Electrons in the next higher energy band, the conduction band are free to move since they are not bound to other atoms.<sup>20</sup> Since electrons in the valence band cannot move, when that band is full and there are no electrons in the conduction band the material, which

is the case for pure silicon, the material acts as an insulator. Doping the material with other atoms creates either electrons in the conduction band or a deficiency of electrons in the valence band, either of which allows for electrical conduction. An n-type semi-conductor has excess electrons in the conduction band, while a p-type semi-conductor has electron deficiencies (holes) in the valence band. These two types of materials are combined to form a p-n junction, which then creates an electric field across the junction due to the charge discrepancy. When high energy photons hit the material, their energy is absorbed by valence band electrons promoting them from the valence band to the conduction band. The amount of energy required to promote an electron from the valence band to the conduction band depends on the type of material.

Solar cells that have high electron energy gaps between the valence band and the conduction band produce high voltages, but low currents.<sup>18</sup> The energy of the photons that hit the solar cell that are below the energy gap of the material is released as heat and not converted into electrical energy. Released electrons are then free to move in the electric field generated by the p-n junction, thus creating a current. This current is collected by a back metal plate and a top metal strips, which connect to a larger piece called the bus bar. The use of thin metal strips on top allows light to pass between them into the solar cell. These solar cells are then connected in series and parallel combinations to increase the voltage and current generated to useful levels.

A 1995 study of solar power found that the average efficiency of commercially available solar power modules was 14.5% in 1994.<sup>2</sup> Typically solar power installations are small, generating 50W-5kW. Larger solar installations are possible, the first being a 1-MW installation in California in 1982 which is connected into the power grid.<sup>1</sup> Solar power is still more expensive than conventional methods, which restricts its main use to areas where there is no power grid.

#### **1.2.4 Piezoelectric Power**

Piezoelectric energy harvesting directly converts vibratory mechanical input energy into electrical energy, essentially making it a new type of generator. Piezoelectricity was first discovered in 1880 by two Frenchmen, Pierre and Jacques Curie.<sup>6</sup> Their research revealed a class of materials that had a coupled relationship between mechanical stress and electrical charge. This relationship is directly due to the crystal structure of the material. Geometrically, certain crystal types have asymmetry which then yields an electric asymmetry since the protons and electrons do not counteract each other in all crystallographic directions.

Commonly used piezoelectric materials are quartz, and man-made materials such as piezoceramics (PZT) and piezopolymers (PVDF). Piezoceramics are a mixture of lead, zirconium and titanium-oxide which, during a cooling phase of production, organize into an asymmetric crystal structure. At this point the net polarization of the material is zero because the crystals are randomly oriented. The material is then placed under a high electric field which reorients the crystals in the direction of the applied field giving the material a net polarization. PVDF is made of polymer chains

of carbon, fluorine and hydrogen. Since the material is relatively soft, polarization of the material is achieved by mechanical stretching and electric field application. Both materials can be depoled if they reach a temperature above its Curie temperature, if they are placed under a high mechanical stress, or if a high electric field in the opposite direction of polarization is applied.<sup>6</sup>

Electrical and mechanical performance can be described in two linear constitutive equations, shown below, for most conditions.<sup>6</sup>

$$\begin{aligned}\varepsilon_i &= s_{ij}^E \sigma_k + d_{ki} E_k \\ D_i &= d_{ik} \sigma_k + e_{ik}^{\sigma} E_k\end{aligned}\tag{1.3}$$

The top equation describes how the mechanical strain,  $\varepsilon$ , is affected by mechanical stress,  $\sigma$ , and electrical field,  $E$ . The bottom equation describes how the electric displacement,  $D$  (Coulombs/area), is affected by mechanical stress and electric field. The other variables represent material properties, such as compliance,  $s$ , and permittivity,  $e$ . The unique material property is the piezoelectric coupling matrix,  $d$ , which quantifies relationships between electric and mechanical performance. The top and bottom equations describe actuator and sensor operation respectively. It is the sensor equation, electric displacement output due to mechanical stress input, which can be used to describe piezoelectric energy harvesting.

Research into piezoelectric energy harvesting applications has revealed the usefulness and challenges for commercial applications. A few prototype devices and advanced circuit control techniques have been developed and tested with reported peak

efficiencies of 35%<sup>26</sup> and 20%.<sup>14</sup> Ottoman et al.<sup>22</sup> have developed a DSP-controlled adaptive circuit to maximize power delivered from a piezoelectric energy harvesting element to a battery. This research led to a 325% increase in the power delivered to the battery, but it requires a minimum piezoelectric power output before it is useful, since the adaptive circuit requires power to operate. Microstrain, Inc has developed a fully integrated sensor system with a piezoelectric energy harvesting device which is capable of producing 2 milliwatts of power at an input frequency of 60 Hz and approximately a tenth of a G acceleration input.<sup>15</sup>

### **1.2.5 Magnetostrictive Power**

Of the energy methods described in this chapter, magnetostrictive power harvesting is most similar to the method described in 1.2.2., because it converts a time varying magnetic field into electric energy according to Faraday's law (eqn. 1.1). The difference lies in the transduction of kinetic to magnetic energy. This process is analogous to the piezoelectric transduction process described in section 1.2.4. Ultimately, a magnetostrictive energy harvesting device uses an inductive coil to convert the time varying magnetic flux generated by the mechanically induced vibration of the magnetostrictive rod into electrical power. Section 1.3 provides a more detailed discussion on the theory of this energy conversion process along with background information on magnetostrictive materials.

### **1.3 Review of Magnetostrictives Materials and Magnetostrictive Transduction**

This chapter will provide an overview of magnetostrictive materials. It includes a review of the history and composition of Terfenol-D and Galfenol, a physical explanation for magnetostriction, simplified equations that model magneto-mechanical transduction and electro-magneto-mechanical transduction and finally discussion of the main external factors which affect the energy harvester's performance. This information will explain the basis of the potential for magnetostrictive energy harvesting and provide motivation for the variety of experimental tests performed.

#### **1.3.1 Material Background**

Magnetostrictive materials are a class of materials which deform physically or strain due to a change in the magnetization state of the material. This type of behavior was first discovered in iron by James Joule in the 1840's.<sup>4</sup> Iron exhibits maximum magnetically induced strain, termed "magnetostriction" on the order of 10 microstrain. A specialized class of magnetostrictive materials is those which are capable of order of magnitude increases in strain deformations relative to iron. These materials are subsequently termed as "large" or "giant" magnetostrictive materials which are capable of magnetostriction on the order of 100 and 1000 microstrain respectively. The discovery of giant magnetostrictive materials directly lead to

increased engineering interest in possible applications, previously prohibitive with conventional magnetostrictives such as iron.

The most widely used commercially available giant magnetostrictive material is Terfenol-D ( $Tb_xDy_{1-x}Fe_y$   $x = .3$   $y = 1.92$ ). The material is comprised of Terbium (Tb), Iron (Fe) and Dysprosium (Dy), and the 'nol' ending stands for 'Naval Ordnance Laboratory' where it was developed in the 1960's. In addition to Terfenol-D, the "large" magnetostrictive material, Galfenol is examined in this thesis. Developed in the late 1990's also by the Navy, Galfenol ( $Fe_{1-x}Ga_x$   $.13 \leq x \leq .31$ ) is comprised of Gallium (Ga) and Iron (Fe). Galfenol was developed to create a magnetostrictive material that didn't have Terfenol-D's less desirable qualities, predominantly brittleness and low tensile strength, both of which limit its structural use. Table 1.2 summarizes material properties for the magnetostrictive materials examined in this study as well as iron.

Research Galfenol and production Galfenol have the same material composition, but they are manufactured (grown) at different rates, which yields different properties. Both are polycrystalline materials, but the crystals in research Galfenol are larger and better oriented than those in production Galfenol due to a slower growing process. Crystal orientation refers to their how well each crystal axis is oriented relative to the molecular lattice orientation that exhibits the largest magnetostriction. The better material properties of research Galfenol comes at a significantly increased

manufacturing cost as compared to that of production Galfenol, which is why both are examined in this study.

Table 1-2: Approximate material property values for Terfenol-D, research Galfenol, production Galfenol and Iron from Calkins<sup>4</sup>, Etrema, Inc and ductile.org.

	Terfenol-D	Research Galfenol	Production Galfenol	Iron
Maximum Magnetostriction ( $\lambda_s$ )	2000 ppm	240 ppm	175 ppm	20 ppm
Young's Modulus (E)	35-65 GPa	~70 GPa	~87 GPa	~190 GPa
Ultimate Tensile Strength ( $\sigma_T$ )	28 MPa	360 MPa	330 MPa	150-430 MPa
Ultimate Compressive Strength ( $\sigma_C$ )	700 MPa			500-1500 MPa
Relative Permeability ( $\mu_r$ )	1.5-8	60-360	60-360	>1000
Resistivity ( $\rho$ )	$58 \cdot 10^{-8}$ Ohm*m	$\sim 1.17 \cdot 10^{-6}$ Ohm*m		$9.7 \cdot 10^{-8}$ Ohm*m
Axial Strain Coefficient ( $d_{33}$ )	$3-20 \cdot 10^{-9}$ m/A			
Coupling Coefficient ( $k_{33}^2$ )	.5-.7	.4-.6		

### 1.3.2 Basics of Magnetostrictives

The behavior of magnetostrictive materials is due to a coupling between the elastic and magnetic states of that material. Below the Curie temperature of the material the crystal structure of magnetostrictives becomes ferromagnetic and all ferromagnetic materials exhibit magnetostriction to some degree.

### 1.3.2.1 Relationship between magnetic flux density and magnetic field

Commonly in the study of magnetostrictives, the magnetic field and magnetic flux density are denoted  $H$  and  $B$  respectively. (In other areas of study, such as physics<sup>23</sup> the magnetic flux density is termed the magnetic field.) Units for the magnetic field are amperes/meter (A/m) and Oersted (Oe). Units for the magnetic flux density are Tesla (T) and Gauss (G).

$$1 \text{ Oe} = 79.6 \text{ A/m}$$

$$1 \text{ G} = 10^{-4} \text{ T}$$

Magnetic flux,  $\Phi$ , is related to the magnetic flux density,  $B$ , in the following equation, where the area,  $A$ , is perpendicular to the flux lines.

$$\Phi = BA \quad (1.4)$$

The magnetic field,  $H$ , describes a quantity which arises due to the motion of electric charges and can be explained with Ampere's law for a long solenoid.<sup>16</sup> For a long solenoid with an air core, carrying a current,  $I$ , and having,  $n$ , number of turns per unit length of the solenoid, the resulting flux density,  $B$ , is,

$$B = \mu_o nI \quad (1.5)$$

where  $\mu_o$  is the permeability of free space, which is  $4\pi \cdot 10^{-7}$  H/m. In free space the relationship between  $B$  and  $H$  is linear as shown in the following equation.

$$B = \mu_o H \quad (1.6)$$

Hence the term  $n$  times  $I$  from equation 1.5 is equal to the magnetic field,  $H$ , in equation 1.6. Ferromagnetic materials and hence, magnetostrictive materials have a unique nonlinear relationship between  $B$  and  $H$ . A graph of the relationship between  $B$  and  $H$  in a ferromagnetic material is shown in Fig. 1.1. The magnetic flux density,

$B$  is still equal to the material permeability,  $\mu$ , times the magnetic field,  $H$ , but now the permeability is not a constant. The ferromagnetic material permeability can be experimentally determined by the following differential equation.

$$\mu = \frac{\partial B}{\partial H} \quad (1.7)$$

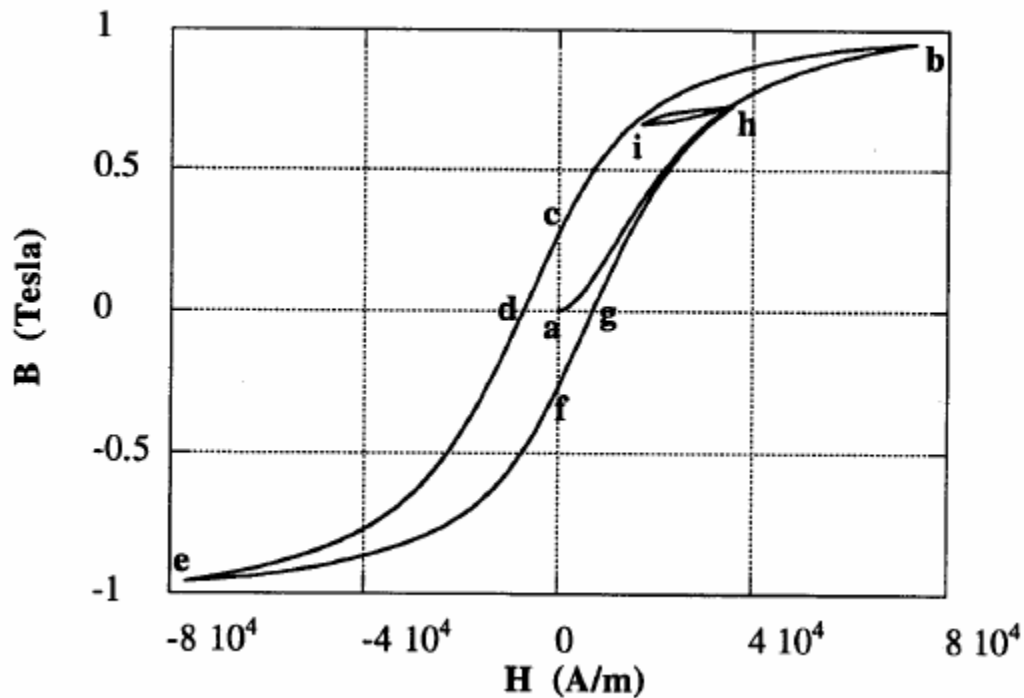


Figure 1.1: Magnetic flux density,  $B$ , versus applied magnetic field,  $H$ , for a theoretical ferromagnetic material. Taken from Calkins.<sup>4</sup>

Figure 1.1 shows a typical nonlinear and hysteretic relationship between magnetic flux density and the applied magnetic field in a ferromagnetic. The hysteretic nature of the curve is due to irreversible magnetization changes, such as the energy required to remove magnetic domains from pinning sites. Some examples of pinning sites are crystal imperfections, grain boundaries and magnetic inclusions, which are different

phase material.<sup>4</sup> The area inside the  $B$ - $H$  curve represents energy lost and is quantified in equation 1.8.

$$E_{hys} = \int BdH \quad (1.8)$$

Hysteretic energy losses reduce the efficiency of magnetostrictives and without proper cooling cause heating of the material which further reduces performance.<sup>4</sup>

Another way of understanding the material permeability is through the use of the material's magnetization,  $M$ . A ferromagnetic material's magnetization can be explained by an intrinsic presence of magnetic dipoles (North-South pole pairs) in the material, which are not all oriented parallel to each other. A more in depth discussion on the origin of magnetic moments in ferromagnetic materials can be found in Jiles.<sup>12</sup> Explained simply, magnetization,  $M$  is a material quantity of the same units as magnetic field,  $H$ , which affects magnetic flux,  $B$ , in the same way as an externally applied magnetic field. Therefore when there are is no external applied field due to the current, eqn 1.5, the magnetic flux density is defined simply by equation 1.9.

$$B = \mu_0 M \quad (1.9)$$

For a ferromagnetic material of magnetization,  $M$ , in the presence of an applied field,  $H$ , the magnetic flux density,  $B$ , is defined by equation 1.10. Hence the flux density through a material is due to the magnetization state of the material itself and outside influences.

$$B = \mu_o (H + M) \quad (1.10)$$

The magnetization of a material is not a constant versus applied field because the magnitude and direction of the applied field affects the material's magnetization.

When all the magnetic dipoles are aligned parallel to each other, the material is considered saturated, and the magnetization is at a maximum, termed  $M_s$ . The relationship between magnetization and field is defined as the susceptibility,  $\chi$ .

$$\chi = \frac{M}{H} \quad (1.11)$$

Moving,  $H$ , outside the parenthesis in equation 1.10 and using equation 1.11 to replace,  $M$ , yields equation 1.12.

$$B = \mu_o H(1 + \chi) \quad (1.12)$$

The quantity  $(1+\chi)$  is then termed the relative permeability of the material,  $\mu_r$ . Then the quantity  $(\mu_r)$  times  $(\mu_o)$  equals the permeability of the material,  $\mu$ , yielding the final equation for magnetic flux density.

$$B = \mu_o \mu_r H = \mu H \quad (1.13)$$

### 1.3.2.2 Relationship between strain and magnetic field

An applied magnetic field not only affects the magnetic state of a magnetostrictive material, but it also affects the material's mechanical state. For a magnetostrictive rod, application of a magnetic field yields a net change in the length of the rod. This magnetically induced change in length or magnetostriction is defined in terms of strain,  $\lambda$ .

$$\lambda = \frac{dl}{l} \quad (1.14)$$

It is this relationship between magnetic field and strain that Joule discovered in the 1840's, and it is this relationship in large and giant magnetostrictives which is why they are classified as smart materials. The applied magnetic field reorganizes the

magnetic domains (groups of like oriented magnetic dipoles) parallel to the field direction. The crystal structure affects magnetostriction as the magnetic dipoles prefer to align themselves to certain crystal axes. Such examination is not needed for this thesis, but can be found in Jiles<sup>12</sup> and Engdahl.<sup>9</sup>

For applications engineers, the relationship between field and magnetostriction is best examined graphically from experimental results (Fig. 1.2). Figure 1.2 shows the strain response,  $\lambda$ , of a Terfenol-D transducer to an externally applied magnetic field,  $H$ , parallel to the rod length, for two different prestresses, zero and one ksi. The effect of prestress is further examined in section 1.3.3.1. As the applied field increases from zero in either the positive or negative direction, the resulting strain response of the magnetostrictive core is positive, meaning the material is increasing in length parallel to the applied field. Because the magnetic dipoles are aligning themselves parallel to the applied field, a positive or negative field will yield the same alignment of ( $\pm 180^\circ$ ) magnetic dipoles and the same maximum change in length. This is why for AC transducer applications a magnetic bias field is applied; then an oscillatory field of lower magnitude than the bias field is applied so the net result is expansion and contraction of the transducer output. Like the  $B-H$  curve in Fig. 1.1, the  $\lambda-H$  curve also exhibits hysteresis which results in energy loss and reduced material performance.

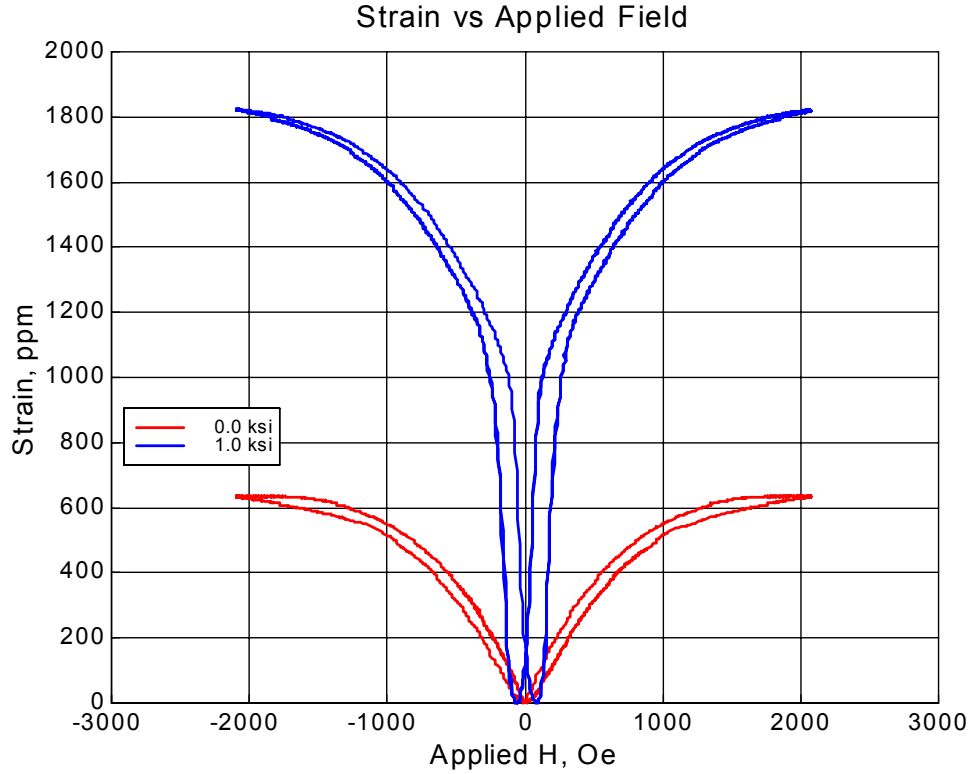


Figure 1.2:  $\lambda$ -H butterfly curves for Terfenol-D from Kellogg<sup>10</sup> under zero and one ksi prestress.

### 1.3.2.3 Linear constitutive equations and material properties

The magnetic and mechanical behavior of magnetostrictives in one dimension (and neglecting thermal effects) can be linearized using two equations that are very similar to the two coupled equations which describe linearized uniaxial piezoelectric material behavior (eqn. 1.3).

$$\begin{aligned}\varepsilon &= \frac{\sigma}{E^H} + dH \\ B &= d^* \sigma + \mu^\sigma H\end{aligned}\tag{1.15}$$

Total mechanical strain,  $\varepsilon$ , results from both an applied stress,  $\sigma$ , and an applied magnetic field,  $H$ , scaled respectively by the material's Young's modulus,  $E$ , and

magnetomechanical coefficient,  $d$ . The total magnetic flux density,  $B$ , is related to the applied stress and the applied magnetic field scaled by two additional material properties; the flux magnetomechanical coefficient,  $d^*$ , and permeability,  $\mu$ . The two magnetomechanical coupling coefficients are defined experimentally by the following two equations, where the  $\sigma$  and  $H$  refer to measurements at constant stress and constant applied magnetic field respectively.

$$\begin{aligned} d &= \left. \frac{\partial \varepsilon}{\partial H} \right|_{\sigma} \\ d^* &= \left. \frac{\partial B}{\partial \sigma} \right|_H \end{aligned} \tag{1.16}$$

As with equation 1.3, the top and bottom equations of eqn 1.15 describe actuator and sensor operation respectively. A brief study on the use of these equations in understanding the performance of a magnetostrictive Terfenol-D tooth phone is presented in Appendix E. Now that a linear approximation for magnetostrictive behavior has been presented, material properties can be better examined.

The apparent Young's modulus for magnetostrictive materials is affected by the magnetic state of the material. The maximum net change in the Young's modulus produced solely by changes in the magnetic state of the material is termed the delta  $E$  effect ( $\Delta E$ ). For the example of a magnetostrictive rod with a magnetic field applied parallel to the rod length, a high applied magnetic field will not only orient the magnetic dipoles parallel to the rod length, but it will also make the dipoles more resistant to stresses imposed so as to rotate dipoles away from parallel to the rod length. This effectively makes the material stiffer, thus increasing the apparent Young's modulus. There are two measurements for Young's modulus, that at a

constant applied field,  $H$ , and that at a constant flux density,  $B$ . A constant flux density, corresponds to a fixed magnetic dipole orientation, which increases stiffness over that at a constant applied field because dipole rotation is restricted<sup>1</sup>.

The relationship between the two measurements is best examined with the introduction of a new quantity, the magnetomechanical coupling coefficient,  $k_{cc}^2$ . This quantity is determined by either solving the linear strain equation for stress, and inserting that result into the linear flux density equation, or by doing the reverse, which is solving the linear flux density equation for field, and substituting that result into the linear strain equation. After some reorganization of terms, the first method yields the following strain equation.

$$\varepsilon = \sigma \left( \frac{1}{E^H} \right) \left( 1 - \frac{dd^* E^H}{\mu^\sigma} \right) + B \left( \frac{d}{\mu^\sigma} \right) \quad (1.17)$$

The following quantity is then defined as the magnetomechanical coupling coefficient,  $k_{cc}^2$ .

$$k_{cc}^2 = \left( 1 - \frac{dd^* E^H}{\mu^\sigma} \right) \quad (1.18)$$

The value of  $k_{cc}^2$  is always between zero and one. This term provides a measure of the potential for conversion of mechanical energy and vice-versa.

The variability in permeability can be explained in a similar manner to the variability in Young's modulus. Not only is the permeability affected by the applied field,  $H$ , but also by the applied stress,  $\sigma$ . A high permeability corresponds to a material where the magnetic dipoles are free to rotate, but if a high stress is applied which resists

dipole rotation then the apparent permeability will decrease. Solving the linear strain equation for stress, inserting that equation into the linear flux density equation, rearranging and using the magnetomechanical coupling definition yields equation 1.20.

$$B = \varepsilon(dE^H) + H(\mu^\sigma)(1 - k_{cc}^2) \quad (1.20)$$

The permeability at a constant strain can be related to the permeability at a constant stress using the magnetomechanical coupling coefficient.

$$\mu^\varepsilon = \mu^\sigma(1 - k_{cc}^2) \quad (1.21)$$

Since the coupling coefficient is between zero and one it means the permeability at a constant strain will always be smaller than the permeability at a constant stress. Calkins<sup>4</sup> explains this by stating at a constant strain the material is mechanically blocked, preventing the magnetic dipoles from rotating.

#### 1.3.2.4 Extension of Material Behavior to Transducer Behavior

For transducer analysis not only does the magnetostrictive material's magneto-mechanical transduction performance need to be modeled but in addition the transducer's electro-magneto-mechanical performance needs to be evaluated. This complete electro-magneto-mechanical transduction can be modeled for simple cases using the following two linearized equations,

$$\begin{aligned} V &= Z_e I + T_{em} v \\ F &= T_{me} I + z_m v \end{aligned} \quad (1.22)$$

where  $V$  is the voltage across the transducer terminals,  $Z_e$  is the blocked electrical impedance,  $I$  is the current through the transducer,  $T_{em}$  is the electro-magneto-

mechanical transduction coefficient for electrical output from mechanical input,  $v$  is the transducer output velocity,  $F$  is the transducer force,  $T_{me}$  is the transduction coefficient from electrical input to mechanical output, and  $z_m$  is mechanical impedance of the transducer. The terms  $T_{em}$  and  $T_{me}$  typically include the effects of the magnetostrictive transduction of the core, while  $Z_e$  and  $z_m$  capture purely electrical and mechanical impedances of the transducer.

For a magnetostrictive energy harvester the coupling coefficient for electrical output from mechanical input is related to the rate of flux change ( $d\Phi/dt$ ) within the magnetostrictive core and the transducer electrical impedance characteristics. The basis of energy conversion from the rate of flux change to electrical output is the Faraday-Lenz law (eqn. 1.1). It relates the change in flux through the area surrounded by a single turn of wire to the induced voltage in the wire which will oppose the change in magnetic flux. Therefore, a stress induced change in the magnetostrictive rod flux density will produce a voltage proportional to the magnitude change in flux in a coil placed concentrically around a magnetostrictive rod because, in accordance with Faraday's law, it is "flux-linked" to the magnetostrictive rod. For a given change in flux, a coil with a greater number of turns,  $N$ , will produce a greater voltage output than a coil with fewer turns. However as the number of turns increases, so does the resistance of the coil. Hence, for design of an optimized coil there will be a trade off in performance associated with wire gauge and the number of turns so as to maximize output power. Thus even the terms  $Z_e$  and  $z_m$  in eqn 1.22 reflect electro-magneto-mechanical coupling in the transducer.

An additional consideration for dynamic operation is coil inductance. The coil inductance shows up in Eqn 1.22 as part of the electrical impedance, so as the coil inductance increases for a fixed coil voltage output, the output coil power will decrease. Induction of the coil will vary as a function of the permeability of the material at the center of the coil. An increase in this material's permeability will increase the coil inductance.

### **1.3.3 Performance considerations**

This section will examine external factors which affect magnetostrictive performance. All of these factors can be controlled or mitigated to some extent through good transducer design to yield better performance.

#### **1.3.3.1 Prestress**

Prestress has several performance effects, the first of which relates to the total strain capability of the material. Without a preload the magnetic domains in the material are randomly oriented, which affects the material size or length. Applying a prestress rotates the magnetic domains perpendicular to the applied load, thereby reducing the length in the direction of the load. Then when a magnetic field is applied the magnetic domains can rotate from perpendicular to the preload to parallel to the preload which yields a greater overall magnetostriction strain due to the decreased initial length of the material. This effect can be quantified by looking at  $\lambda$ - $H$  curves for discrete prestresses, such as in Fig. 1.2. The slope and peak magnitude of the

curve will increase with increasing prestress until a certain point, after which significantly higher magnetic bias will be required to achieve maximum magnetostriction and the resulting curve slope will decrease. This is because more input magnetic field is required to overcome the prestress on the material to achieve the same magnetostriction.

Many studies have been performed to analyze or have noted the effect of prestress on the properties of magnetostrictive materials, and hence their performance.<sup>3,15,21,24</sup> Kellogg<sup>15</sup> noted that a specific amount of prestress was required to align a single crystal Galfenol rod along the easy axis perpendicular to the rod length. He also noted an increase in the elastic modulus with an increase in the prestress.

### **1.3.3.2 Magnetic Bias**

Magnetic bias affects a magnetostrictive material in similar ways to prestress, therefore performance optimization of magnetostrictive transducers involves a coupled optimization of bias and prestress. An applied magnetic field changes the orientation of the magnetic domains which in turn alters the elastic or physical dimensions of the material. A significant distinction in the effect prestress and bias have on a magnetostrictive is how the material reacts in relationship to the direction of the applied prestress or bias. In the case of a magnetostrictive rod, a prestress parallel to the length of the rod will reduce the length of the rod and force the magnetic domains perpendicular to the applied load. A magnetic bias applied parallel

to the length of the rod will rotate the magnetic domains parallel to the magnetic field which leads to an increase in rod length. Thus, to optimize an energy harvester it will be important to identify the prestress and bias combination that maximizes the coupling coefficient,  $d^*$ .

### 1.3.3.3 Eddy Currents

Eddy currents are currents induced in a material that resist changes in the magnetic field. The basis for these induced currents is the Faraday-Lenz law which in this case states that induced currents in a conductor will be related to the negative time rate of change of the magnetic flux,  $\Phi$ . The negative means that these currents will oppose the change in flux, yielding a lower net flux change through the material. These currents only occur in magnetostrictives during dynamic operation and only become a significant problem at high frequencies. The “cut off” frequency above which eddy currents become a significant problem is,

$$f_c = \frac{2\rho}{\pi D^2 \mu_\epsilon} \quad (1.23)$$

where,  $\rho$  is the electric resistivity,  $D$  is the rod diameter and  $\mu_\epsilon$  is the permeability at constant strain. Curves of the approximate cutoff frequency for Terfenol-D and Galfenol versus rod diameter are shown in Fig. 1.3. Since operation at frequencies below 100 Hz was targeted in this study, and rod diameters of .25" were used, consideration of eddy currents and the use of laminated samples to reduce eddy currents were not necessary. If magnetostrictive energy harvesting from a high

frequency mechanical input were to be investigated, then eddy current losses would have to be considered.

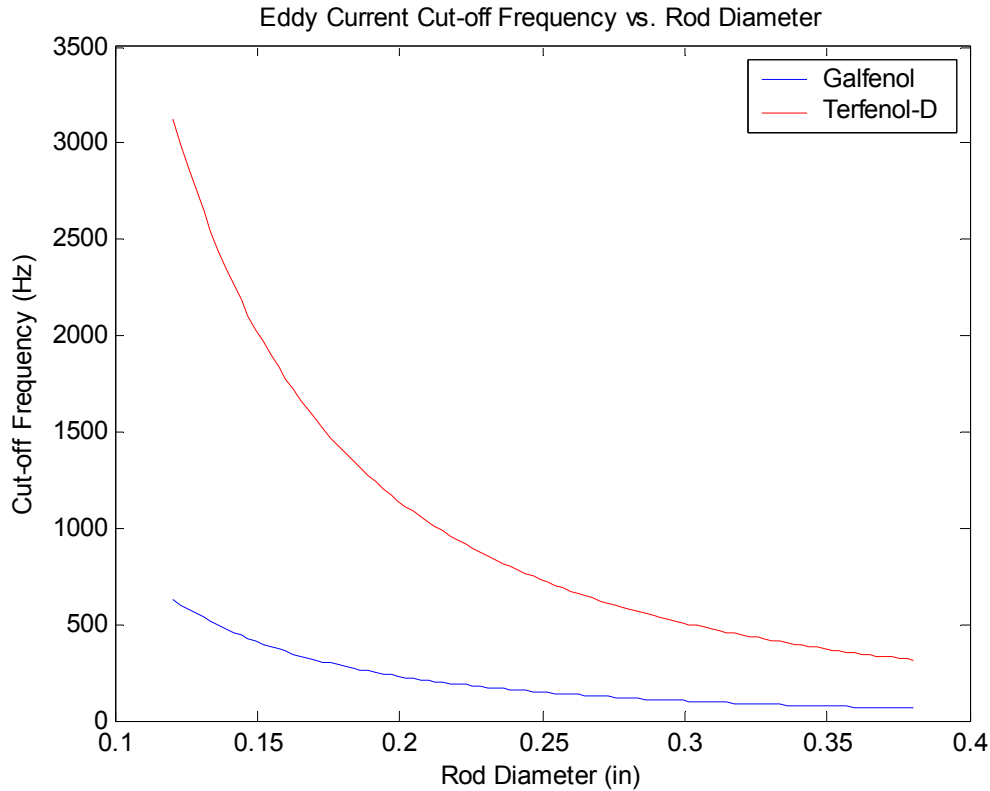


Figure 1.3: Eddy current cutoff frequency relationship to rod diameter for Terfenol-D and Galfenol using the relative properties of each material. Relative permeability of 10 and 100 used for Terfenol-D and Galfenol respectively. Resistivity shown in table 1-1.

#### 1.3.3.4 Temperature Effects

The stoichiometry of Terfenol-D has been optimized for operation at room temperature. There is a significant decrease in performance with a decrease in temperature because different crystal axes with less magnetostriction dominate over those axes which produce large magnetostriction.<sup>4</sup> Terfenol-D performance does decrease some with temperature above room temperature, though not to the same

extent as with low temperatures. If the material temperature reaches the Curie temperature of the material then the crystal structure will no longer be ferromagnetic and will not exhibit magnetostriction. Kellogg<sup>15</sup> performed temperature tests on single crystal Galfenol and found similar temperature related performance trends to those found for Terfenol-D but with much lower sensitivity to temperature change. The tests in this study were performed at room temperature and were short enough in duration that no significant heat was generated due to transducer operation and the magnetostrictive material temperature was not significantly altered during testing.

## **2. TRANSDUCER DESIGN AND TESTING METHODOLOGY**

### **Introduction**

This chapter first describes the design of the magnetostrictive energy harvesting transducer utilized during testing. A description of the testing methodology and equipment used follows and the chapter concludes with an overview of the experiments conducted to obtain the results presented in the experimental results chapter.

### **2.1 Transducer Design**

Goals of this project were two fold. The first goal was to design and implement a transducer that can be attached to an arbitrary vibrating surface and act as a vibration sink. The second goal was to demonstrate conversion of ambient mechanical energy into longitudinal strain energy of the harvester's magnetostrictive element and thereby into a time-varying magnetic field that can be used to produce electrical power.

#### **2.1.1 Overview**

To implement energy harvesting with a typical fixed-free commercially available magnetostrictive transducer requires that the “free” end is attached to the vibrating structure and the actuator base or “fixed” end is attached to a non-vibrating structure

(Fig. 2.1a). This would require a stiff mounting system from the fixed transducer end to the non-vibrating structure, which in practice could prove difficult and bulky. Furthermore, such a mounting system would introduce a major impedance change to the structure's stiffness and would most likely alter the structure's displacement characteristics. This type of mounting system would be required to ensure the energy of the vibrating structure is transformed into strain energy of the magnetostrictive rod rather than rigid body motion of the actuator. The approach illustrated in Fig. 2.1b is self-contained in that it is attached to a vibrating surface at one location and becomes a point mass load, and while the device attachment plate undergoes rigid body motion, the upper portion of the device is free to move as a rigid body at low frequencies but can be designed to produce large internal oscillations, especially when the base excitation occurs at frequencies near its resonances. This latter approach is used in this thesis.

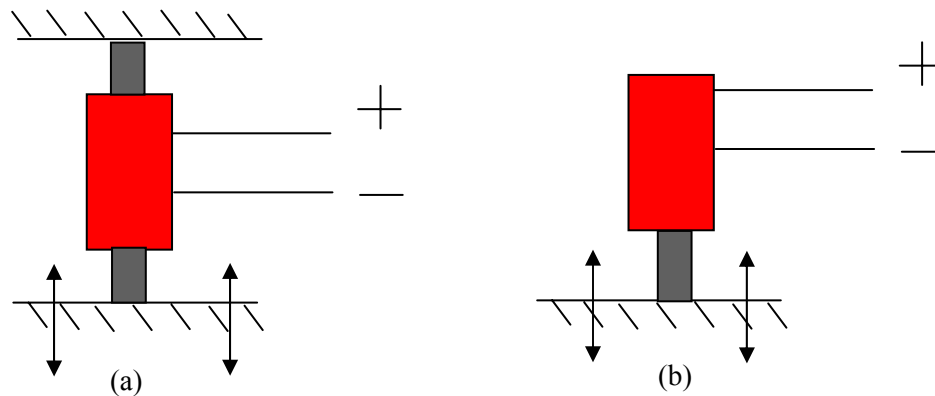


Figure 2.1: Two types of energy harvesting transducers.

To tune the resonant frequencies of this prototype energy harvesting transducer to frequencies other than just the first axial mode of the magnetostrictive sample, the design implemented in this study uses the tunable resonant response of a fixed – simply supported – free beam to produce dynamic stress in the magnetostrictive rod.

The energy harvester is designed to be attached to an arbitrary vibrating host structure at its base, which consists of  $\frac{1}{2}$ " thick, 2" wide and 12" long 6061-T6 aluminum. A  $\frac{1}{2}$ " thick aluminum bar is used to approximate a rigid support for the fixed end of the resonant beam on the top of the energy harvester (shown at the right of fig. 2.2). A  $\frac{1}{8}$ " thick,  $\frac{1}{2}$ " wide, 11" long piece of 6061-T6 aluminum serves as the tunable resonant fixed – simply supported – free beam. At the right end of Fig. 2.2 the beam is clamped to the vertical aluminum support via a top aluminum piece which is screwed into the vertical support over the end of the beam. The magnetostrictive transduction element, a  $\frac{1}{4}$ " diameter and 2" long cylindrical rod of either research Galfenol, production Galfenol or Terfenol-D, is introduced as an intermediate simply supported boundary condition, approximately 2.2 inches to the left of the cantilevered boundary. The left end of the beam is loaded with an end mass and with tension springs, both of which can be varied to achieve different beam resonant frequencies and to control the preloads on the magnetostrictive element.

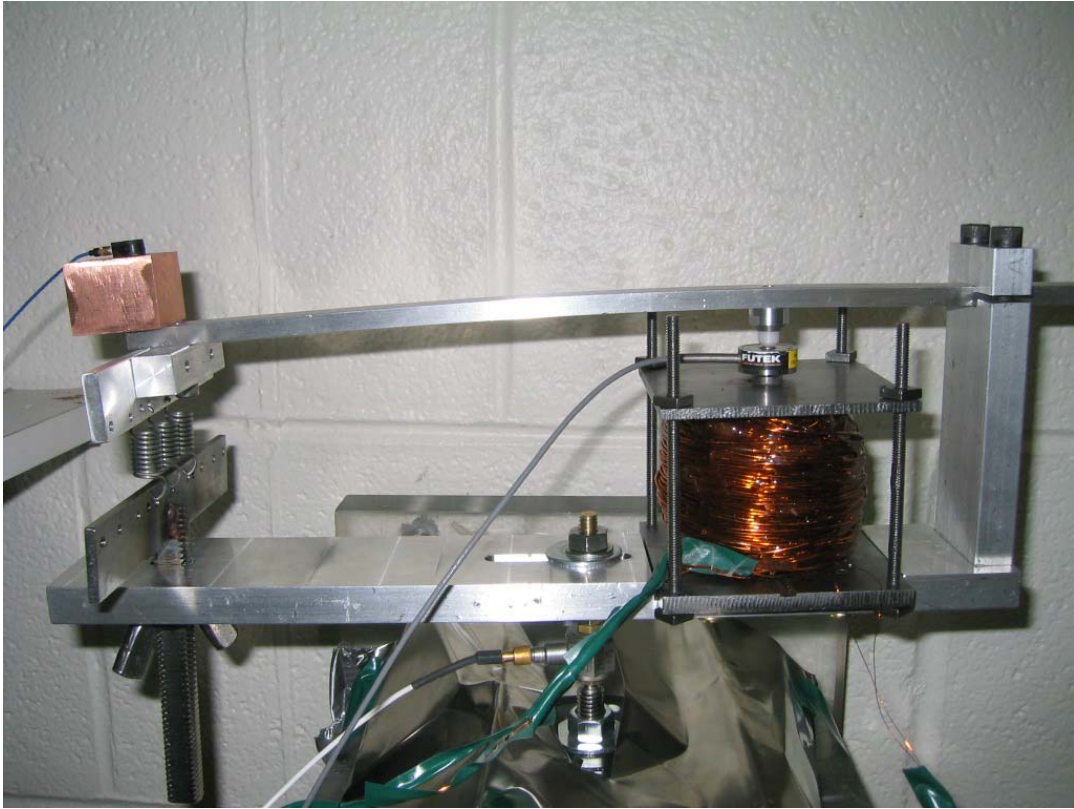


Figure 2.2: Picture of the energy harvesting transducer used in this study.

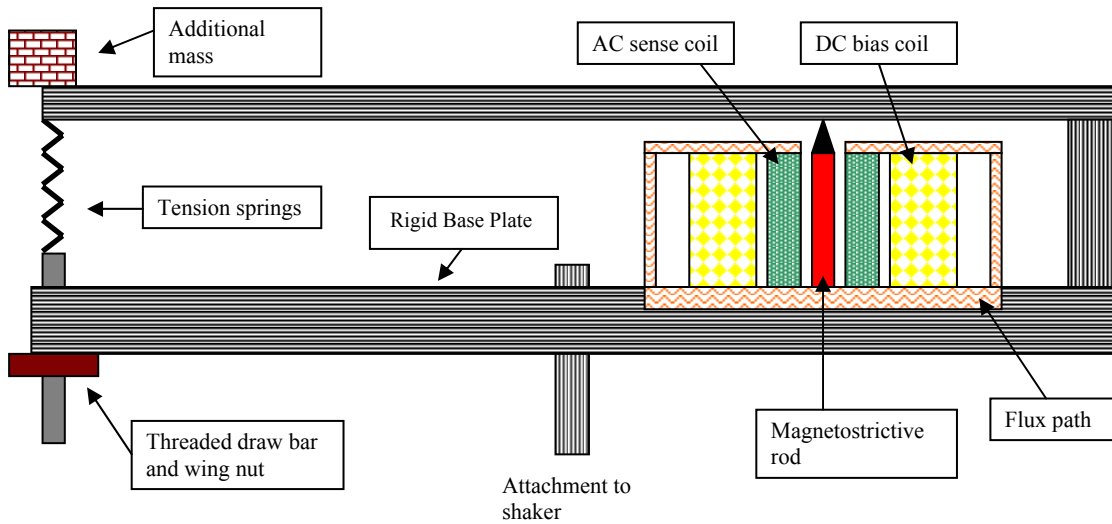


Figure 2.3: Diagram of the energy harvesting transducer designed for this study

### 2.1.2 Magnetic Circuit Design

The magnetostrictive transduction component ideally consists of a self-contained magnetic circuit. The circuit includes a bias coil and a pick-up sense coil. The upper and lower surface of the circuit is comprised of two 3" square, 1018 steel plates. The lower circuit surface  $\frac{1}{4}$ " thick plate was inserted into a milled groove in the rigid aluminum base. A  $\frac{1}{8}$ " thick plate with a  $\frac{1}{2}$ " diameter center hole centered on top of the magnetostrictive rod formed the upper circuit surface. The  $\frac{1}{2}$ " diameter hole allows a load cell to pass through the top steel plate and interface both the bottom of the resonant beam and the top of the magnetostrictive rod. The magnetostrictive rod itself is located at the center of the magnetic circuit. The top of the rod contacts a 1018 steel end cap with a .1" diameter milled cut to center the rod. This end cap sits in the center of the hole in the top steel plate and is connected to that plate via flexible magnets. Four 8-32 1018 steel threaded rods connect the top and bottom steel plates on their edges. A  $\frac{1}{4}$ " diameter, .1" deep cut is made in the center of the lower steel plate to hold the bottom end of the magnetostrictive rod, orienting the rod perpendicular to the aluminum base as illustrated in Fig. 2.3.

During testing this design proved to provide an inadequate magnetic circuit. The two most likely weak points in the current magnetic circuit design are as follows. One difficult area was the air gap between the moving steel end cap and the non-moving top steel plate. The current design used flexible magnets to bridge this gap. Another problem could be inadequate sizing and number of threaded steel rods that connect the top and bottom steel plates.

### **2.1.3 Prestress Adjustment Design**

The 1018 steel end cap on top of the magnetostrictive rod is screwed into a non-magnetic 500 lb<sub>f</sub> Futec static load cell (model: L1635), which in turn is interfaced to the resonant beam via a hard plastic impact-hammer tip screwed into the top aluminum beam. This rounded hammer-tip interface is positioned to press against the slightly convex top of the static load cell to provide a simply supported condition and minimize losses in transferring beam bending motion into axial motion of the magnetostrictive rod.

The free end of the top aluminum beam is attached to the base via three extension springs connected to a threaded draw bar, which slides freely in a through hole in the base (left side of Fig 2.2). The initial deflection of the extension springs is adjustable via a wing nut on the threaded draw bar on the bottom side of the aluminum base. An additional .3 lb mass is attached to the free end of the beam to lower the first natural frequency. The combination of the weight of the top beam, end mass and deflection of the extension springs provides the preload on the magnetostrictive rod. The effective magnitude of this preload was measured with the static force load cell and was combined with the known area of the magnetostrictive rod to determine prestress. The prestress level was set by varying the adjustment position of the tension springs with the wing nut.



effective spring constant of the tension springs which affect the frequency response, a Hamilton/Rayleigh energy method was employed. The results were obtained using Matlab and the code can be found in appendix A.

The method to solve for the first natural frequency begins with Hamilton's principle (eqn. 2.2).

$$\delta \int_{t_1}^{t_2} (T - V) dt = 0 \quad (2.2)$$

The above equation begins with the system kinetic energy,  $T$ , and potential energy,  $V$ , and then variational principles are applied which yields the system equation of motion. Though this method was employed, the end result is simply Rayleigh's quotient which states that the square of the first natural frequency is equal to the ratio of the potential (stiffness) energy to the kinetic (mass) energy present in the equation of motion. The total kinetic energy of the system includes the distributed kinetic energy of the beam due to its mass and the concentrated kinetic energy of the mass at the beam tip. The total potential energy of the system includes the distributed potential energy of the beam due to its stiffness and the concentrated potential energy of the tension springs at the beam tip. The equations for each of these energy terms are presented below.

$$\begin{aligned}
T_{beam} &= \frac{1}{2} \int_0^L m\dot{w}(x)^2 dx \\
T_{mass} &= \frac{1}{2} M\dot{w}(L)^2 \\
V_{beam} &= \frac{1}{2} \int_0^L EI(w'')^2 dx \\
V_{springs} &= \frac{1}{2} kw(L)^2
\end{aligned} \tag{2.3}$$

The resulting form of Rayleigh's quotient for this problem is presented in equation (2.4), which results from applying Hamilton's principle with the energy terms above.

$$\omega^2 = \frac{\int_0^{L1} EIw(x)'''' dx + \int_{L1+L2}^{L1+L2} EIw(x)'''' dx + kw(L)}{\int_0^{L1} mw(x) dx + \int_{L1+L2}^{L1+L2} mw(x) dx + Mw(L)} \tag{2.4}$$

Since  $w(x)$  at  $x$  equal to  $L1$  is forced equal to zero due to the simply supported condition, the beam integrals are split into two, and  $w(x)$  equation for each interval is used. Since the beam displacement curve equation,  $w(x)$  is an unknown quantity, it was decided to determine the static beam displacement curve and use that in equation (2.4) as a good approximation. The static beam displacement curve was determined, by using equation (2.5), the differential equation of an elastic curve.

$$EI \frac{d^2w}{dx^2} = EIw'' = M(x) \tag{2.5}$$

The moment equation,  $M(x)$  is determined using the distributed and concentrated forces on the beam. Then  $w''$  is equal to the moment equation divided by the product of Young's modulus of the beam,  $E$ , and the moment of inertia,  $I$ . Finally the beam vertical displacement equation,  $w(x)$  is determined by integrating twice with respect to  $x$ , and the resulting constants are determined using boundary conditions. All

calculations and equations are shown in the Matlab code in Appendix A. This method resulted in selection of parameters (dimensions, spring constants, etc) that should yield a first natural frequency of 40.3 Hz.

### **2.1.5 Bias Coil and Sense Coil Design**

The magnetostrictive rod is surrounded by a ~3000-turn, 38-gauge AC sense coil which in-turn is surrounded by a 1000-turn, 20-gauge DC bias coil. The bias coil is used to provide a variable external DC magnetic field,  $H$ , to the magnetostrictive rod. The adjustable bias from the DC coil and the adjustable prestress from the tension springs allow for coupled optimization of performance, the importance of which is explained in section 1.3.3.2.

An AC voltage is generated in the sense coil by changes in magnetic flux in the magnetostrictive rod, which are induced in response to load-induced mechanical strain of the magnetostrictive rod. Initially a coil with a high  $n$ , or turns per unit length was selected since as Faraday's law, eqn. 1.1, suggests, the voltage generated for a given rate of flux density change will increase in proportion to the number of turns of the coil. Near the end of the testing this high  $n$  (~3000 total turns), 38 gauge, 127 ohm, sense coil broke, due to mechanical loading during handling. It was replaced with a 28 gauge, 20 ohm, ~1500 turn sense coil to finish the full circuit testing. A smaller gauge, lower  $n$ , coil was made to replace the previous coil for two reasons. First, a coil made of smaller gauge, larger diameter wire is less likely to break than the first coil. Second, a coil with a different  $n$ , yields a different voltage

response from the coil, allowing performance comparisons to be made between the different coils from test results run under the same conditions.

## **2.2 Test Procedure**

Before performing dynamic tests, the range of bias fields needed to center operation about roughly one half of the saturation strain length for both the Terfenol-D and Galfenol rods was determined. As explained in section 1.3.2.2., magnetostriction is dependant on the applied field. To determine these ranges, quasi-static  $\lambda$ - $H$  (strain vs. applied field) curves were collected for a Terfenol-D and research grade Galfenol rod under prestresses of 1, 2 and 3 ksi. Since this was an actuator test and the goal was to measure the resulting rod strain for applied magnetic fields, the transducer base was clamped to a test table to prevent any motion of the base or fixed end of the transducer. These tests were performed using the energy harvesting transducer with a DVRT placed directly above the magnetostrictive rod on the top aluminum beam. DVRT stands for ‘differential variable reluctance transducer,’ and it provides accurate position information of its tip. The DVRT from MicroStrain, Inc used in these experiments (model: HSGDVRT6) has a resolution of 2.0 microns.

A magnetic bias is provided to the magnetostrictive rod by applying a DC voltage across the “DC coil.” The voltage applied across the coil correlates directly to the magnetic field produced. This conversion from applied voltage to magnetic field was calibrated utilizing measurements from a hand-held gauss probe in the center of the DC coil for various voltages and then creating the linear interpolation shown in Fig.

2.5. The interpolation equation shown in Fig. 2.5 was then used during all resulting tests to convert applied voltage into the applied magnetic field.

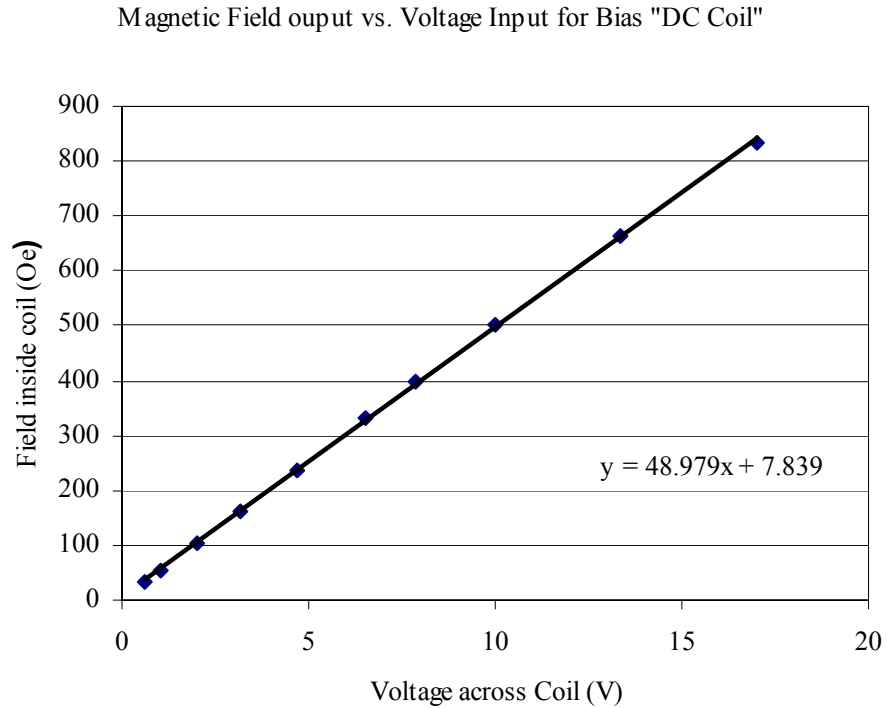


Figure 2.5: Output field at radial center of the bias coil along the axis vs. applied DC voltage.

Displacement measurements were taken while sweeping up and down in input voltage to get complete strain hysteresis data. Voltage readings from the DVRT were converted to millimeter displacement using the supplied conversion factor from MicroStrain, Inc., then converted to inches and then into strain using the known length of the magnetostrictive rods. Plots, presented in appendix B, were produced using the collected magnetic field and strain data.

All dynamic tests were run on a 75 lbf shaker from Labworks, Inc (model: ET-139) with the transducer locked to the shaker with a threaded stinger and nut that passes through the aluminum base of the transducer. A 10 lbf PCB dynamic load cell (model: 208C01) threaded in between the shaker and the transducer provided force feedback data that was used in a control loop in conjunction with a Data Physics shaker controller (model: U1 8222). Power was provided to the DC coil via two 12 volt car batteries in series with a rheostat (variable resistor). A diagram of the setup is shown in Fig. 2.6. This setup, rather than utilizing a DC power amplifier, ensured that no AC noise signals from a floating ground in the laboratory would interfere with the test readings. Since the sense coil is inside the bias DC coil it acted as a transformer when AC signals were present in the bias coil which added noise to the harvested power signals. A knob on the rheostat allows for continuous adjustment of magnetic bias during testing, because it controls the voltage drop across the DC coil.

Electrical output from the energy harvester is dependant on both the magnetic bias and prestress on the magnetostrictive rod. To achieve an efficient representation of output performance, curves of the sense coil output at varying magnetic biases were repeated for three or more constant prestress levels and the resulting performance curve for each prestress was plotted on the same graph.

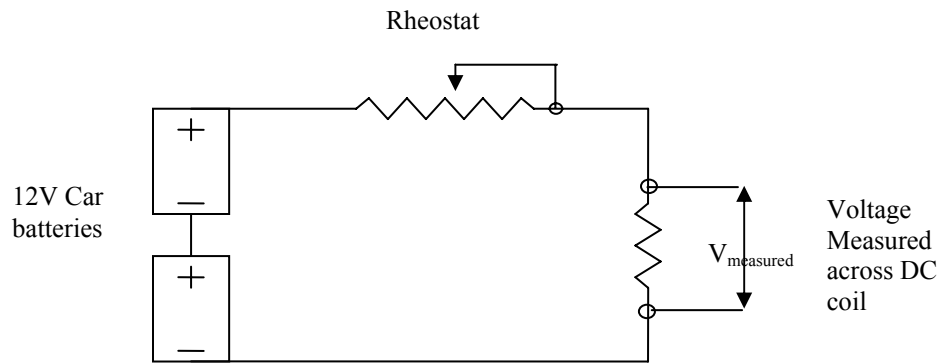


Figure 2.6: Diagram of Power supply setup to control the DC magnetic bias coil.

Data from sine sweep tests of 25 to 125 Hz provided the natural frequencies of the transducer in that range. Then dwell tests at the slightly different resonant frequencies for the different magnetostrictive rods determined from the sweep tests were run at fixed prestresses of 1 ksi to 3 ksi in 1 ksi increments. Open circuit sense coil measurements were then recorded for a range of magnetic bias suggested from the quasi-static  $\lambda$ -H curves. Tests for comparison of performance at different prestress and magnetic bias settings were conducted using a 2 lb peak sine force input from the shaker to the transducer. Sweep tests at 2 ksi and different biases were performed to better illustrate how drastically bias affects performance and sensitivity and to verify the results from the dwell tests. Then sine sweep tests were again performed at different prestresses but at the determined optimum bias for each prestress from the previous tests. This was done to determine whether the same output sense coil performance could be achieved at different prestresses if the optimum bias was applied. Finally, more sweep tests at the same prestress and bias, but different mechanical force inputs were run to examine the linearity of open circuit

electrical output to mechanical input. These tests are summarized in table 2.1 at the end of the chapter.

To collect a more meaningful measurement of electrical output from the energy harvesting transducer and to verify material-based comparisons of performance from open circuit tests, full circuit tests were run. Instead of measuring the RMS voltage across the unconnected leads of the sense coil, a resistor decade box was connected between the two leads to create a full circuit. Now measurements of RMS voltage were measured across the load resistance in the circuit. The resulting circuit diagram is shown in Fig 2.7. The resistance across the leads was then varied using the resistance decade box and the resulting change in voltage drop across this load was recorded.

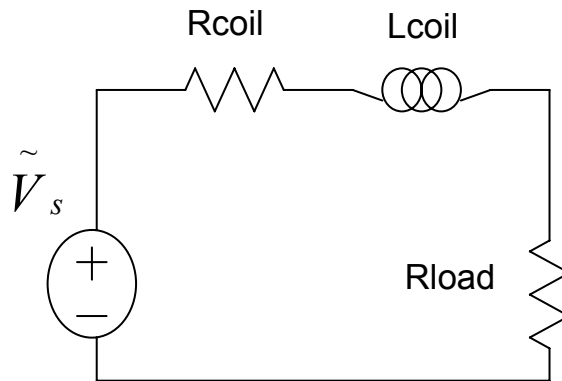


Figure 2.7: Full circuit test setup, including representation of the sense coil and the load resistance.

The sense coil is modeled as an AC voltage source in series with a resistance and an inductance. The load resistor represents a component to which energy is supplied from the energy harvesting transducer and it is modeled as resistance in series with

the coil resistance and inductance. This circuit models an application for which power is continuously supplied to a device rather than using the harvested power to charge a battery. Dissipated power or the supplied power to the load resistance is calculated using equation 2.6. Plots of supplied power vs. load resistance were then created for the energy harvester performance when using Terfenol-D, Research Galfenol and Production Galfenol magnetostrictive rods.

$$\tilde{P}_{load} = \frac{\tilde{V}_{load}^2}{R_{load}} \quad (2.6)$$

Inductance measurements of the sense coil were recorded using a handheld Extech LCR meter (model: 380193) at two test frequencies for all three magnetostrictive materials. Inductance data was taken at different prestress and magnetic biases. This information was then used in the analytical model to determine the optimum load resistance for each coil.

Table 2-1: Examination of the different tests performed; the overall test purpose, the variables involved, materials tested, output measurement type and additional knowledge gained.

<b>Test Type and order in which performed</b>	<b>Main Purpose</b>	<b>Additional knowledge gained</b>	<b>Variables</b>	<b>Materials Tested</b>	<b>Output Measurement</b>
1. $\lambda$ -H	To determine the range of bias fields and relative magnetostriction between materials		Bias and Prestress	Terfenol-D, Research Galfenol	Transducer displacement at the rod location
2. Sweep	To determine transducer resonant frequencies and verify transducer operation		Frequency, Bias and Prestress	Terfenol-D, Research Galfenol, Production Galfenol	Open circuit sense coil RMS voltage
3. Dwell	To determine the optimum bias field versus prestress	Terfenol-D hysteresis affect on optimum bias	Bias and Prestress	Terfenol-D, Research Galfenol, Production Galfenol	Open circuit sense coil RMS voltage
4. Sweep (fixed prestress)	To verify previous optimum bias dwell test results		Frequency and Bias	Terfenol-D, Research Galfenol	Open circuit sense coil RMS voltage
5. Sweep (fixed prestress and bias)	To compare performance at different prestress with the optimum bias for each prestress applied	Affect of prestress on the resonant frequency	Frequency, prestress, (bias dependant on prestress)	Terfenol-D, Research Galfenol	Open circuit sense coil RMS voltage
6. Sweep (mechanical input)	To obtain relationship between electrical output and mechanical input	Affect of mechanical drive level on the resonant frequency	Frequency, Mechanical peak force input	Terfenol-D, Research Galfenol	Open circuit sense coil RMS voltage
7. Full Circuit dwell	To determine real power output and the optimum load resistance	Coil inductance affect on peak power output (material related)	Load Resistance	Terfenol-D, Research Galfenol, Production Galfenol	Full circuit voltage across load resistance and power delivered to the load resistance

## 3. EXPERIMENTAL RESULTS

### 3.1 Static Strain-H Curves

Results from the  $\lambda$ - $H$  tests are shown in Fig. 3.1 for both research grade Galfenol and Terfenol-D for a prestress of 3.9 ksi. All performed  $\lambda$ - $H$  test results are in Appendix C. As expected the Terfenol-D rod has a much higher total strain response than the Galfenol, but it also requires a significantly higher field to reach saturation strain. Results from other prestress tests, given in Appendix C, yielded similar results. These tests occurred before the production grade Galfenol samples were obtained, but since production grade Galfenol is similar to research grade the  $\lambda$ - $H$  test for production grade Galfenol was not performed. This  $\lambda$ - $H$  test is an actuator based test, but yields a baseline of what field ranges affect the magnetization state of each magnetostrictive. The slope of the  $\lambda$ - $H$  curve corresponds to the coupling coefficient,  $d$ . Also this test did not yield the free saturation magnetostiction strain response of the material because the strain of the rod is resisted by the stiffness of the beam and the springs at the end.

### 3.9 ksi Galfenol and Terfenol-D

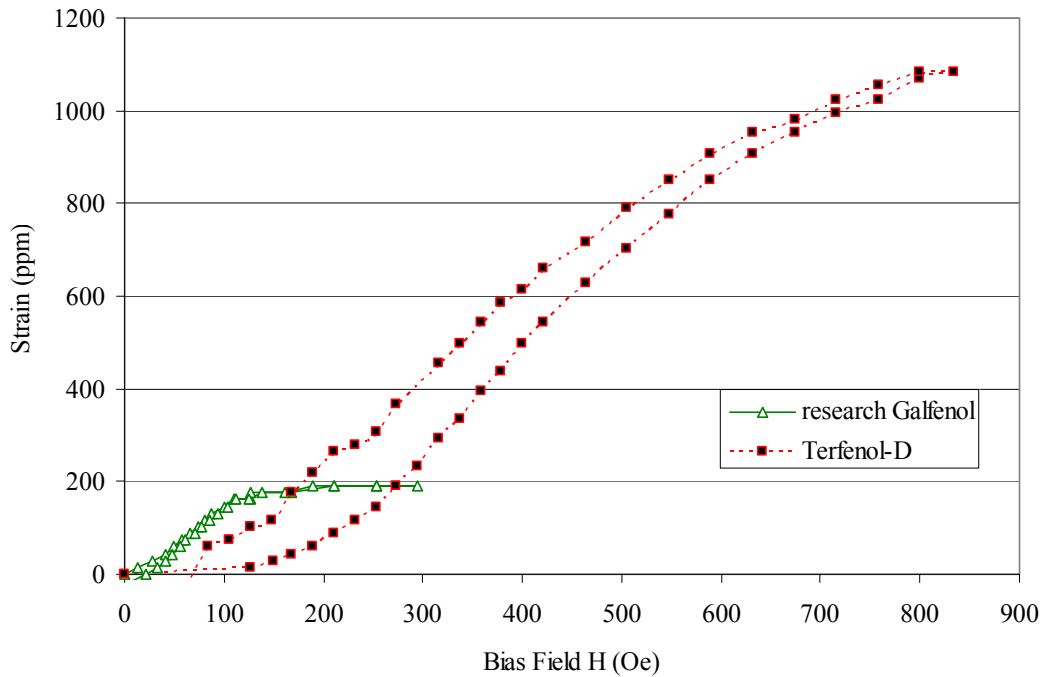


Figure 3.1: Static Strain-H curve for research Galfenol and Terfenol-D under a 3.9 ksi prestress.

### 3.2 Sine sweep tests to characterize transducer performance

Sine sweep tests at 2-lb peak force show the resonant response of the top aluminum beam via autospectra of responses measured with a miniature PCB accelerometer (model: 352A24) bonded to the mass at the free end. Figure 3.2 shows the accelerometer data for 25-100 Hz for a Terfenol-D rod, research and production Galfenol rod configuration at 2 ksi prestress. Even though the only difference in the transducer is the rod, the accelerometer readings have slight differences. Both peaks are present in each response but the resonance points for all the rods are slightly different. This can be explained by the different Youngs modulii of each material<sup>4,21</sup>

and variation associated with transducer assembly. Figure 3.3 shows the normalized response of the open circuit sense coil voltage output, scaled so the maximum output occurs at 1 on the y-axis. An aluminum rod of the same dimensions as the magnetostrictive rods replaced the magnetostrictive element for a sweep test to verify that the induced voltage in the sense coil is directly attributable to the magnetostrictive element. The frequency autospectra results for the accelerometer retained the same characteristic double peak output as for the magnetostrictive rods, but as expected there was no sense coil output at any frequency.

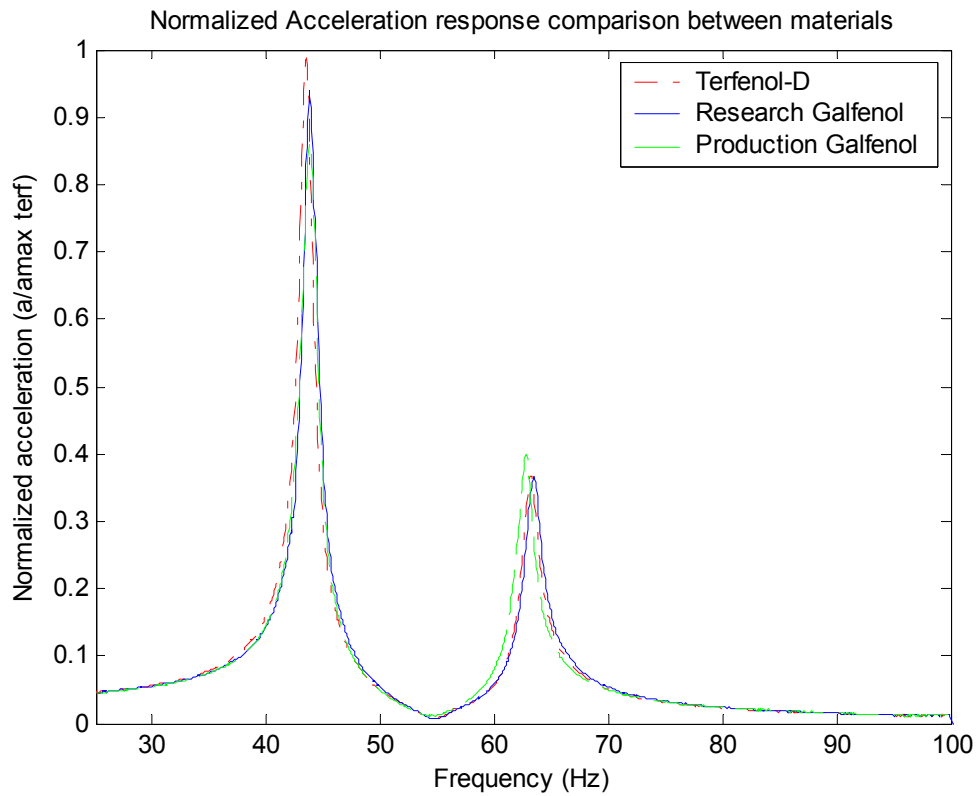


Figure 3.2: Normalized frequency vs. acceleration curves for Terfenol-D, research and production Galfenol. Plots are all normalized to the maximum tip acceleration of the Terfenol-D plot.

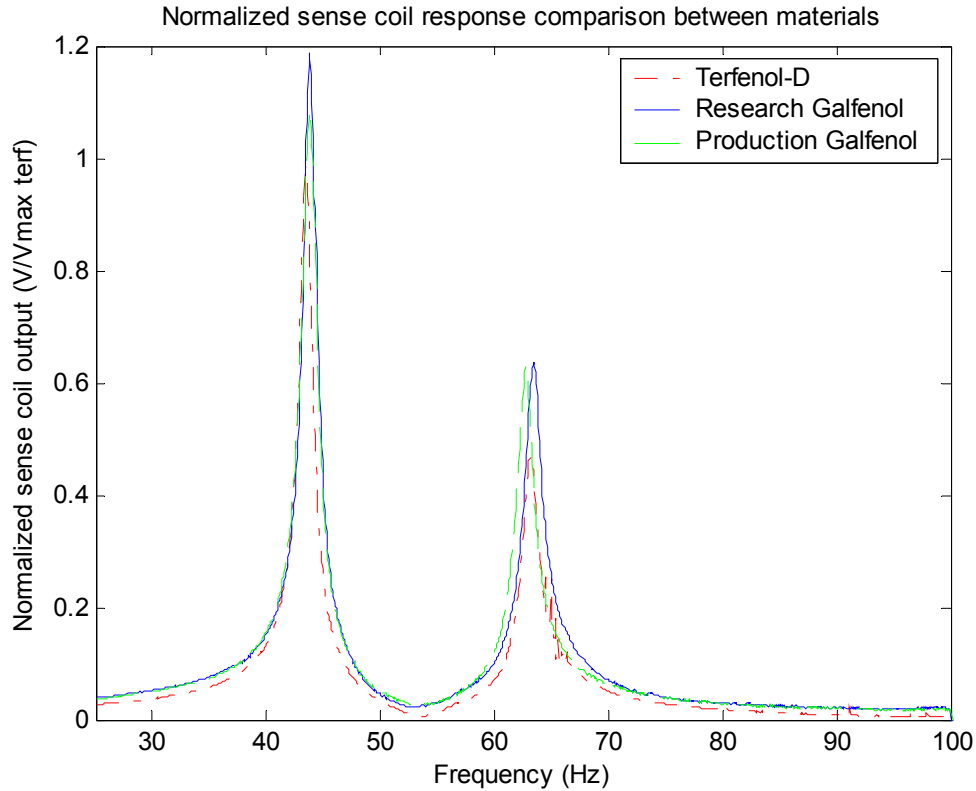


Figure 3.3: Normalized open circuit sense coil voltage response for Terfenol-D, research Galfenol and production Galfenol as the magnetostrictive. Curves are normalized with respect to the Terfenol-D curve peak open circuit voltage output. This is why the graph exceeds a value of one on the y-axis.

Initial tests yielded fluxuations of greater than 50% in the sense coil output at the system first resonant frequency of roughly 45 Hz, while responses at the second peak, at roughly 58-63 Hz were quite reproducible. These measurements were revisited after completion of most of this study and this fluxuation could not be reproduced. As a result the second peak shown in Figs 3.2 and 3.3 was used in conducting the dwell tests described in the next section. Although the second peak is close to 60 Hz, it is not a result of 60 Hz noise, as the previously mentioned test where an aluminum rod was placed instead of a magnetostrictive rod proves because there was no sense coil output between the 25-100 Hz range tested. Had there been a noise source at 60

Hz influencing the sense coil output, the sense coil output for the aluminum rod case would not have been zero at 60 Hz.

### **3.3 Sinusoidal dwell tests**

Sinusoidal dwell tests of 2-lb peak force input at the second resonant frequency of the system were conducted to characterize the energy harvester performance with respect to prestress and magnetic bias. Figures 3.4-3.7 show the open circuit voltage measured across the 127 ohm sense coil during dwell tests of the Terfenol-D and research Galfenol rods on two different days as both prestress and magnetic bias were varied. For these tests the prestress was set to 1, 2, or 3 ksi by adjusting the springs at the end of the aluminum beam, the shaker was operated at a fixed frequency, and the DC applied magnetic field was varied from 25 Oe up to as much as 900 Oe. In Figs. 3.4 & 3.6 the dwell frequency of ~61 Hz was determined based on energy harvester resonance under 3 ksi prestress. In Figs. 3.5 & 3.7 tests were conducted at a dwell frequency of ~59 Hz based on transducer resonance under 2 ksi prestress. The data points in the following graphs represent the discrete measurement values and the curves associated with each graph are simply a smoothed fit to the discrete values.

As the prestress on the magnetostrictive core increases so does the magnetic bias necessary to achieve peak performance. This can be explained at the material level by analyzing magnetic domain position as described in sections 1.3.3.1 and 1.3.3.2. The mechanical prestress applied to the rod ends creates an energy minimization state with the magnetic domains flat, perpendicular to the rod while the application of a

magnetic field parallel to the rod creates an energy minimization state with the domains parallel to the rod. Maximum sense coil output is achieved when the magnetic domains have the greatest ability to rotate, or when magnetic and mechanical energies are balanced. Thus, as prestress increases one should expect a proportional increase in the magnitude of optimum magnetic bias.

Trends for identification of the optimal prestress necessary to achieve peak performance are not readily apparent from the results in Figs. 3.4-3.7. The most likely explanation for this is the testing procedure, as is quantified in section 3.5, and specifically in Figs. 3.10 and 3.11. These figures show that the frequency of the resonant peak shifts slightly for different prestresses and that, due to the narrow bandwidth of the resonant peaks, off-resonance excitation can significantly lower the sense coil voltage. For each set of dwell tests in Figs. 3.4.-3.7, only one sweep test at one prestress was run to determine the dwell frequency for that figure. All sweep tests were run at prestresses of either 2 ksi (Figs. 3.5 & 3.7) or 3 ksi (Figs. 3.4 & 3.6), which predisposed the magnitude of the sense coil output for the dwell tests to favor that prestress since the transducer is operating at precisely the resonant frequency for that prestress. Unfortunately this did not become apparent until the results were being analyzed, or additional dwell tests at the resonant frequency associated with each prestress would have been conducted. This is left as a suggestion for future work.

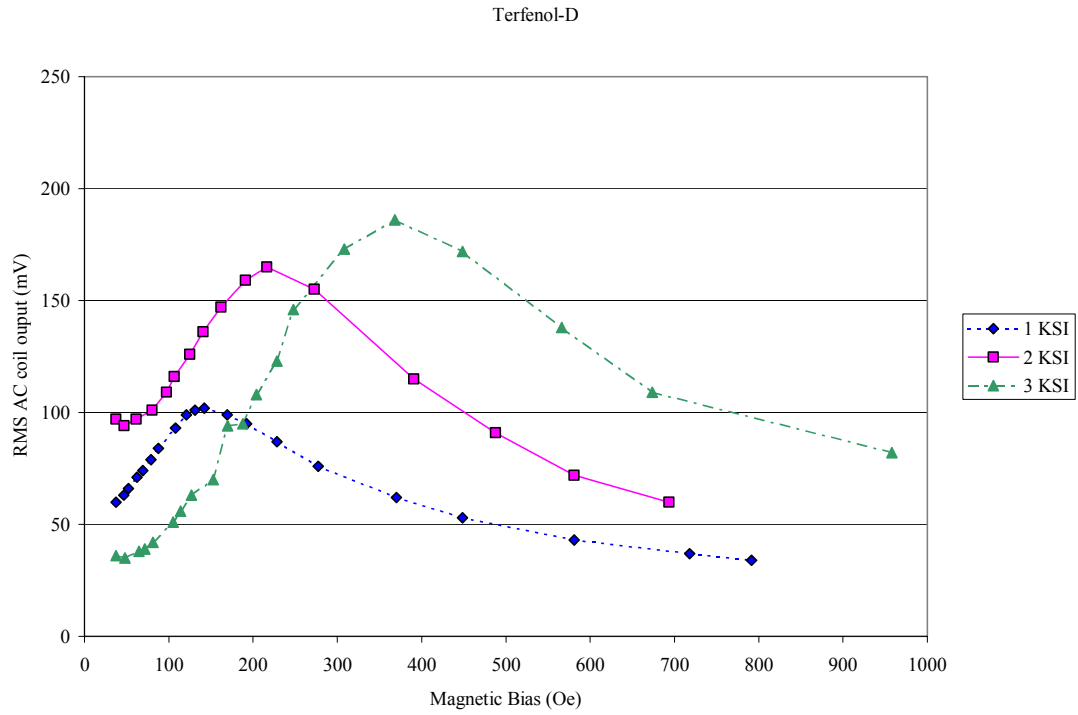


Figure 3.4: Terfenol-D sweep tests at for 1, 2 and 3 ksi prestress. Data taken on 4/13/05.

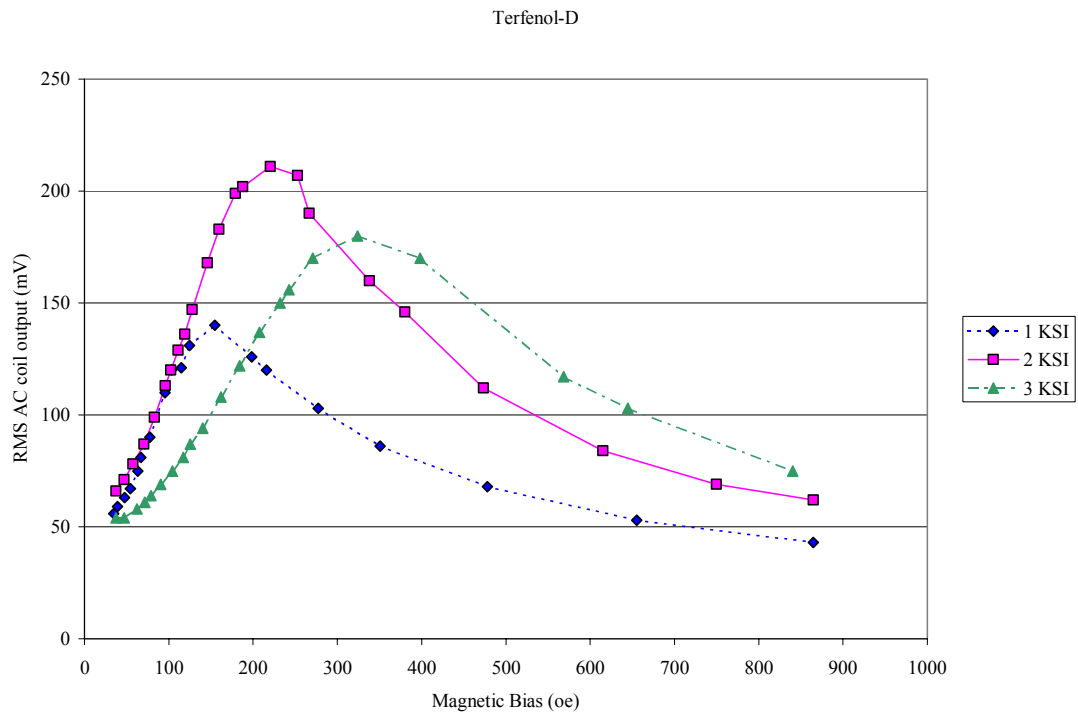


Figure 3.5: Terfenol-D sweep tests at 1, 2 and 3 ksi prestress. Data taken on 4/14/05.

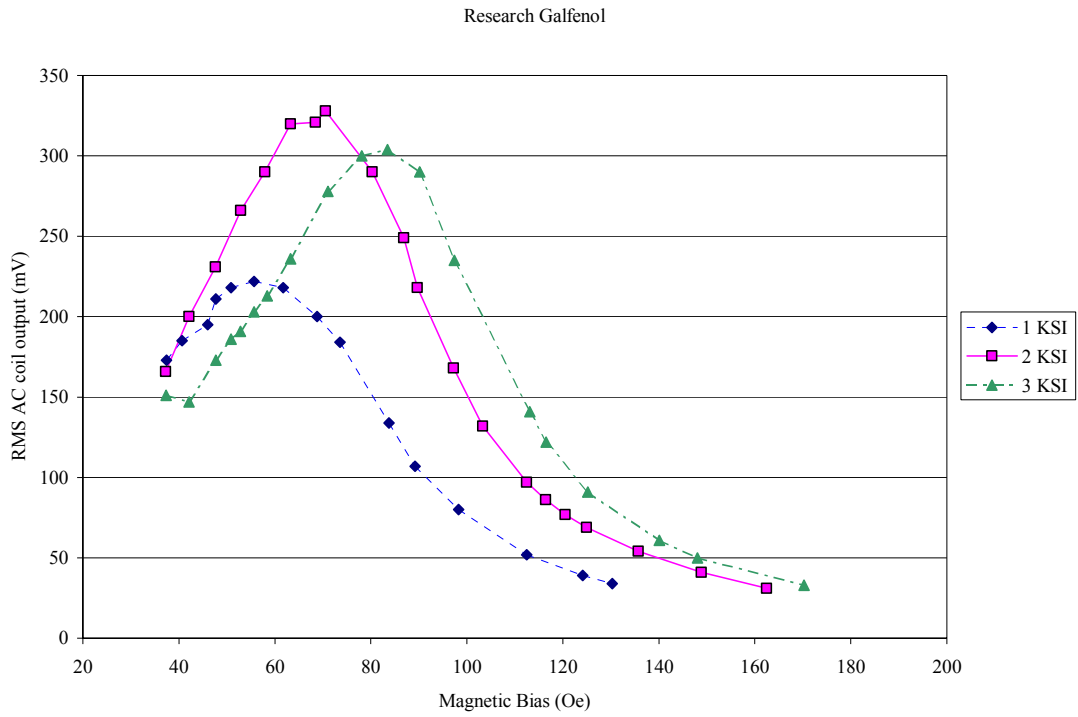


Figure 3.6: research Galfenol sweep tests at 1, 2 and 3 ksi prestress. Data from 4/13/05.

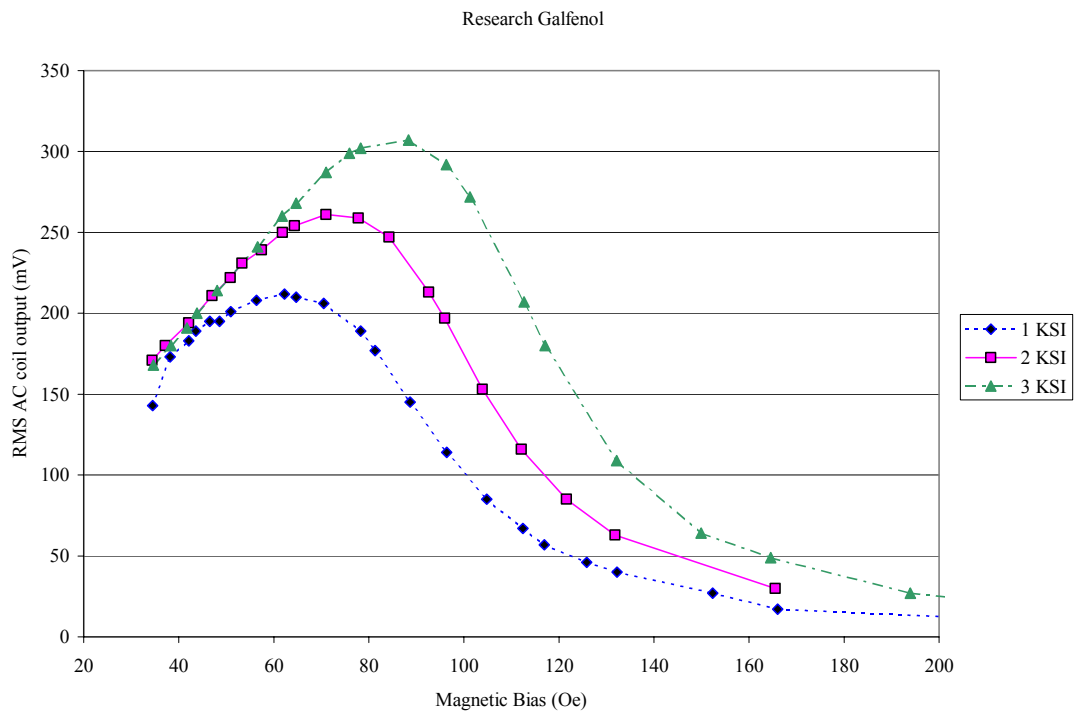


Figure 3.7: research Galfenol sweep tests at 1, 2 and 3 ksi prestress. Data on 4/14/05.

### **3.4 Sine sweep tests at 2 ksi and different biases**

Further sweep tests were performed at 2 ksi for both Terfenol-D and research Galfenol to reinforce the optimum bias results of the previous dwell tests. The data in Figs. 3.8 and 3.9 validates the dwell data because the optimum biases found from the dwell tests prove to be the same during these sweep tests. It is interesting to note that for the research Galfenol tests with a  $2\text{-lb}_f$  mechanical input, an extremely high bias is less favorable than no applied bias. The sense coil still registers output for no applied bias, but has zero electrical output for 300 Oe bias, which is above the saturation bias for Galfenol as shown in Fig. 3.1. In the case of the zero applied bias, there still is a residual magnetization of the rod. The bias tests for Terfenol-D have the same result where magnetic bias significantly affects the magnitude of output from the sense coil, with large biases appearing to limit dipole rotation for the mechanical input tested.

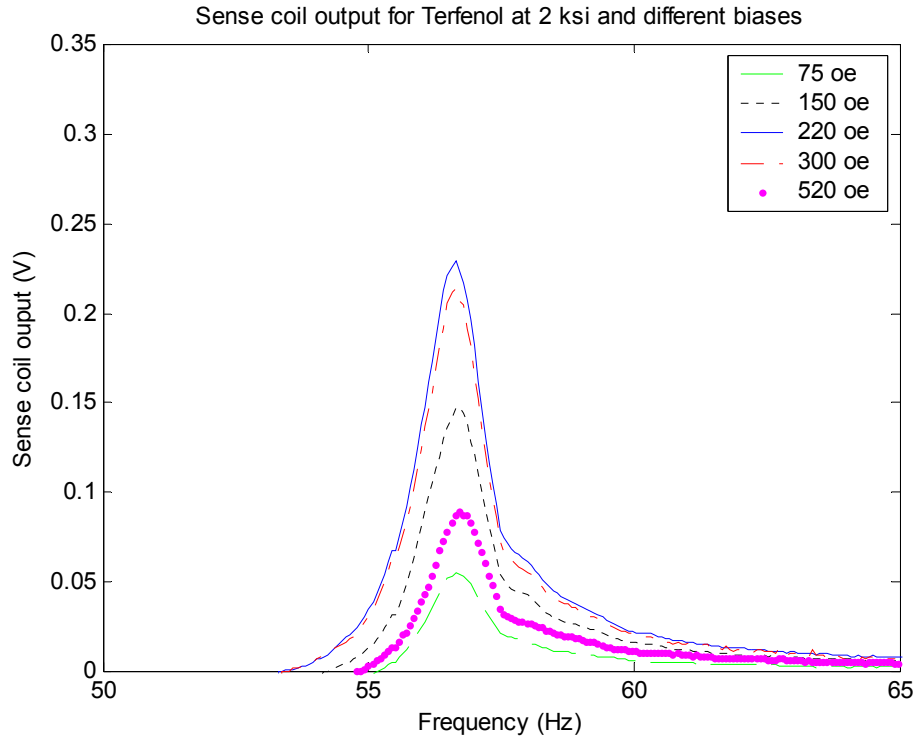


Figure 3.8: Sense coil output for Terfenol-D at 2 ksi prestress and varying biases.

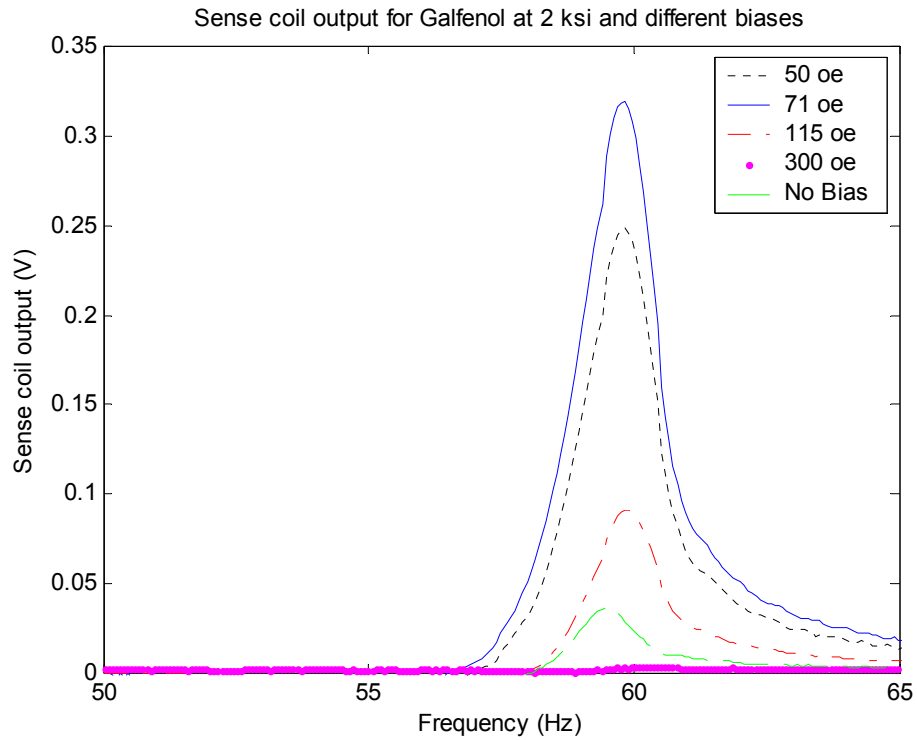


Figure 3.9: Sense coil output for research Galfenol at 2 ksi prestress and varying biases.

### 3.5 Sine Sweep Tests at different prestresses and optimum bias

To accurately evaluate whether different prestresses can have different outputs at their respective optimum bias, sweep tests were again run at different prestresses. In Figs. 3.10 and 3.11 it is easy to see that the prestress setting affects the natural frequency response of the transducer. This phenomena is related to the discussion in section 1.3.2.3, where the influence of magnetic field and flux density on the Young's modulus is examined.

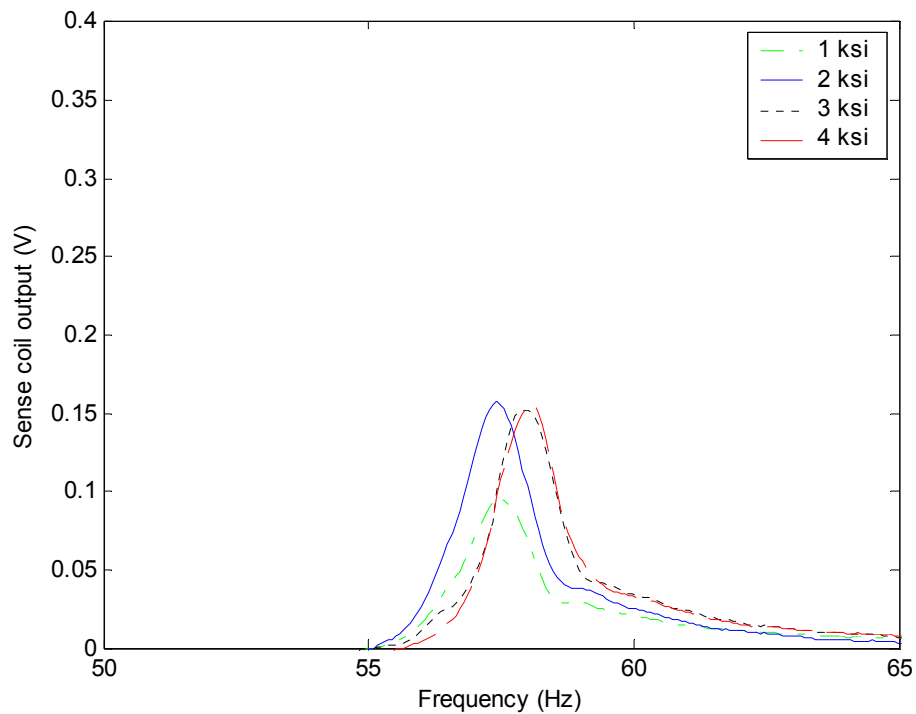


Figure 3.10: Sense coil open circuit output for Terfenol-D under different prestress and the corresponding optimum bias as determined from Figs. 3.4 and 3.5.

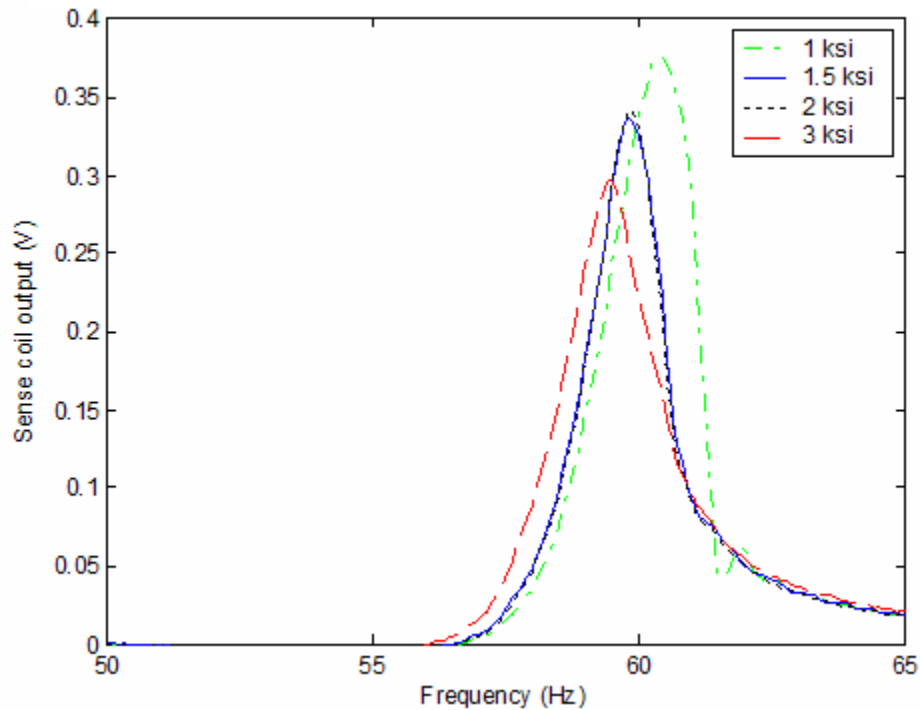


Figure 3.11: Sense coil open circuit output for research Galfenol under different prestresses and the corresponding optimum bias as determined from Figs. 3.6 and 3.7.

Table 3-1: Terfenol-D maximum sense coil output comparison

Prestress (ksi)	Fig 3.4 (mV output)	Fig 3.5 (mV output)	Fig 3.10 (mV output)
1	102	140	70
2	165	211	100
3	186	180	153

Table 3-2: research Galfenol maximum sense coil output comparison

Prestress (ksi)	Fig 3.6 (mV output)	Fig 3.7 (mV output)	Fig 3.11 (mV output)
1	222	212	340
2	328	261	330
3	304	307	220

For the Terfenol-D data in Table 3.1, the increasing output trend with prestress matches for the Figs. 3.4 and 3.10 data. The discrepancy in the data trend for Fig. 3.5 could be attributable to the resonant frequency shift due to changes in prestress. For the Galfenol sweep tests it is interesting to note that 3 ksi, which had the best performance for the dwell tests in Fig. 3.7, has the lowest performance for the sweep

test. 1 ksi and 2 ksi have similar performance for the sweep test in Fig. 3.11, but the sense coil open circuit output dropped significantly for 3 ksi of prestress. A possible explanation for this has not been identified.

### **3.6 Scalability of electrical output to mechanical input**

Sine sweep tests were run at 2 ksi and optimum bias for both Terfenol-D and research Galfenol to assess how the magnitude of electrical output is affected by the magnitude of mechanical input. Figures 3.12 and 3.13 show the results of sense coil output for mechanical input levels of 1 to 4 lb<sub>f</sub> peak input force to the system. A notable test phenomenon is the fact that as mechanical input to the transducer increases the natural frequency response decreases. This occurs for both Terfenol-D and Galfenol as shown in the sense coil response (Figs. 3.12 and 3.13) and the beam tip acceleration (Fig. 3.14, 3.15). Kellogg<sup>16</sup> noted similar trends during testing of a tunable Terfenol-D vibration absorber, where as the input vibration level increased the natural frequency of the transducer decreased. The result of dividing the sense coil data by the beam tip acceleration data is shown in Figs. 3.16 and 3.17 for both Terfenol-D and research Galfenol respectively. That the traces in Figs. 3.16 and 3.17 almost overlap indicates that as dynamic force input increases the sense coil output increases by the same percentage. This means that the response to force is linear and that at the tested input levels both of the magnetostrictive materials were not stressed to their saturation magnetostriction value.

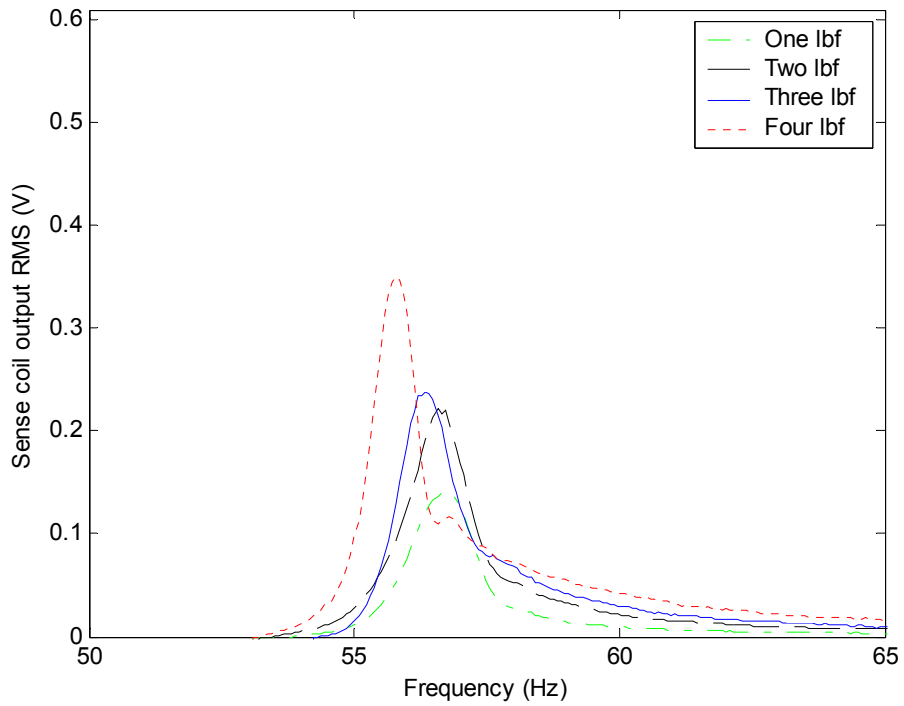


Figure 3.12: Sense coil output for Terfenol at 2 ksi and optimum bias (220 Oe) vs. frequency at input peak sine forces of 1,2,3 and 4 lb<sub>f</sub>.

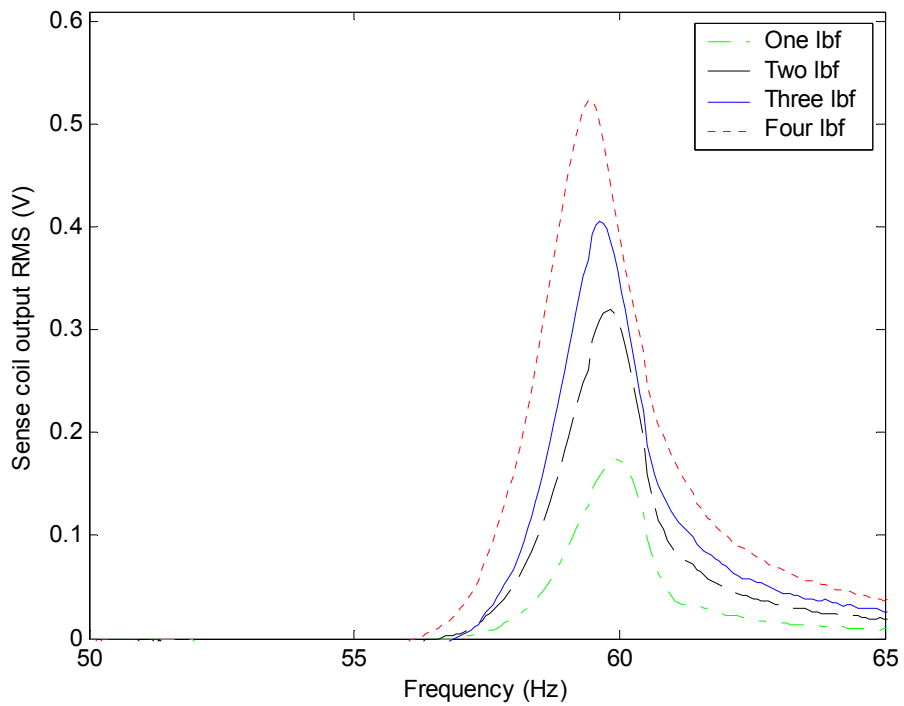


Figure 3.13: Sense coil output for research Galfenol at 2 ksi and optimum bias (71 Oe) vs. frequency at input peak sine forces of 1,2,3 and 4 lb<sub>f</sub>.

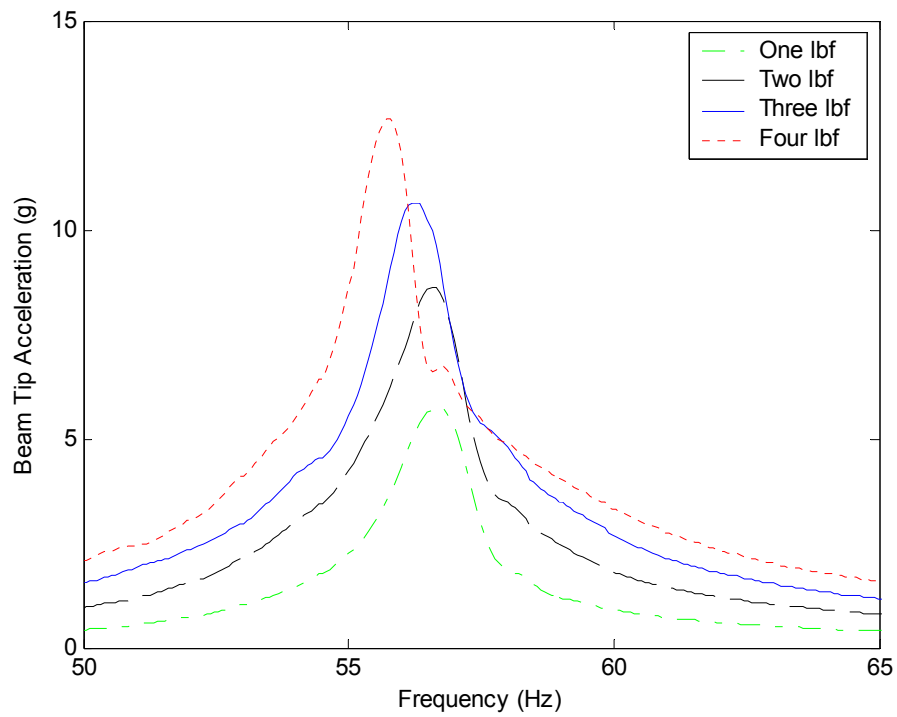


Figure 3.14: Beam tip acceleration response vs. frequency at input peak sine forces of 1,2,3 and 4  $lbf_f$  for Terfenol-D.

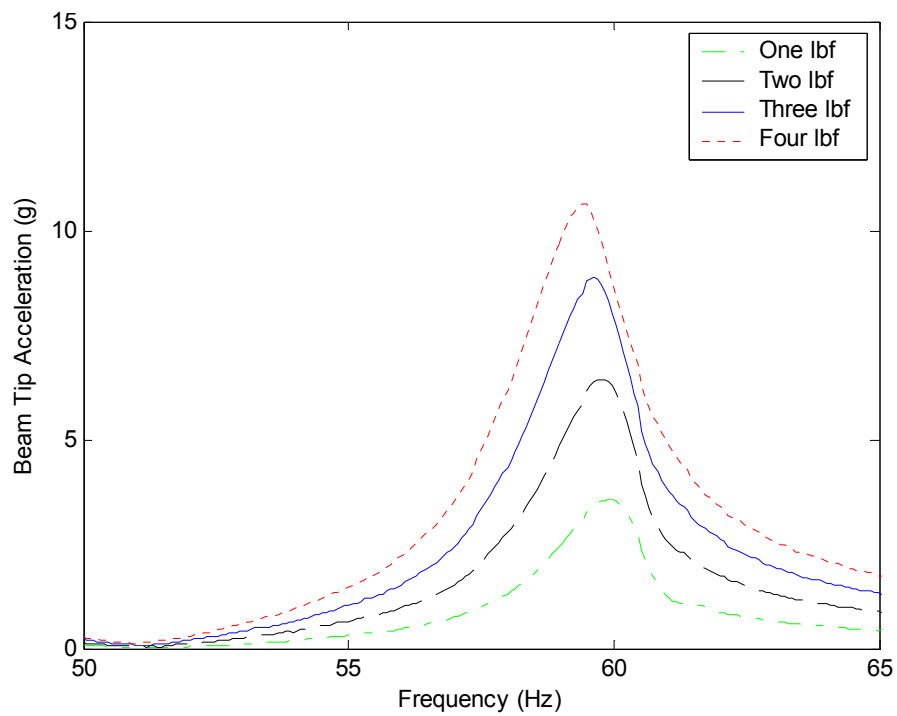


Figure 3.15: Beam tip acceleration response vs. frequency at input peak sine forces of 1,2,3 and 4  $lbf_f$  for research Galfenol.

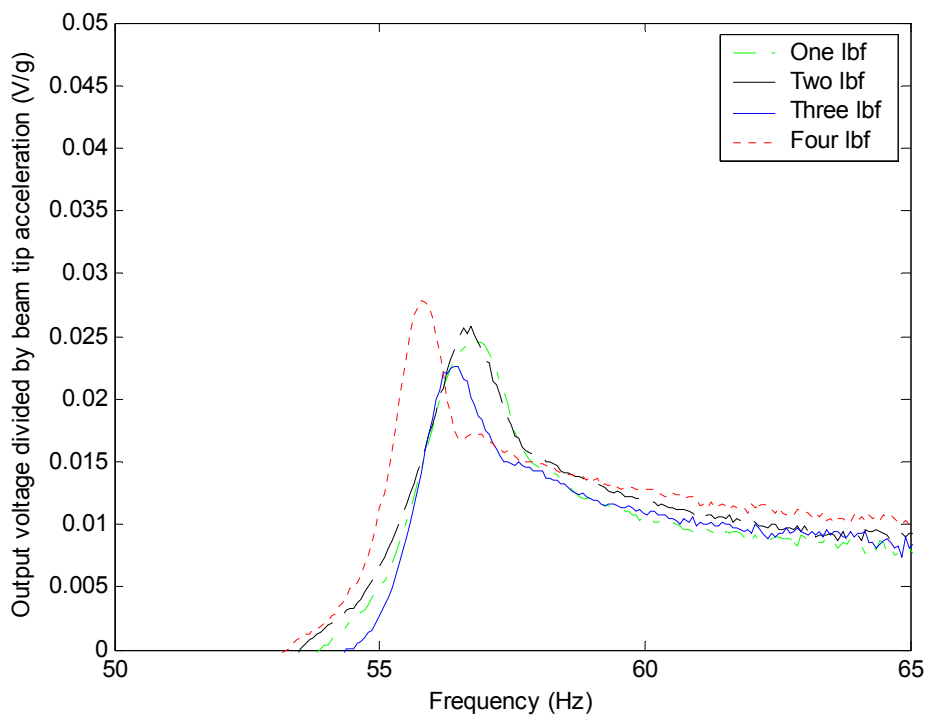


Figure 3.16: Sense coil output (Fig. 3.12) divided by beam tip acceleration (Fig. 3.14) for Terfenol-D.

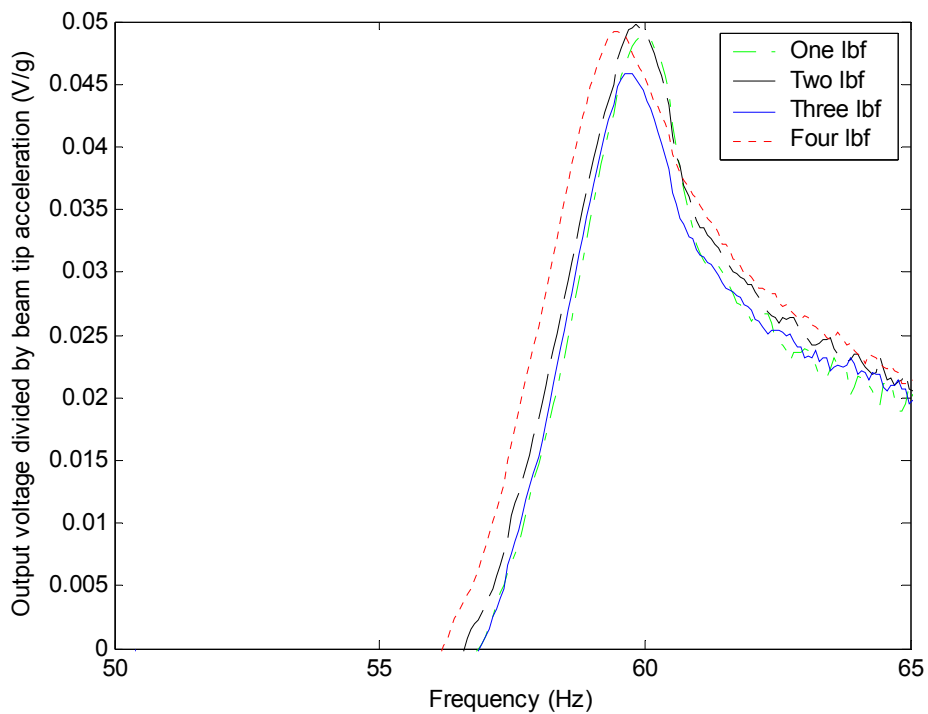


Figure 3.17: Sense coil output (Fig. 3.13) divided by beam tip acceleration (Fig. 3.15) for research Galfenol.

### 3.7 Circuit Tests

Full circuit tests were performed for all three rod materials under 2 ksi at the optimum bias for each material as determined from the open circuit testing. During this part of the testing the coil used for all previous tests, which was made of 38 gauge wire and had a 127 ohm resistance, broke. A new coil was made of 28 gauge wire, yielding fewer turns than the previous coil and a resistance of 20 ohms. Although inductance readings were not obtained from the original coil before it broke, data of load power was obtained for both coils, yielding more comparison data. Before the full circuit tests were performed, dwell test data similar to that presented in Section 3.3 was collected to verify the optimum bias for each prestress. The frequency used for these dwell tests was based on resonance under a 3 ksi prestress. This data is displayed in Appendix C. As the load resistance was changed using the resistor decade box, the associated change in voltage across the load resistor was recorded. Then the power delivered to the load resistor was calculated using Equation 2.6. Curves of electrical power delivered to the load resistor versus the load resistance value are displayed in Fig. 3.18 for Terfenol-D, research Galfenol, and production Galfenol.

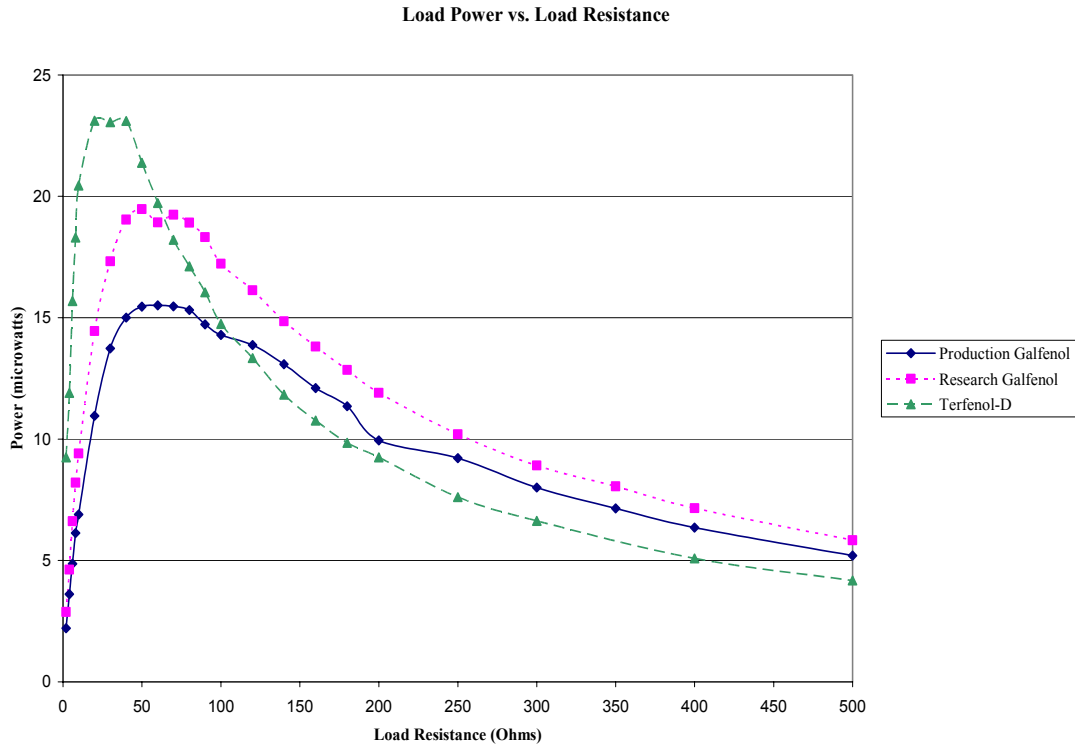


Figure 3.18: Power delivered to load vs. load resistance for production and research Galfenol and Terfenol-D under 2 ksi prestress and optimum bias for each material. This data was obtained with the 20 ohm coil and a 2-lb input sinusoidal force at the transducer resonant frequency of ~61 Hz.

The most significant discovery from the results in Fig. 3.18 is that solely considering open circuit voltage is not an accurate method of comparing materials for energy harvesting potential. The Galfenol rods consistently yielded higher open circuit voltages, but for the same mechanical input the Terfenol-D rod delivers larger output power to low values of resistive load. Also, the optimum load resistance is different for Terfenol-D and Galfenol as the core material. This difference in trends in trying to correlate output open circuit voltage to full circuit power and the difference in optimum load resistance with magnetostrictive core material is explained by the inductance of the transducer coil, which varies for the different magnetostrictive

materials because of the difference in their permeability. The value which the power curve graph approaches as the load resistance increases is related to the open circuit voltage because an open circuit measurement represents an infinite load resistance. As the load resistance increased the measured voltage drop approached the open circuit voltage measurement. Load power versus load resistance data for both the 20 ohm and the 127 ohm coils is shown for Terfenol-D and research Galfenol in Figs. 3.19 and 3.20 respectively. In both cases the 127 ohm coil yielded a higher maximum power delivered to the load and a higher optimum load resistance.

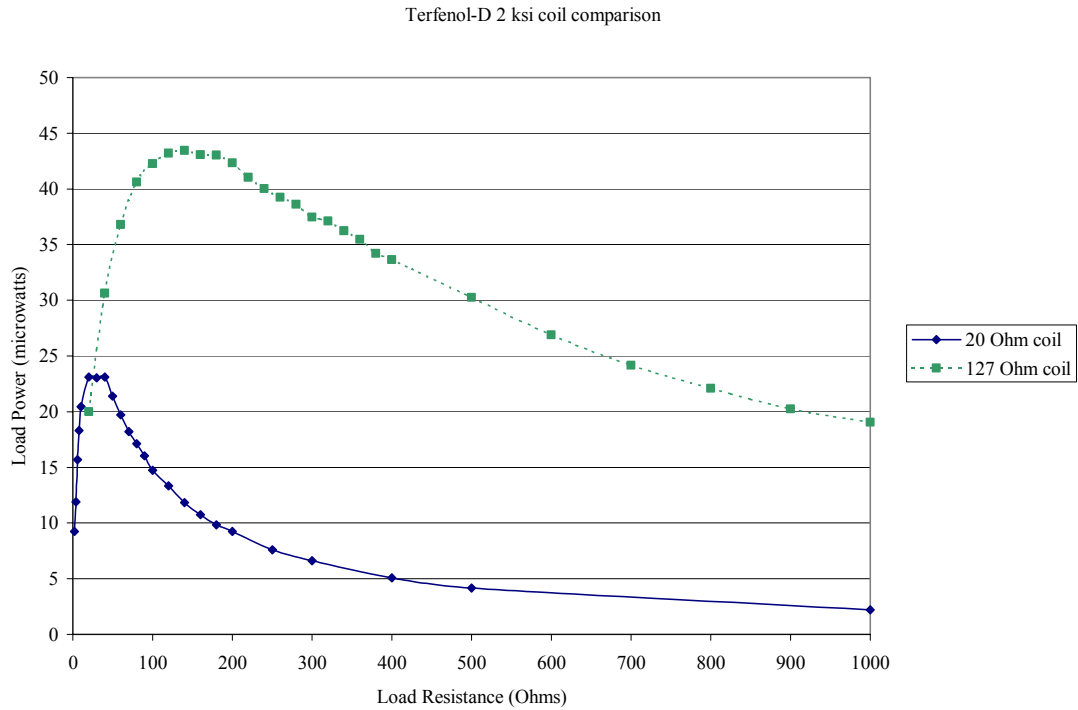


Figure 3.19: Comparison of power delivered to the load resistance for the two different coils tested. Material is Terfenol-D under 2 ksi prestress and a 2-lb input sinusoidal force at the transducer resonant frequency of ~61 Hz..

Research Galfenol 2 ksi coil comparison

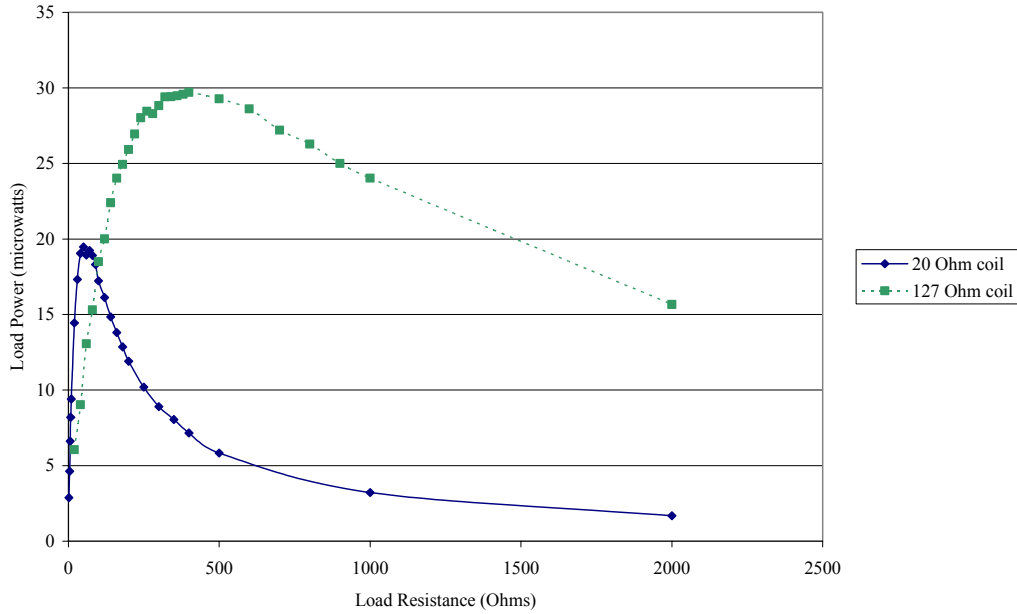


Figure 3.20: Comparison of power delivered to the load resistance for the two different coils tested. Material is research Galfenol under 2 ksi prestress and a 2-lb input sinusoidal force at the transducer resonant frequency of ~61 Hz..

Table 3-3: Optimum load resistance for maximum power transfer to load for the two different coils and two different materials.

	127 Ohm coil	20 Ohm coil
Terfenol-D	140 Ohms	20 Ohms
Research Galfenol	480 Ohms	50 Ohms

### 3.8 Coil Inductance

In preparation for analytically determining the optimum load resistance, the coil inductance value was recorded under different conditions for the 20 ohm coil. The coil inductance is affected by the permeability of each material which in turn is affected by changes in prestress and magnetic bias. The Extech LCR meter used (model: 380193) can obtain inductance readings at two test frequencies, 120 Hz and 1

kHz. Table 3.4 shows the values for air and the three magnetostrictive materials as the core material inside the 20 ohm coil at the two test frequencies. For these values no prestress or magnetic bias was applied. An expected but important result is the significantly higher inductance value for the coil when Galfenol is the core material. This is directly attributable to the higher permeability of Galfenol compared to Terfenol-D. An expected result was the large percentage change of the inductance reading between the two test frequencies for both types of Galfenol, while for air and Terfenol-D the inductance reading stayed fairly constant. This is attributable to eddy currents in the Galfenol rod and the fact that Galfenol has a lower eddy current cutoff frequency than Terfenol-D (Section 1.3.3.3).

Table 3-4: Coil Inductance readings at two test frequencies for 4 different coil core materials: Air, Terfenol-D, research Galfenol, production Galfenol. All readings taken under no prestress or bias.

	Air	Terfenol-D	Research Galfenol	Production Galfenol
120 Hz	11.49 mH	17.549 mH	97.2 mH	112.94 mH
1 kHz	11.369 mH	16.734 mH	57.52 mH	63.68 mH
Percent change	1 %	4.2 %	40.8 %	43.6 %

Table 3.5 displays inductance readings at the 120 Hz test frequency for 1, 2 and 3 ksi prestresses on the different magnetostrictive rod materials, while under no applied magnetic bias. The permeability decreases slightly with increasing prestress, but for the range of prestresses tested it is not a significant change.

Table 3-5: Coil inductance readings at 120 Hz for Terfenol-D, research Galfenol, and production Galfenol under 1, 2 and 3 ksi prestress, but no magnetic bias.

No Bias	Terfenol-D	Research Galfenol	Production Galfenol
1 KSI	20.7 mH	141.91 mH	170.78 mH
2 KSI	21.35 mH	141.35 mH	165.25 mH
3 KSI	20 mH	132.24 mH	162.2 mH

Table 3.6 displays inductance readings for the different magnetostrictive rod materials under no applied bias and the optimum applied bias as determined from the dwell tests. All readings were obtained for 2 ksi of prestress on the magnetostrictive rod. A significant result is the large percentage drop, averaging 50 percent, in the inductance reading of the coil for both Galfenol materials when the optimum magnetic bias is applied. This suggests a decrease in permeability at the optimal bias.

Table 3-6: Coil inductance readings at 120 Hz for Terfenol-D, research Galfenol, and production Galfenol under 2 ksi prestress for when no bias and optimum bias were applied.

	Terfenol-D	Research Galfenol	Production Galfenol
No Bias	21.35 mH	141.35 mH	165.25 mH
Optimum Bias	19.91 mH	74.32 mH	75 mH
Percent change	6.7 %	47.4 %	54.6 %

## 4. FULL CIRCUIT MODELING

### 4.1 Circuit Model

The goal of this section is to analytically model the behavior of the transducer electrical circuit (Fig. 2.7) and based on knowing just the coil resistance and inductance, predict the optimum load resistance. To determine the optimum load resistance, the power delivered to the load resistance must be maximized. The equation for the power delivered to the load resistance is shown in Equation 4.1.

$$P_{av} = \frac{\tilde{V}^2}{|Z_L|} \cos \theta \quad (4.1)$$

The average power delivered to the load resistance is the RMS voltage drop across the load resistor squared divided by the magnitude of the load impedance multiplied by the cosine of the impedance angle of the entire circuit. To find the impedance angle of the circuit, the overall circuit impedance must be reduced to the form shown in Equation 4.2.

$$Z = R + jX \quad (4.2)$$

For the circuit shown in Fig. 2.7, the overall impedance is determined from the load resistance,  $R_L$ , the coil resistance,  $R_C$ , and the coil inductance,  $L_C$  as given by Equation 4.3.

$$Z = (R_L + R_C) + j(\omega L_C) \quad (4.3)$$

The impedance angle,  $\theta$ , of the circuit is shown in Fig. 4.1 and the resulting cosine of the impedance angle is shown in Equation 4.4.

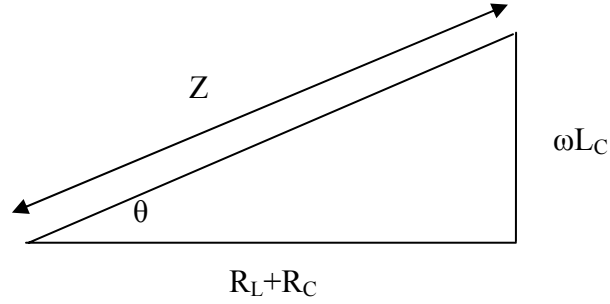


Figure 4.1: Impedance Triangle.

$$\cos \theta = \frac{R_C + R_L}{\sqrt{((R_C + R_L)^2 + (\omega L_C)^2)}} \quad (4.4)$$

The voltage across the load resistor,  $V_R$ , is determined by the ratio of the load impedance divided by the total circuit impedance multiplied by the RMS value of the source voltage,  $V_S$  (Equation 4.5).

$$\tilde{V}_L = \tilde{V}_S \left( \frac{R_L}{R_L + R_C + \omega L_C} \right) \quad (4.5)$$

Now Equations 4.4 and 4.5 can be combined with the magnitude of the load impedance to form the power flow equation through the load resistor, Equation 4.6.

$$P_{av} = \tilde{V}_S^2 \frac{\left( \frac{R_L}{R_L + R_C + \omega L_C} \right)^2}{R_L} \left( \frac{R_C + R_L}{\sqrt{((R_C + R_L)^2 + (\omega L_C)^2)}} \right) \quad (4.6)$$

Using the coil resistance value of 20 ohms and the coil inductance from Table 3.6 of 19.91 mH and 74.32 mH for Terfenol-D and research Galfenol respectively, Fig. 4.2 was generated using equation 4.6 while varying the load resistance value.

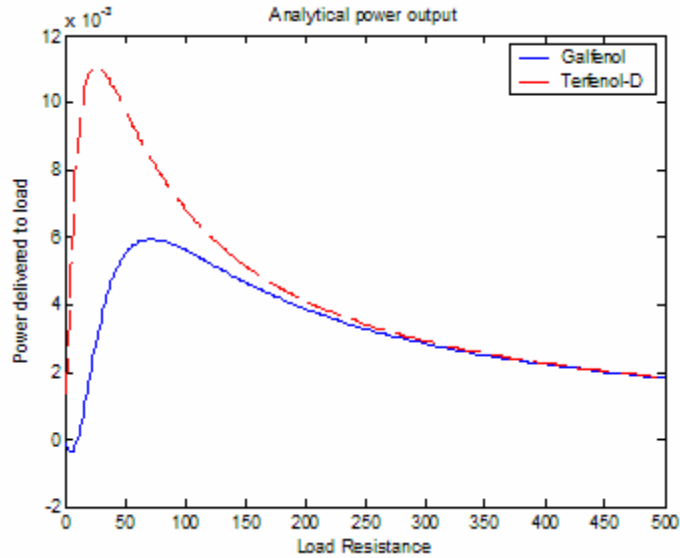


Figure 4.2: Power delivered to load resistance vs. the load resistance for Terfenol-D and research Galfenol. Generated using equation 4.6.

Two significant results are shown in Fig. 4.2. The first result is the accurate prediction of the optimum load resistance and the second is the match to the overall shape of the curves shown in Fig. 3.18 for the experimental results. The predicted and experimental optimum load resistances are shown in Table 4.1. The results are in very good agreement considering the resistance increment used during testing was 10 ohms.

Table 4-1: Experimental vs. analytical optimum load resistance values for Terfenol-D and research Galfenol in the 20 ohm coil.

	Terfenol-D	Research-Galfenol
Experimental Optimum Load Resistance (ohms)	20	50
Analytical Optimum Load Resistance (ohms)	22	43

A value of one volt was used for the source RMS voltage value to generate Fig. 4.2. However, even with the voltage source a constant value, the peak power magnitude,

though occurring at different resistances, is not the same for the two materials. The maximum power delivered to the load resistance for the coil with the Galfenol rod is almost half the maximum power for the coil with the Terfenol-D rod, even though the source voltages were assumed to have the same magnitude. This supports the experimental observation that the Terfenol-D rod yielded a higher magnitude power transfer to the load resistance, even though Galfenol rods developed a larger magnitude voltage output than the Terfenol-D rod in the open circuit tests. The coil inductance values are directly attributable for the phenomenon. This knowledge is critical in comparing the performance capability of each material.

#### **4.2 Transducer Efficiency**

An important consideration for any energy harvesting method is the conversion efficiency from its ambient energy source to electrical energy. Even though this study's main goal was to implement a working magnetostrictive transducer and compare performance for different magnetostrictive materials, prestresses, biases, and load resistances, the efficiency of this transducer is a good metric for future magnetostrictive energy harvesting work.

Since output performance was obtained for an input peak sine force of  $2 \text{ lb}_f$  (8.9N), the input power is calculated for the same value. The overall transducer mass is approximately 4 lbm (1.8 kg). By treating the energy harvester as a rigid body, a lumped mass approximation, the peak acceleration is calculated be  $5 \text{ m/s}^2$ . Since the

mechanical input is a sine wave of fixed frequency, the peak velocity of the entire transducer is easily determined.

$$a = a_{\max} \sin(\omega t) \quad (4.7)$$

The integral of Equation 4.7 provides the transducer velocity equation.

$$v = -v_{\max} \cos(\omega t) \quad (4.8)$$

From the integration  $v_{\max}$  equals the peak acceleration divided by the frequency in radians per second. The test frequency for the peak full circuit output occurred at 63 Hz (396 rad/sec), which yields a peak velocity of .0126 m/s. The peak kinetic energy of the systems is calculated using Equation 4.9.

$$KE_{\max} = \frac{1}{2}mv_{\max}^2 \quad (4.9)$$

Doing this calculation yields a  $KE_{\max}$  of  $143 \times 10^{-6}$  J, which corresponds directly to the work input to the transducer since the kinetic energy is a maximum when the potential energy is a minimum, zero. The RMS kinetic energy is then the maximum, divided by the square root of two, which yields a value of  $101 \times 10^{-6}$  J. Power is calculated by dividing the RMS kinetic energy by the time period, which is the inverse of the excitation frequency. This yields a time interval of  $1/63 \text{ Hz}^{-1}$  which equals .0158 seconds.

$$P_{\text{avg}} = \frac{KE_{\text{rms}}}{\Delta t} = \frac{101 * 10^{-6} J}{.0158s} = .00635 \text{Watts} \quad (4.10)$$

The peak power transferred to the load was 43.5 microwatts ( $\mu\text{W}$  - RMS) for Terfenol-D under 2 ksi and optimum bias using the 127 ohm sense coil and a load resistance of 140 ohms. The transducer efficiency is simply calculated in the following equation by dividing the electrical output power by the mechanical input power and multiplying by 100 to yield a percentage result.

$$\text{Efficiency} = \frac{.0000435}{.00635} * 100 = .69\% \quad (4.11)$$

This efficiency could be further improved by optimizing the sense coil, possibly implementing a complete high permeability magnetic flux path or by using a permanent magnet to produce the bias field and reducing the mass of the transducer.

The inclusion of a permanent magnet would prevent the DC bias coil from extracting energy from the sense coil, a drawback of the current setup in which placement of the sense coil inside the DC coil yields a transformer. The DC bias coil used in the current transducer was needed to allow variability of magnetic bias. Once the optimum bias for an operating condition had been identified it would have been useful to repeat tests using a permanent magnet. Unfortunately at the time of testing a magnet of the correct dimensions and bias could not be found. The power extracted from the DC coil was on the same order as that transferred to the load resistance, so removal of this coil could double the efficiency of the transducer. For practical applications, replacing the DC coil with a permanent magnet is mandatory because, even if using a permanent magnet instead of a DC coil to provide a magnetic bias to the magnetostrictive rod did not increase the power output of the transducer, the DC

coil requires power to operate. A DC bias coil would reduce or negate any power output harvested.

## 5. CONCLUSION

### 5.1 Summary of Results

The design of the resonant energy harvesting transducer was successful in practice, yielding a magnetostrictive energy harvester which does not affect the host structure's stiffness yet still converts ambient mechanical vibration into electrical energy. A trend of increasing optimum bias for increasing prestress was established and quantified for Terfenol-D, research Galfenol and production Galfenol. The dependence of the transducer resonant frequency on prestress inhibited conclusive results for performance comparisons at different prestresses at their respective optimum bias. Linearity in scaling of mechanical input to electrical output response functions indicates that for the input levels tested none of the magnetostrictive materials reached their saturation magnetostriction,  $\lambda_s$ .

Full circuit testing yielded the experimental optimum load resistance for each material and quantification of maximum power output for the sense coils tested. The full circuit tests also showed the relationship of peak power output to the coil inductance. This relationship yielded a lower full circuit power output for research Galfenol even though research Galfenol yielded a higher open circuit sense coil voltage than Terfenol-D. The 127 ohm coil, with ~3000 turns yielded significant gains over the 20 ohm sense coil, with ~1500 turns, suggesting that further improvements in the sense coil, and hence electrical output and transducer efficiency are possible. The electric circuit model was successful in predicting the optimum

load resistance based on the coil resistance and inductance values as well as the general shape of the load power versus load resistance curve. Also it matched the experimental result that research Galfenol yields a lower peak load power output than Terfenol-D because of the increased coil inductance, which is due to material permeability. For the circuit type used in this study, Terfenol-D performed the best, followed by research Galfenol and production Galfenol. For full circuit power output Terfenol-D produced an 18% performance gain over research Galfenol, and research Galfenol yielded a 25% performance gain over production Galfenol.

Efficiency calculation yielded a low conversion efficiency of mechanical power to electrical power, but areas that could yield significant improvement were identified.

## **5.2 Recommended Future Work**

Insights from the experimental results and circuit model have been used to identify areas of further study. First is an examination of sense coil performance through a model which takes into account the number of turns and the resistance. As coils increase in diameter, a single turn of wire requires a longer length, which will have a larger resistance and hence increased power loss. Therefore it is expected that there is a tradeoff between the number of turns, coil diameter, coil resistance, and coil inductance which will lead to an optimum coil design.

It might be possible to remove the detrimental effect of the coil inductance on the maximum power output by adding an appropriate capacitor in series with the coil and load resistance. The basis for this possibility is the fact that the reactance of a coil is negative as shown in Equation 5.1.

$$X_c = -j \frac{1}{\omega C} \quad (5.1)$$

The reactance of a coil is given in Equation 5.2 and if the reactance of the coil and the reactance of the capacitor are equal and opposite they will cancel.

$$X_L = j\omega L \quad (5.2)$$

$$X_L + X_c = 0 = j\omega L - j \frac{1}{\omega C} \quad (5.3)$$

Then, for a given inductance,  $L$ , and frequency,  $\omega$  the correct capacitance to use is determined by,

$$C = \frac{1}{\omega^2 L} \quad (5.4)$$

Canceling the reactance of the circuit would make the cosine of the impedance angle equal to one. Figure 5.1 shows how removing the circuit reactance would affect the peak load power. This figure was created using the data used to create Fig. 4.2. If possible to implement, this would yield a 13% performance improvement for the peak Terfenol-D power output and a 140% improvement for the peak Galfenol power output. Then given that the research Galfenol output has a higher open circuit voltage at the same prestress and input mechanical energy, this would make research Galfenol more efficient than Terfenol-D.

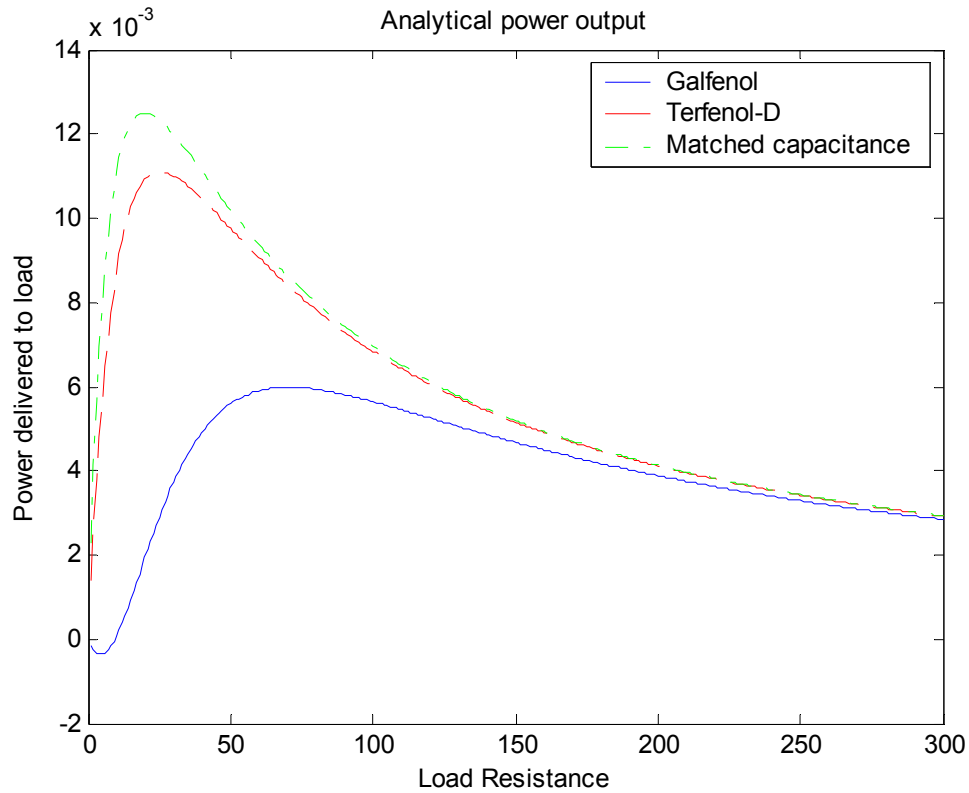


Figure 5.1: Power delivered to load resistance versus load resistance. Includes matched capacitance case. Assumes sense coil generates 1 volt in each case.

This thesis examined a magnetostrictive energy harvesting transducer which is resonant in nature and does not affect the stiffness characteristics of the host structure. A load bearing magnetostrictive transducer could take advantage of Galfenol’s high tensile strength and ductility which make it attractive for structural applications. If such a transducer was designed as an engine mount for a diesel engine on a ship, it would receive fairly constant frequency mechanical input and the high proof mass of the engine would ensure the magnetostrictive rod experiences large strain deformation which would increase the amount of flux generated. This type of

transducer would also be subjected to large dynamic loading at any frequency, eliminating the complicated resonant frequency optimization of the current energy harvesting transducer. Finally, an experimental implementation of a load bearing energy harvesting transducer would allow for easier experimental determination of performance versus prestress and optimum bias since the dynamic stress input is not dependant on a steep resonant frequency curve.

## APPENDIX A

Matlab code to determine the first beam natural frequency using the Hamiltonian/Rayleigh quotient method.

```
%energy harvesting - beam
%pinned at points A and B
%point B is the Terfenol Rod
%point A is a hinge at one end
%at the other end is an additional mass and tension spring.
clear all
close all

%integration to get deflection of beam
syms RA RB x p g A L1 L2 Ltot
m1 = -RA*x+p*g*A*(x*(x/2));
m2 = -RA*x-RB*(x-L1)+p*g*A*(x)*(x/2);
% from 0 to L1
yprime1 = INT(m1, x) % ,0, L1);
y1 = INT(yprime1, x) % ,0, L1);
% for L1<x<(L1+L2)
yprime2 = INT(m2, x, L1, x) % ,L1, Ltot);
y2 = INT(yprime2, x, L1, x) % ,L1, Ltot);

syms RA RB x p g A L1 L2 Ltot C11 C12 C21 C22 E I
%for section 1
Y11 = ((-1/6*RA*x^3+1/24*p*g*A*x^4)/(E*I)+C11*x+C12);
Y14 = DIFF(Y11, x, 4);
k14 = Y11; %p*g*A*
p14 = Y14;
%for section 2
Y21 = (1/24*p*g*A*(x^4-L1^4)+1/3*(-1/2*RA-1/2*RB)*(x^3-L1^3)+1/2*RB*L1*(x^2-L1^2)-
1/6*p*g*A*L1^3*(x-L1)-1/2*(-RA-RB)*L1^2*(x-L1)-RB*L1^2*(x-L1))/(E*I)...
+C21*(x)+C22;
Y24 = DIFF(Y21, x, 4);
k24 = Y21;
p24 = Y24;
KE1sym = INT(k14, x, 0, L1);
PE1sym = INT(p14, x, 0, L1);
KE2sym = INT(k24, x, L1, Ltot);
PE2sym = INT(p24, x, L1, Ltot);

%-----
%all numbers given in english units and converted to metric
%Beam Properties (Aluminum) METRIC meters, N, kg
L1 = 3*.02540 ;%m
L2 = 8*.02540 ;%m
w = .5*.02540;%m
h = .25*.02540 ;%m
A = w*h;% cross sectional area of the beam (m^2)
p = (0.0975*.4535924)/(.02540^3) ;% density of beam material kg/m^3
```

$E = (10 \times 10^6 \times 4.4482216) / (.02540^2);$  % beam youngs modulus N/m<sup>2</sup>

$\text{weightofbeamkg} = A \times (L1 + L2) \times p$

if  $w == h$

    % square beam

$I = w^4 / 12$

else

    % rectangular beam

$I = (w \times h^3) / 12$

end

$M = .3 \times 0.4536;$  % mass at the end of the beam kg

$K = (16 \times 5 \times 4.4482216) / .02540;$  % spring constant (N/m)

$\text{delta} = .5 \times .02540;$  % amount spring is pulled down (m)

$g = 9.8;$  % kg to N

%-----

% %-----

% %Beam Properties (Aluminum)

%  $L1 = 3;$  %inches

%  $L2 = 5;$  %inches

%  $w = .75;$  %inches

%  $h = .5;$  %inches

%  $A = w \times h;$  % cross sectional area of the beam (in<sup>2</sup>)

%  $p = 0.0975;$  % density of beam material lbf/in<sup>3</sup>

%  $E = 10 \times 10^6;$  % beam youngs modulus lbf/in<sup>2</sup>

%

%  $\text{weightofbeam} = A \times (L1 + L2) \times p$

%

% if  $w == h$

%   % square beam

%    $I = w^4 / 12$

% else

%   % rectangular beam

%    $I = (w \times h^3) / 12$

% end

%

%  $M = .3;$  % mass at the end of the beam lbf

%  $K = 240;$  % spring constant (lbf/in)

%  $\text{delta} = .5;$  % amount spring is pulled down (in)

%  $g = 1;$  % 1 lbm = 1 lbf

% %-----

%force at the end of the beam

$F_{\text{end}} = M \times g + K \times \text{delta}$  % lbf

%cross-sectional area of the terfenol rod

$\text{TerfA} = ((.25^2 \times \pi) / 4) \times (.02540^2);$

% static reaction at point B (terfenol rod)PRESTRESS LOAD

$\text{RB} = F_{\text{end}} \times ((L1 + L2) / L1) + p \times g \times A \times ((L1 + L2) / L1) \times ((L1 + L2) / 2);$

$F_{\text{terf}} = \text{RB};$

$\text{TerfprestressMPa} = \text{RB} / (\text{TerfA} \times 10^6)$  %Mpa

$\text{TerfprestressKSi} = \text{TerfprestressMPa} / 6.8947573$  %ksi

% static reaction at point A (hinge)

$\text{RA} = -F_{\text{end}} \times (L2 / L1) - p \times g \times A \times (L2 / L1) \times (L2 / 2) + p \times g \times A \times (L1 / 2);$

%below is a sum of forces - statically should be zero.

```

Check = RA+RB-Fend-p*g*A*(L2+L1)

y1 = subs(y1);
yprime1 = subs(yprime1);
y2 = subs(y2);
yprime2 = subs(yprime2);

%----Moment equations for the length of the beam-----
x = L1;
y1L = subs(y1);
y2L = subs(y2);
y1primeL = subs(yprime1);
y2primeL = subs(yprime2);
%for 0<x<L1
for i1=0:L1*10000
    x=i1/10000;
    a(i1+1)=i1/10000;
    M1(i1+1)= -RA*x+p*g*A*(x*(x/2));
end

% for L1<x<(L1+L2)
Ltot = L2+L1;
c = Ltot*10000;
n = L1*10000;
n=round(n);
c=round(c);
for i=n:c
    x=i/10000;
    b(i+1-n)=x;
    M2(i+1-n) = -RA*x-RB*(x-L1)+p*g*A*(x)*(x/2);
end

% Beam Moment Diagram
plot(a, M1)
hold on
plot(b, M2, 'r')

%simply supported yprime (x=0) not = 0!
C11 = -y1L/(L1*E*I);
C12=0;
for i1=0:L1*10000
    x=i1/10000;
    Yprime1(i1+1) = (-1/2*RA*x^2+1/6*p*g*A*x^3)/(E*I)+C11;
    YF1(i1+1)= (-1/6*RA*x^3+1/24*p*g*A*x^4)/(E*I)+C11*x+C12;
end

Ltot = L2+L1;
c = Ltot*10000;
n = L1*10000;
c=round(c);
n=round(n);
C21 = y1primeL/(E*I)+C11-y2primeL/(E*I);
C22 = -y2L/(E*I)-C21*L1;
for i=n:c
    x=i/10000;
    Yprime2(i+1-n)=(1/6*p*g*A*(x^3-L1^3)+1/2*(-RA-RB)*(x^2-L1^2)+RB*L1*(x-L1))/(E*I)+C21;

```

```

    YF2(i+1-n)=(1/24*p*g*A*(x^4-L1^4)+1/3*(-1/2*RA-1/2*RB)*(x^3-L1^3)+1/2*RB*L1*(x^2-
L1^2)-1/6*p*g*A*L1^3*(x-L1)-1/2*(-RA-RB)*L1^2*(x-L1)-RB*L1^2*(x-L1))/(E*I)...
    +C21*(x)+C22;

```

```
end
```

```

figure(2)
plot(a, YF1)
hold on
plot(b, YF2, 'r')
title('Beam deflection (in)')
xlabel('distance along beam length (in)')
ylabel('deflection(in)')
figure(3)
plot(a, Yprime1)
hold on
plot(b, Yprime2, 'r')
title('Beam slope')
xlabel('distance along beam length (in)')

```

```

x=1
check1K =subs(k14)
check1P =subs(p14)
check1sum =check1P+check1K
x=4
check2K =subs(k24)
check2P =subs(p24)
check2sum =check2P+check2K
x=7
check3K =subs(k24)
check3P =subs(p24)
check3sum =check3P+check3K

```

```
%KE = kinetic energy PE = potential energy.
```

```

KEB1 = subs(KE1sym)
PEB1 = subs(PE1sym)
KEB2 = subs(KE2sym)
PEB2 = subs(PE2sym)

```

```

%deflection at the end of the beam times K
KE = K*YF2(i+1-n)

```

```

%deflection at the end of the beam times M
ME = M*YF2(i+1-n)

```

```

%apply Hamiltonian / rayleigh quotient
w2 = (KE+PEB1+PEB2)/(ME+KEB1+KEB2);

```

```

%convert from radians to hz
w = (w2^(.5))/(2*pi)

```

## APPENDIX B

$\lambda$ -H curves for Terfenol-D and research Galfenol at different prestresses. Some of the hysteresis present in all curves is due to the drift inherent in the DVRT.

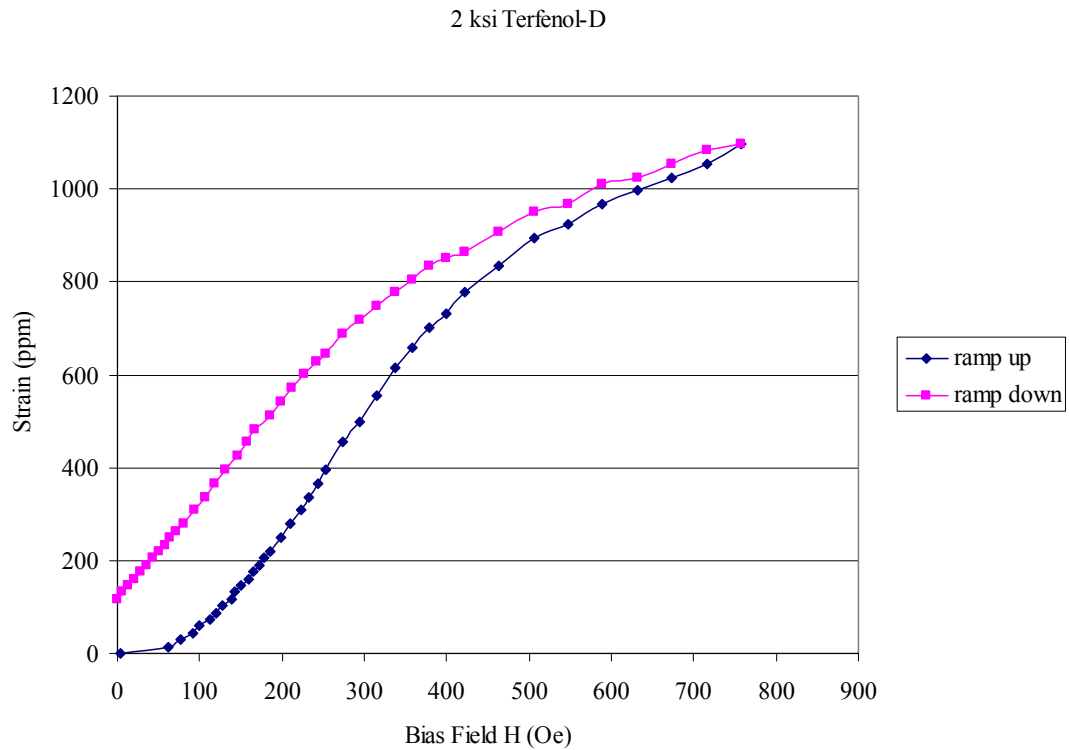


Figure B-1: Terfenol-D  $\lambda$ -H curve at 2 ksi prestress

### 3.9 ksi Terfenol

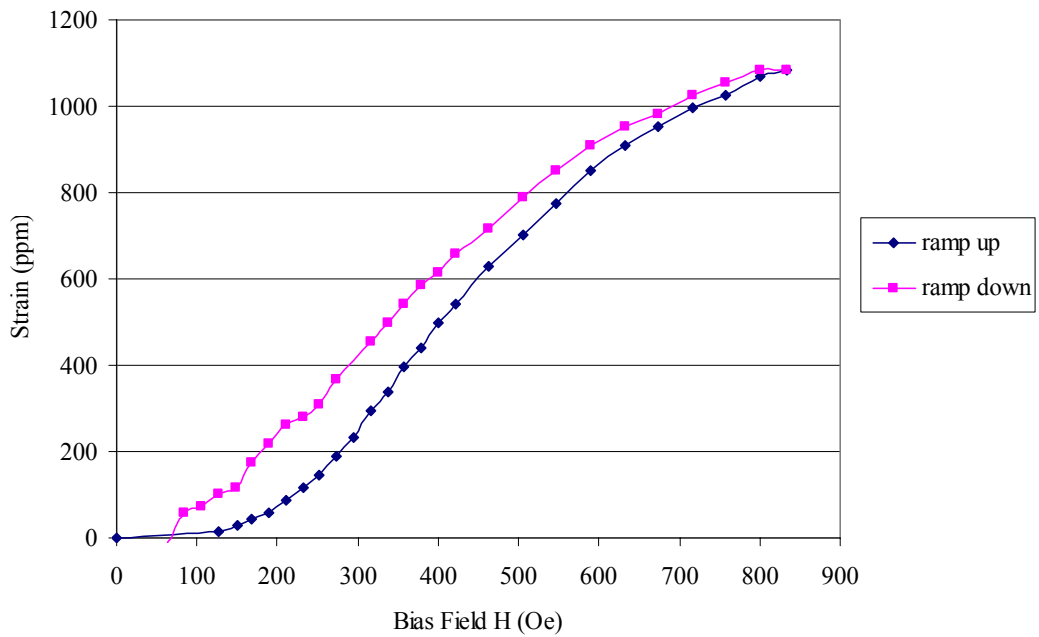


Figure B-2: Terfenol-D  $\lambda$ -H curve at 3.9 ksi prestress.

### 1.1 ksi Research Galfenol

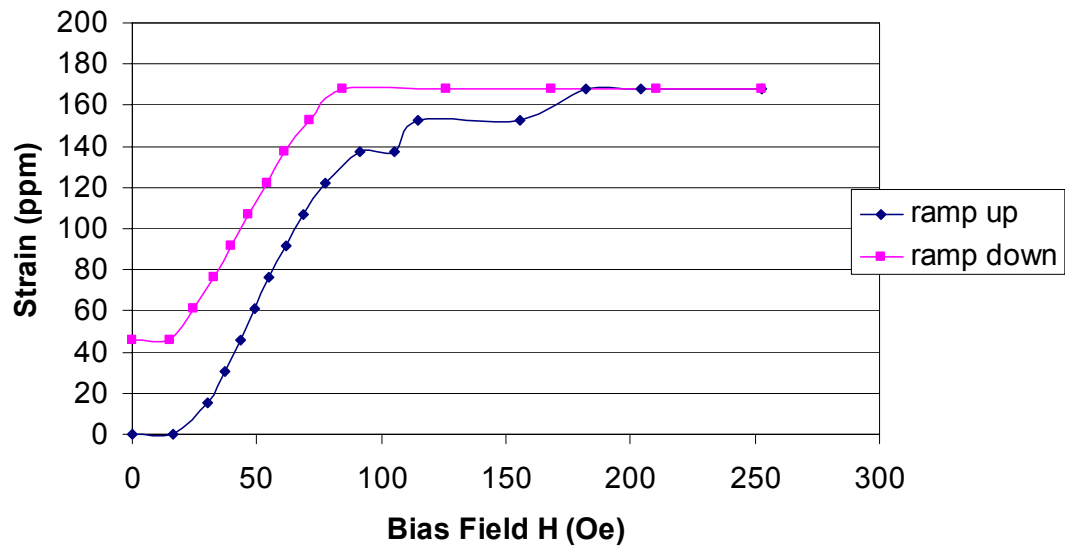


Figure B-3: Research Galfenol  $\lambda$ -H curve at 1.1 ksi prestress.

### 2 ksi Research Galfenol

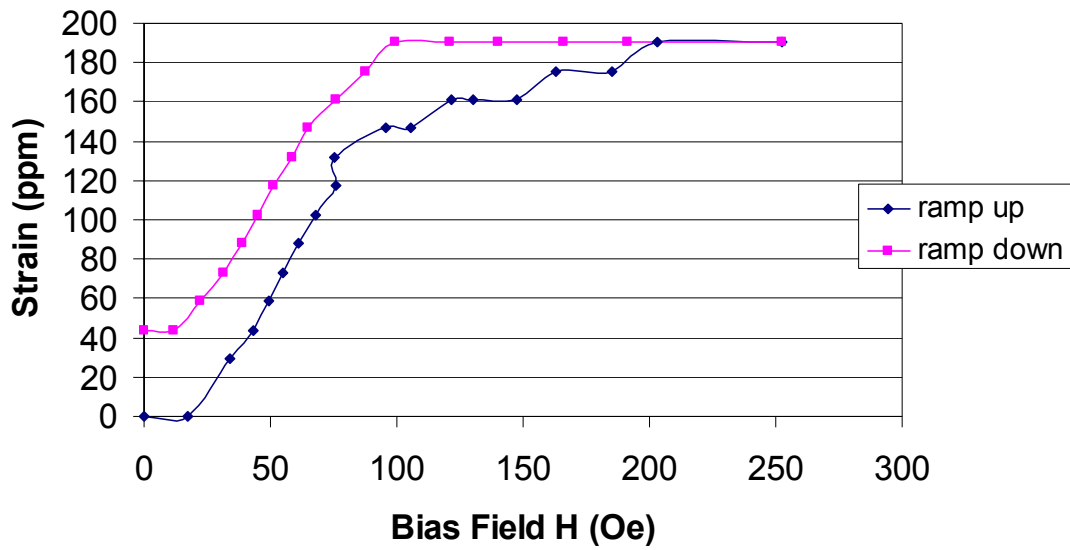


Figure B-4: Research Galfenol  $\lambda$ -H curve at 2 ksi prestress.

### 3 ksi Research Galfenol

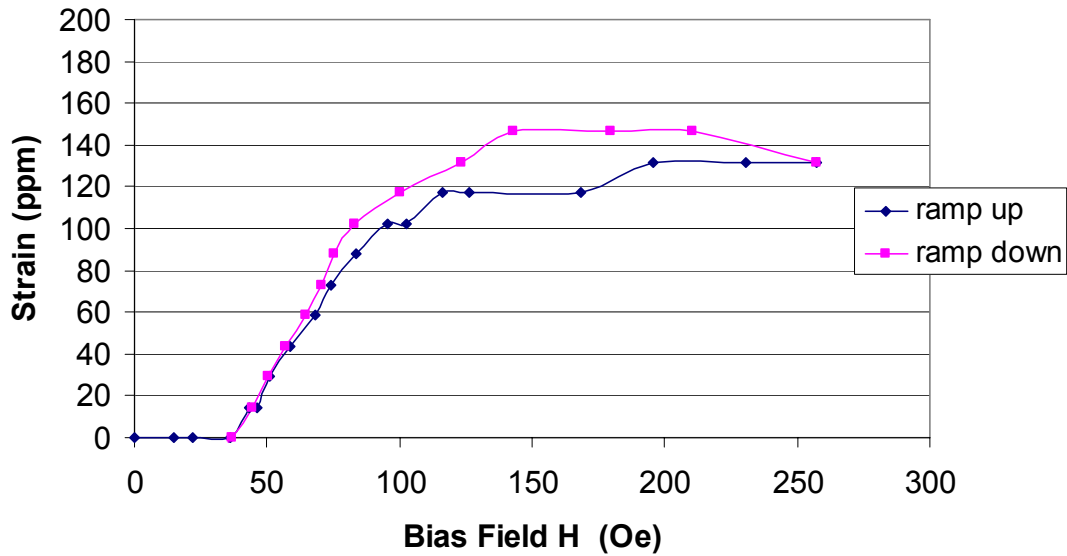


Figure B-5: Research Galfenol  $\lambda$ -H curve at 3 ksi prestress.

# APPENDIX C

Dwell tests for Terfenol-D, Research Galfenol, and Production Galfenol using the 20 ohm, 28 gauge wire sense coil. Note the significant hysteresis present in the Terfenol-D data as the bias is continuously swept up and down.

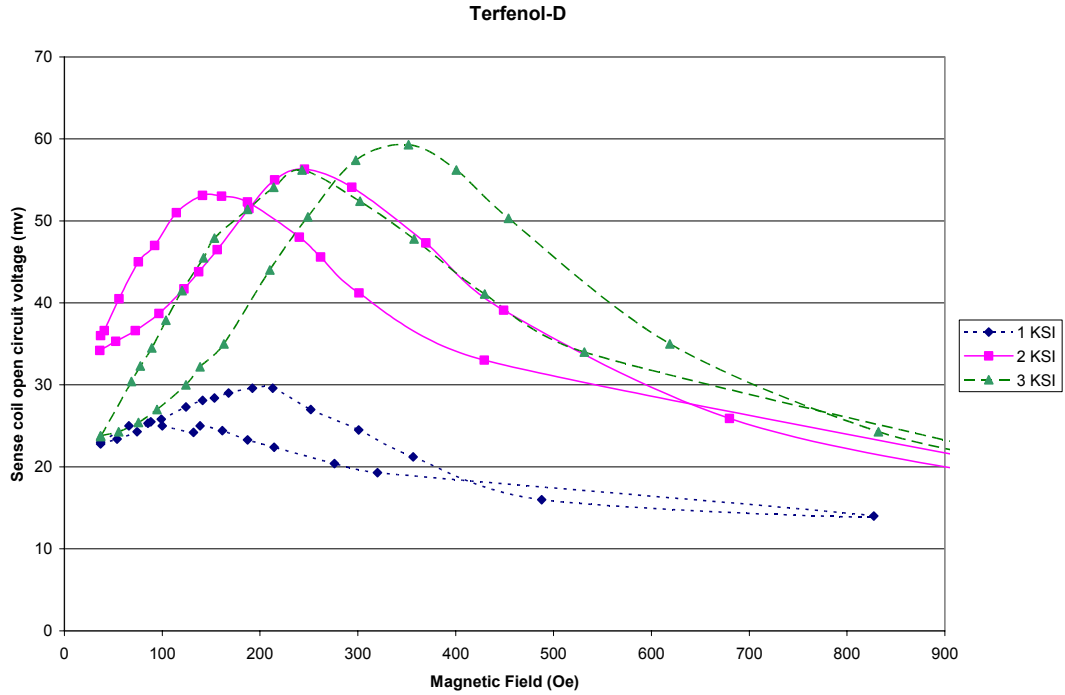


Figure C-1: Terfenol-D sense coil performance at 60 Hz for various biases and prestresses, which displays significant hysteresis. 20 ohm sense coil.

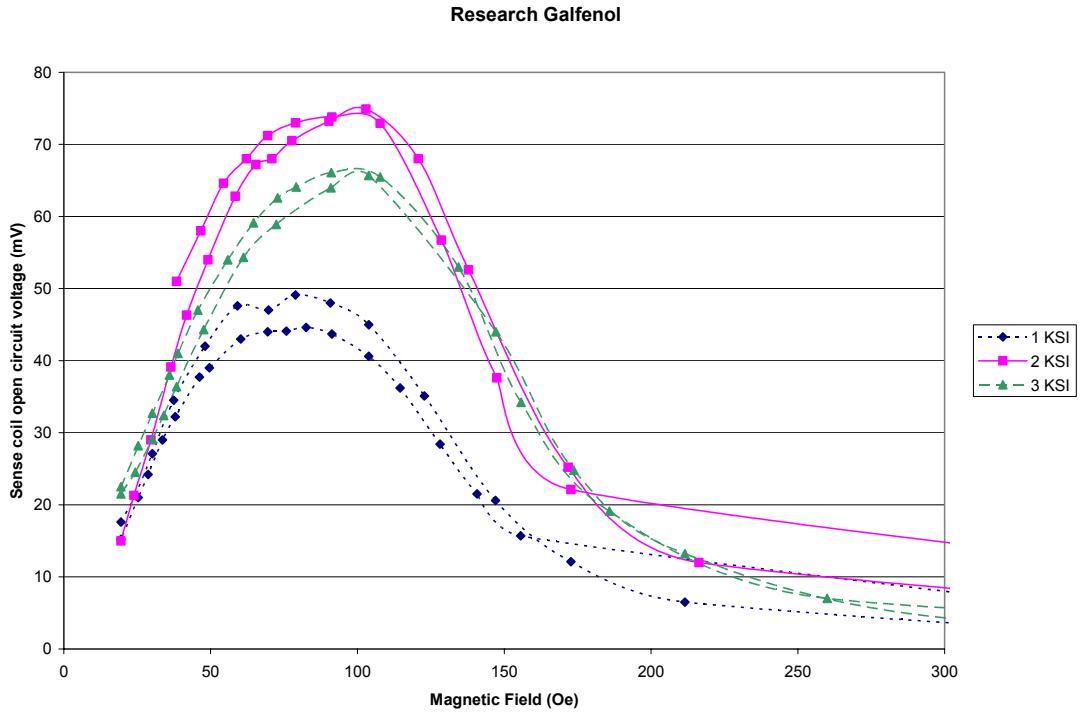


Figure C-2: Research Galfenol sense coil performance at 58.9 Hz for various biases and prestresses. 20 ohm sense coil.

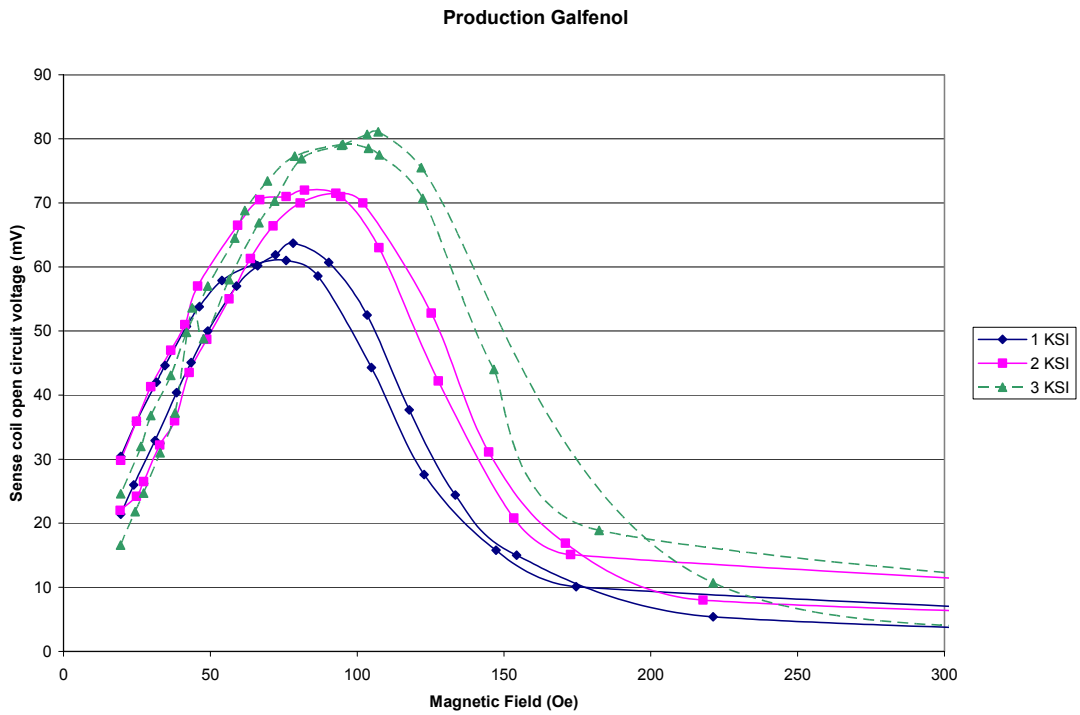


Figure C-3: Production Galfenol sense coil performance at 58.9 Hz for various biases and prestresses. 20 ohm sense coil.

## APPENDIX D

Magnetostrictive rod data

	Rod ID #	Length (in)	Diameter (in)	Weight (oz)
Terfenol-D	F1-99-172-01	2.019	.249	.526 oz
Research Galfenol	F1-03-144-100	2.001	.249	.449 oz
Production Galfenol	F1-03-112-190	2.002	.249	.451 oz

## **APPENDIX E**

MMM paper on Terfenol-D based toothphone experimental sensor operation.

### **Terfenol-D Tooth Phone Performance Characterization and Optimization**

Mark E. Staley, Alison B. Flatau

Aerospace Engineering Department, University of Maryland, MD 20742

A new Terfenol-D transducer has been developed for use as a tooth phone with both sensing and actuating capabilities by Audiodontics Inc. This research focuses on characterizing the sensitivity of the tooth phone's magnetostrictive Terfenol-D rod performance in both sensor and actuator mode to changes in the initial prestress of the device. A new test apparatus was designed to allow prestress variability using a micrometer head and a static load cell while operating the transducer as either a sensor or an actuator. To assess sensor-mode performance, a force-feedback loop control system was used to excite the tooth phone with a constant force from a mechanical shaker at the tooth-tooth phone interface surface while measuring the voltage generated in the transducer's coil. The shaker was driven with a 200 Hz to 7 kHz swept sine at dynamic force loadings of .0005, .001, .01, .02 and .03 pounds of force for prestresses ranging from .25 to 3.5 ksi. Results indicate a prestress of 2 ksi offers the best sensor-mode performance.

To assess actuator performance, a miniature accelerometer was attached to the tooth-tooth phone interface surface and output acceleration was recorded while sweeping the tooth phone excitation frequency from 200 Hz to 7 kHz with zero-to-peak voltages of .1, .3 and .5 V. The prestress settings were varied from .3 to 3.25 ksi. As an actuator, no prestress offered a significant broadband performance advantage. Finally, comparisons were made of the tooth phone and an accelerometer for measuring tooth vibrations induced during humming. They perform similarly and capture much of the frequency content found in concurrently recorded microphone data.

## I. INTRODUCTION

This research was undertaken to investigate the sensitivity of a Terfenol-D transducer to prestress application for both actuation and sensing modes. Previous studies have shown a strong dependence of the resonant response of Terfenol-D transducers to prestress [1]. However this transducer targets achieving a constant broadband performance rather than maximizing its resonant response, and the device under study is much smaller in size than previous Terfenol-D devices to allow its use as a tooth phone. The Terfenol-D rod employed in this transducer is  $.045 \pm .001$ " square and  $.3 \pm .002$ " long. It is surrounded by a  $\sim 1500$ -turn coil of 44-gauge shielded wire. The coil, in turn, is surrounded by a circular slit permanent magnet which provides a magnetic field bias. It is then packaged in a medical plastic housing with a tip which contacts a tooth. The fixed magnetic bias provided by the permanent magnet eliminates coupled optimization of pre-stress and bias, but still allows for prestress optimization at that bias.

The commercially available Terfenol-D rod used is an alloy of iron, terbium and dysprosium. Terfenol-D is capable of 1000 times more magnetic induced strain than iron [2]. This high strain ability is also possible at high frequencies making this material ideal for transducers. The linearized, one-dimensional coupled strain and magnetic flux equations are presented below.

$$B = d^* \sigma + \mu^* H \quad (1)$$

$$\varepsilon = \frac{\sigma}{E_y^H} + dH \quad (2)$$

All terms are explained in detail in [2]. Equations (1) and (2) can be used to predict the tooth phone performance as a sensor and actuator, respectively.

## **II. EXPERIMENTAL METHOD**

A test stand was designed to allow operation of the transducer in both actuation and sensing modes while varying the prestress on the Terfenol-D rod. The stand employs aluminum construction for its non magnetic properties to ensure no interference with the magnetic field path of the transducer. The setup is aligned vertically with the top beam of the setup the stiffest component to ensure no mechanical resonances in the test frequency range (selected to match predominant speech bandwidth). Stiffness and resonant frequencies for various cross-sections [3] were compared while keeping cross-sectional area constant. A channel design was chosen for its high stiffness and because it allowed easy attachment of the micrometer head into the channel. Directly underneath the micrometer is a Sensotec model 31 10-lb force static load cell which, combined with the known cross-section area of the Terfenol-D rod, allows for precise prestress application. The load from the micrometer is passed through the load cell to a small ceramic ball bearing, for load alignment, which sits in a spherical seat in the transducer stainless steel end cap. A center tip on the other side of the steel cap then pushes directly on the Terfenol-D rod. The transducer is clamped on its outer circumference to a mount which attaches back to the test stand. This allows for vibration of the plastic tip and Terfenol-D rod, but no free body movement of the transducer housing or prestress mechanism.

For sensor operation a 4-lb force Ling Dynamics shaker model V-203 is employed in conjunction with a PCB dynamic load cell to provide mechanical actuation of the transducer tip from 200 Hz to 7 kHz. The dynamic load cell along with a Signal Star Vector shaker controller allows for force feedback control of the shaker to ensure a constant peak sine force application to the transducer over the entire tested frequency range. Prestresses of .25 ksi to 3.25 ksi in .25 ksi increments were tested. Excitations included .0005, .001, .01, .02 and .03 pound force. The output used for sensor performance comparison is the induced voltage from the coil surrounding the Terfenol-D rod, which is proportional to the magnetic induction,  $B$ , in Eqn. (1).

In actuator operation mode, a .03 oz PCB accelerometer model 352A24 is attached to the tip of the transducer in place of the shaker and dynamic load cell. The transducer is actuated by passing a fixed voltage through the coil while sweeping in frequency from 200 Hz to 7 kHz. The transducer was operated at peak AC voltage levels of .1, .3, and .5 volts and results from nine prestress levels from .3 ksi to 3.1 ksi were recorded. The output used for actuator performance comparison is the tip acceleration, which is proportional the strain,  $\varepsilon$ , in Eqn. (2).

Finalizing the test procedure included assessing impact of sweep rate. Tests were conducted at sweep rates of 15 Hz/sec to 130 Hz/sec at 15 Hz/sec intervals at a fixed prestress without impacting sensor or actuator performance, indicating insensitivity to sweep rate. Early prestress performance tests prompted some changes including a newer back cap with a longer tip to ensure that the cap did not press against the coil at the

higher prestresses, which would prevent the entire load from being passed through the Terfenol-D rod.

## **II. SENSOR TEST RESULTS**

Results shown in Fig. 1 for .001 lbf excitation are typical induced voltage autospectra results. Figure 2 shows the area under the Fig. 1 autospectra (i.e. volts squared times frequency) for the different prestress settings. A prestress of 2 ksi yields the greatest broadband performance output. While Calkins [3] observed the minimum prestress that fixed the Terfenol-D rod in the transducer produces the largest resonant performance, Figs 1 and 2 are in keeping with results [4] indicating a maximum slope in magnetization versus stress data at ~2 ksi for 10-30 kA/m DC magnetic biases.

## **III. ACTUATOR TEST RESULTS**

Acceleration autospectra for the 0.5V excitation case are shown in Fig. 3. For the .3V and .5V tests, no prestress yields a broadband performance advantage. Up to 5 kHz the acceleration autospectra are very similar. Above 5 kHz, until the test ends at 7 kHz, different resonances occur. While this distinguishes performance at different prestress levels, none offers a distinct broadband advantage. In the .1V tests, a prestress of 1.9 ksi yields the best output until 4 kHz. Then, due to resonances, this prestress setting had the worst performance up to 7 kHz. As a measure of broadband performance, the area under the autospectra (i.e. acceleration squared times frequency) for the different prestress

settings at each excitation voltage are shown in Fig. 4. In Fig 4, the essentially constant traces indicate insensitivity to prestress.

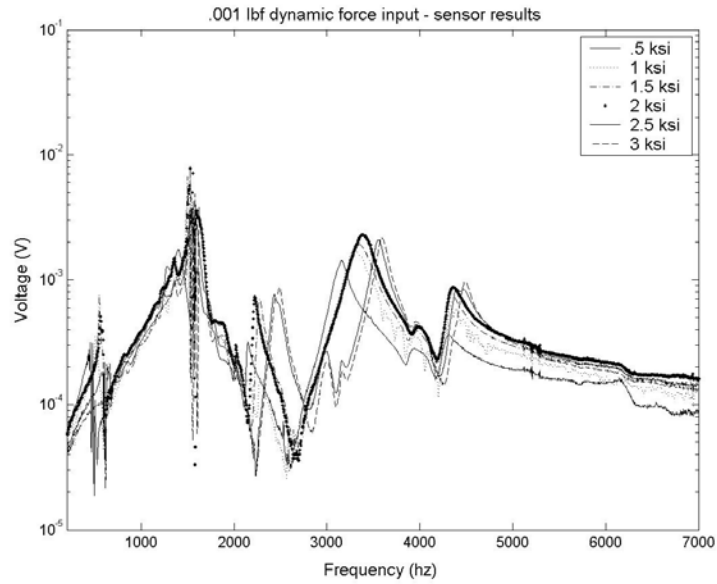


Fig.1 Sensor performance comparison for .001 lbf dynamic force input.

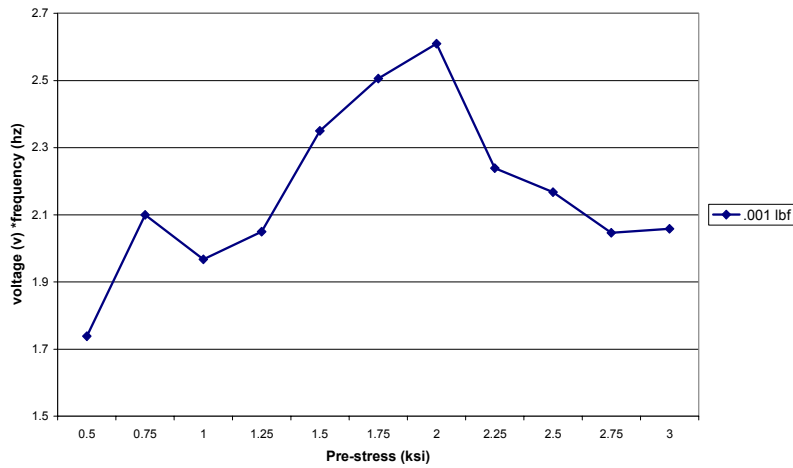


Fig.2 Area calculation under voltage vs. frequency curves for fig.1 proves 2 ksi to have optimum broadband performance.

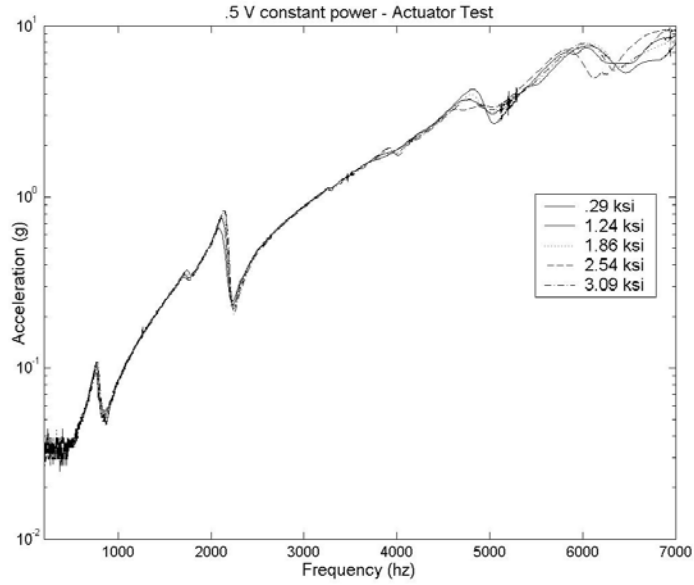


Fig.3 Actuator performance for .5 V constant input power.

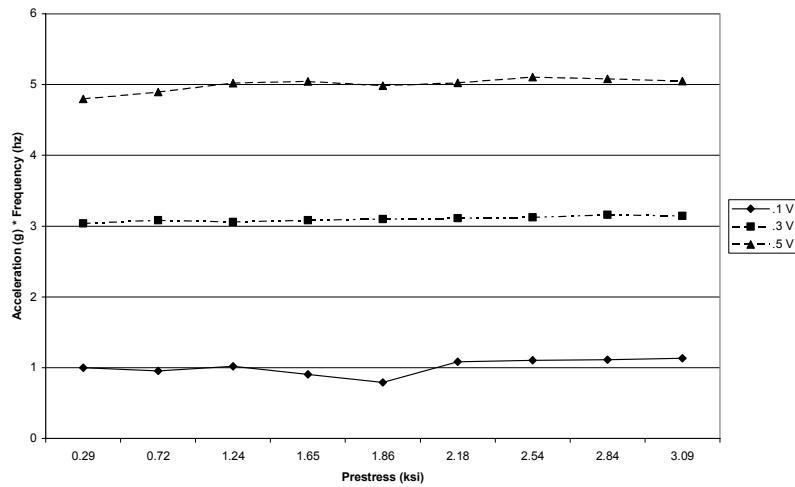
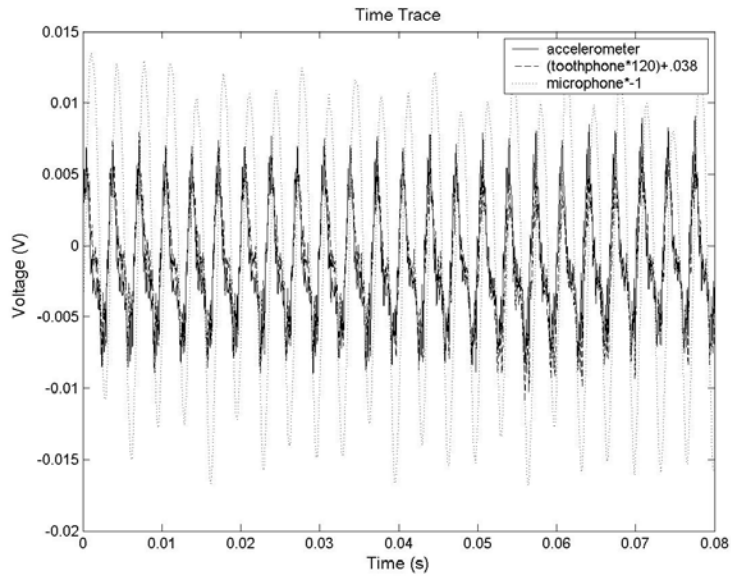


Fig.4 Area calculation under acceleration vs. frequency curves for actuator tests of .1V, .3V and .5V constant input.

#### IV. TOOTH VIBRATION RESULTS

The goal of these tests was to compare the performance of the tooth phone to other devices. A DSP SigLab signal box was used to record the output voltages from the tooth phone transducer, the accelerometer used in the actuator tests and a microphone while they were excited with a constant frequency hum. Both the tooth phone and the accelerometer were pressed with uniform pressure against the lead author's front teeth and the microphone was held an inch in front of the teeth.

Time traces and frequency autospectra from all three sensors are shown in Figs. 5 and 6. The signals from the accelerometer and microphone were amplified by their respective signal conditioners while the signal from the tooth phone transducer was not amplified. Phase and gain of the signals were scaled during post-processing to ease trend comparison. The accelerometer and tooth phone traces are essentially identical after adjusting gain and phase, and both are in close agreement with microphone out to ~2kHz.



*Fig.5* Accelerometer, tooth phone & microphone time histories with incorporation of a tooth phone DC offset and gain of 120 and microphone phase inversion.

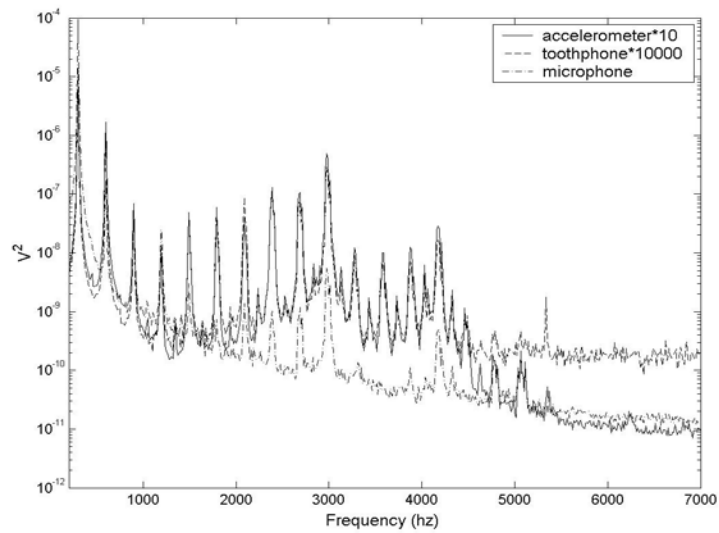


*Fig.6* Accelerometer, tooth phone & microphone autospectra.

Frequency response functions and coherence functions of the tooth phone and accelerometer output voltages per microphone output voltage were also recorded to provide a measure of the similarity between the tooth vibrations as recorded by the tooth phone and accelerometer and the acoustic pressure produced as measured by the microphone. From the autospectra of Fig.6, it is apparent that meaningful signals are detected at the harmonic tones indicated by the frequency spikes, with the noise floor of all three sensors masking information at intermediate frequencies. Thus, it is expected that if meaningful similarities arise at the tooth vibrations and in the air in front of the tooth, they will be revealed by high coherence values at the frequency spikes as observed in Fig. 7. Notably, the tooth phone performs as well as the accelerometer for detecting tooth vibrations, and there is a substantial correlation between the measured tooth vibrations and the measured acoustic field frequency content.

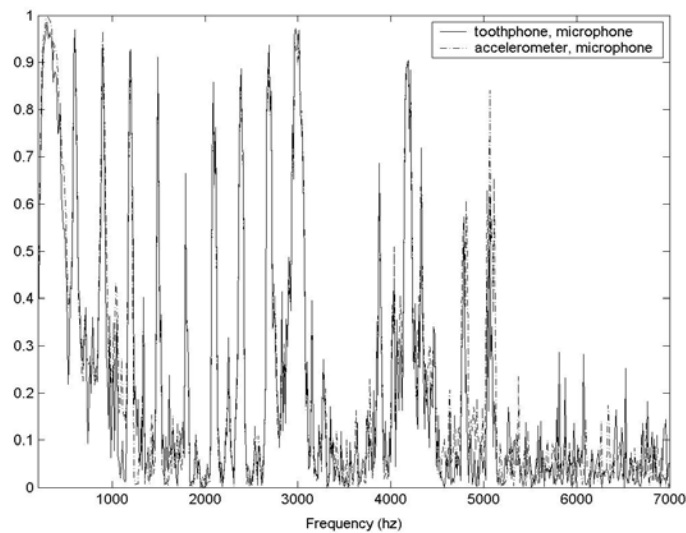


*Fig.7* Coherence functions for tooth vibration to acoustic pressure relationship from tooth phone, accelerometer and microphone frequency response functions.

## V. SUMMARY

This research has characterized the performance of the tooth phone transducer as both an actuator and a sensor. Sensor performance is optimized with a prestress of 2 ksi, while actuator performance is relatively insensitive to prestress. Time traces and coherence function results indicate the tooth phone performs well at detecting tooth vibrations and that a high correlation exists between tooth vibrations measured with the tooth phone and measured acoustic fields.

## ACKNOWLEDGEMENTS

The authors thank Dr. B. Mersky of Audiodontics, Inc. for discussions and support through sponsorship from the U.S. Army Communications-Electronics Research, Development and Engineering Center.

## REFERENCES

- [1] Calkins, F. T, Dapino, M. J, Flatau, A. B. *Effect of prestress on the dynamic performance of a Terfenol-D transducer* SPIE Symposium on Smart Structures and Materials #3041-23, 1997
- [2] Engdahl, Göran. *Handbook of Giant Magnetostrictive Materials*. Academic Press.
- [3] Blevins, R. D. *Formulas For Natural Frequency And Mode Shape*, 1979.
- [4] Kellogg, R.A. and Flatau, A.B. *Experimental Investigation of Terfenol-D's Elastic Modulus* Journal of Intelligent Material Systems and Structures, to appear, 2005

## References

1. Arms S.W., Townsend, C.P., Churchill, D.L., Galbreath, J.H., Mundell, S.W. 2005. *Power Management for Energy Harvesting Wireless Sensors* 12<sup>th</sup> SPIE Int'l symposium on Smart Structures and Smart Materials. San Diego.
2. Asian Development Bank. 1996. *Solar Photovoltaic Power Generation Using PV Technology Volume II: The economics of PV Systems*.
3. Calkins, F.T., Dapino, M.J., and Flatau, A.B. 1997. *Effect of Prestress on the Dynamic Performance of a Terfenol-D Transducer* Proceedings of SPIE, 3041-23: San Diego.
4. Calkins, F. T. 1997. *Design, analysis and modeling of giant magnetostrictive transducers*, Ph.D. Dissertation: Iowa State University.
5. Clark, A.E. "Structural Fe based alloys with high magnetostriction," Galfenol Workshop, [www.aerosmart.umd.edu/Galfenol](http://www.aerosmart.umd.edu/Galfenol) Univ. of MD, College Park, January 29<sup>th</sup>, 2004.
6. Chopra, I. 2003. *Smart Structures* Class Notes: Univ. of MD, College Park..
7. Dorf, R.C., Svoboda, J.A. 2001. *Introduction to Electric Circuits* 5<sup>th</sup> Edition, John Wiley & Sons, Inc.
8. Emadi, A. 2005. *Energy-Efficient Electric Motors*. New York: Marcel Dekker, Inc
9. Engdahl, G. 2000. *Handbook of Giant Magnetostrictive Materials*. USA: Academic Press.
10. Idaho National Laboratory, Geothermal Program Homepage <http://geothermal.id.doe.gov>.

11. Jiandong, Naibo, Xianhuan, Jing, and Ding Huishen. 1997. *Mini Hydropower*. England: John Wiley & Sons.
12. Jiles, D. 1991. *Magnetism and Magnetic Materials*. London: Chapman & Hall.
13. Johnson, Gary L. 1985. *Wind Energy Systems*. New Jersey: Prentice-Hall, Inc.
14. Kasyap, A., Lim, J., Johnson, D., Horowitz, S., Nishida, T., Ngo, K., Sheplak, M., Cattafesta, L. 2002. *Energy Reclamation from a vibrating Piezoceramic Composite beam*. Florida: 9<sup>th</sup> international Congress on Sound and Vibration, Paper No. 271.
15. Kellogg, R.A., Flatau, A.B., Clark, A.E., Wun-Fogle M., Lograsso, T. 2005. *Quasi-static Transduction Characterization of Galfenol*. *J. of Intelligent Material Systems and Structures*, vol. 16, pp. 471-479.
16. Kellogg, R. A. 2003. *Development and Modeling of Iron-Gallium Alloys*. PhD Dissertation: Iowa State University.
17. Khennas, Dunnett, and Hugh Piggott. 2003. *Small Wind Systems for Rural Energy Services*. England: ITDG Publishing.
18. Markvart, Thomas. 1994. *Solar Electricity*. England: John Wiley & Sons.
19. McGoldrick, R. T, and Russo, V. L. "Hull Vibration Investigation on SS Gopher Mariner" Society of Naval Architects and Marine Engineers," Annual Meeting, New York, NY. Nov. 9-12 1955.
20. Messenger, Roger A. and Ventre, Jerry. 2004. *Photovoltaic Systems Engineering*. Florida: CRC Press.

21. Moffet, M.B., Clark, A.E., Wun-Fogle, M., Linberg, J.F., Teter, J.P., McLaughlin, E.A. 1991. *Characterization of Terfenol-D for magnetostrictive transducers*. J. Acoust. Soc. Am., 89(3), pp. 1448-1455.
22. Ottman, G. K., Hofmann, H. F., and Lesieutre G. A., “Optimized Piezoelectric Energy Harvesting Circuit Using Step-Down Converter in Discontinuous Conduction Mode,” IEEE Transactions on Power Electronics, Vol 18, No. 2 March 2003.
23. Reese, R. L. 2000. *University Physics*. USA: Brooks/Cole Publishing Co.
24. Schulze, M.P., Greenough, R.D., Galloway, N. 1992. *The Stress dependence of  $k_{33}$ ,  $d_{33}$ ,  $\lambda$ , and  $\mu$  in  $Tb_{0.3}Dy_{0.7}Fe_{1.95}$* . IEEE Transactions on Magnetics, Vol. 28, No. 5.
25. Sodano, H. A., Park G., and Inman, D. J. “Estimation of Electric Charge output for Piezoelectric Energy Harvesting,” Strain Vol. 40 Issue 2, p 49, May 2004.
26. Umeda, M. Nakamura, K. and Ueha, S. 1997. *Energy Storage Characteristics of a Piezo-Generator using Impact Induced Vibration*. Japanese Journal of Applied Physics, Vol. 36, Part 1, No. 5B, pp. 3146-3151.